2019-01-01

Computational Studies On Perovskite-Metallofullerene Interface And Magnetic Properties Of Mn-Based Mixed Olivines

Bethuel Omutiti Khamala
University of Texas at El Paso, khamalabethuel59@gmail.com

COMPUTATIONAL STUDIES ON PEROVSKITE-METALLOFULLERENE INTERFACE AND MAGNETIC PROPERTIES OF Mn-BASED MIXED OLIVINES

BETHUEL OMUTITI KHAMALA

Doctoral Program in Computational Science

APPROVED:

Rajendra R. Zope, Ph.D., Chair

Tunna Baruah, Ph.D., Co-Chair

Ming-Ying Leung, Ph.D.

Mahesh Narayan, Ph.D.

Stephen Crites, Ph.D.
Dean of the Graduate School

Dedication

Dedicated to my lovely wife, kids, and parents.

COMPUTATIONAL STUDIES ON PEROVSKITE-METALLOFULLERENE INTERFACE AND MAGNETIC PROPERTIES OF Mn-BASED MIXED OLIVINES

by

BETHUEL OMUTITI KHAMALA, MS

DISSERTATION

Presented to the Faculty of the Graduate School of

The University of Texas at El Paso

in Partial Fulfillment

of the Requirements

for the Degree of

DOCTOR OF PHILOSOPHY

Computational Science Program

THE UNIVERSITY OF TEXAS AT EL PASO

May 2019

ACKNOWLEDGEMENTS

I would like to express my utmost gratitude to my professors, Dr. Rajendra Zope who was my advisor and Dr. Tunna Baruah who was my co-advisor, for their professional guidance and extraordinary measure of patience. Their willingness to share knowledge and discuss ideas as well as their insightful comments played a pivotal role in bringing this work to completion. Their tireless efforts in facilitating access to computational resources are greatly acknowledged. I extend many thanks to my dissertation committee members for their guidance and support, and to the University of Texas at El Paso (UTEP) for giving me an opportunity to pursue in graduate studies.

My innermost gratitude is also conveyed to all members of the Electronic Structure Lab for the conducive and exemplary work atmosphere. Much gratitude is extended to the postdoc, Dr. Yoh Yamamoto for reading my dissertation and discussion, and Dr. Luis Basurto and Dr. Jorge Vargas for motivating me in my computational work. I'd also thank Carlos, Sharmin, Shamsul, and Prakash. It is hard to forget the friendliness and the great feeling of being part of this wonderful team.

My research studies at UTEP would not have been possible without the financial support from the Computational Science Program. I am grateful to Southern University for preparing me adequately for my graduate courses.

I am deeply indebted to my wife and children for their love and patience during my academic journey. For the love and prayers of my parents, Paul and Jane, I am deeply thankful. Finally, I thank the Almighty God for his love and mercy, without which I would not have come this far.

ABSTRACT

Methyl ammonium lead halide ($MAPbX_3$) perovskite based solar cells have recently emerged as promising class of materials for photovoltaic applications with efficiencies reaching over 22%. Designing interfaces with strong binding is vital to developing efficient, high-performing solar cells. Fullerene-based materials are widely employed as efficient electron acceptors and can serve as electron transporting layer in perovskite based solar cells. We have studied interfaces of methyl ammonium lead iodide $MAPbI_3$ with $Sc_3N@C_{80}$ fullerene and $Sc_3N@C_{80}$PCBM fullerene derivate within the density functional formalism. Different surface terminations and orientations of the methyl ammonium are examined for binding of the fullerene layer. Our calculated binding energies shows the possibility of adsorption of the fullerene and its derivative on the perovskite surface. The changes in the electronic structure of the perovskite surface due to the fullerene layer is studied.

We have also studied the structural, electronic, and magnetic behavior of Mn based olivines A_2BX_4 (A=Mn, B=Si, X=S, Se). The olivine chalcogenides are antiferromagnets and show linear trend in the transitional temperature with decrease of transition temperature from 86K for Mn_2SiS_4 to 66K for Mn_2SiSe_4. We studied $Mn_2SiS_{4-x}Se_x$ for x = 0 to x = 4 through first principles calculations for the structural, electronic, and antiferromagnetic spin arrangements of the four different compositions of $Mn_2SiS_{4-x}Se_x$. Our spin magnetic moments, density of states, and bandgap are comparable to the available experimental data. We also find several spin structures can exist depending on the doping content.

TABLE OF CONTENTS

LIST OF TABLES

LIST OF FIGURES

CHAPTER 1: INTRODUCTION

Energy is a very important resource in any natural or artificial setting. For instance, it could be viewed as a trait which when transferred to an object, could impact work performance, produce heat, and be transformed from one form to the other as desired. There are several sources of energy which can broadly categorized as the renewable and nonrenewable sources. Bioenergy and hydro-energy dominate the renewable energies. Such energies are increasingly getting exhausted with the already developed technologies. Bio-energy won't meet the worldwide potential due to overdependence on land which is a multifunctional resource [1]. All land is needed for food, larger plantations for biomass, natural conservation, and climate protection [1].

Other sources of energy include coal, oil, and natural gas, all of which are fossil fuels. These sources contribute to a total of about 81% of the energy supplied to the united states. We all need this energy for domestic and commercial purposes. We get concerned more about the most affordable energy for a long-term. Presently, we depend more on fuels to heat or cool our homes, operate automobiles, power industry and manufacturing, and supply electricity. Over-dependence on fossil fuels will have to decline as more pressure builds on their sources.

The energy supply problem in 1970s led to the public awareness program that was launched in 1973 about the limitation of fossil fuels to the many governments including the US, Japan, and European nations [2]. The need to quickly build up the advanced technology that converts the resources into reserves is desirable. We look at Table 1.1, which compares resource base and reserve-to-production ratio. We see that some regions appear to spend less technologically in converting resources to reserves.

Table 1.1: Crude Oil resources in Various Regions of the World. Source: Calculated from the Data warehouse in NPC [3].

	Percent of World Convention Crude oil Resources	Reserve-to-Production in Region
Africa	5.4	32.1
Asia/Oceana	6.6	14.0
Canada	6.7	14.9
Central/South America	10.3	30.2
Middle East	39.0	79.5
OECD Europe	3.5	8.0
Non−OECD Europe	16.0	28.0
United States	12.5	11.9

We can infer from Table 1.1, that, Middle East, non-OECD Europe (mostly in the Russian Federation), and Central/South America (Primarily Venezuela) contain about 65% of the World's conventional crude oil. These estimates, though approximate from both magnitude and in regional but clearly provides a probable idea that may project US resource base in the impossibilities to develop than most of the crude oil in other areas of the world. Elsewhere [4], the ratio of proved reserves in the US to annual production is 11.9 compared to 40.5 for the world. Obtaining data on the costs and technologies involved is quite hard if possible, because most of the World's Petroleum resources and reserves are controlled by the national oil companies.

What about the natural gas? The situation is almost like that of the Oil reserves. However, natural gas hydrates appear promising but less economically competitive. Gas hydrates is where a significant amount of methane could be trapped within a crystal structure of water ice. This happens in Marine sediments and in places of very low temperatures where permafrost could exist. Methane molecule must be present to stabilize a cage of water molecule in temperatures above the

freezing point of the water and high pressure. These two conditions must co-exist for the hydrates to be stable. Most often, the hydrates harnessed are relatively of low concentration. This makes it uneconomical [5].

In early 1990s, ecological issues and global warming problems associated with fossil fuels formed the major driving force in promoting alternative sources of energy, particularly photovoltaics [2]. Solar has, over the years, had increasingly great potential, in providing clean, economical, and reliable power. In America, Solar power already play a key role across the nation's electricity system. It serves as an equal opportunity renewable energy resource. Multiple sources reveal the impressive growth rate for the solar energy in every state of the US.

The U.S. National Renewable Energy Laboratory (NREL), under the widespread adoption of renewable energy, determined Solar to have an important role that would potentially account for 4% of national electricity production by 2030, and 13% by 2050 [6] . The United States solar market installed 2 044 MW direct current in the first quarter of 2017 that realized more than half the capacity increments from PV segments that had more than 1 GW_{dc} in the close of its sixth consecutive quarter in the previous year.

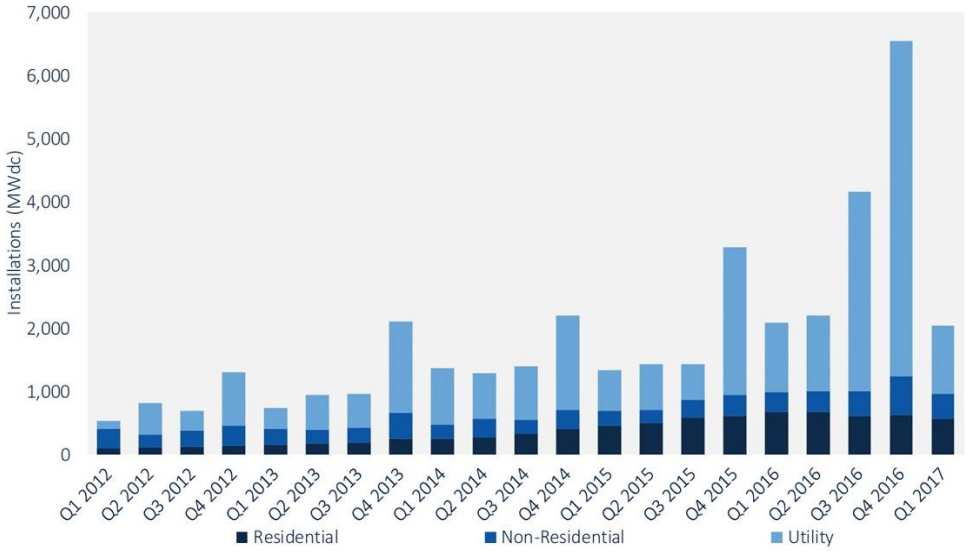

Figure 1.1: New U.S. Electricity Generating Capacity Additions, 2010-Q1 2017. (Source: SEIA/GTM Research)

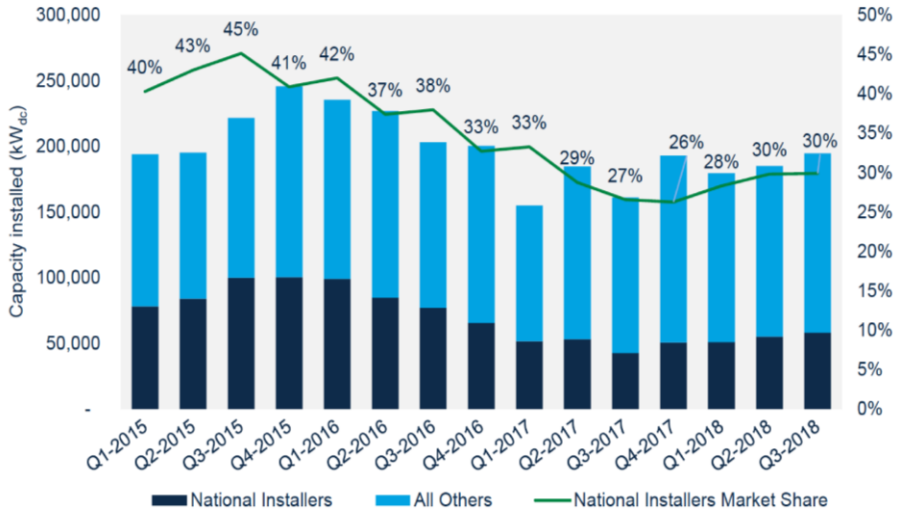

Figure 1.2: Residential national installer market share, California, Q1 2015-Q3 2018 [7]

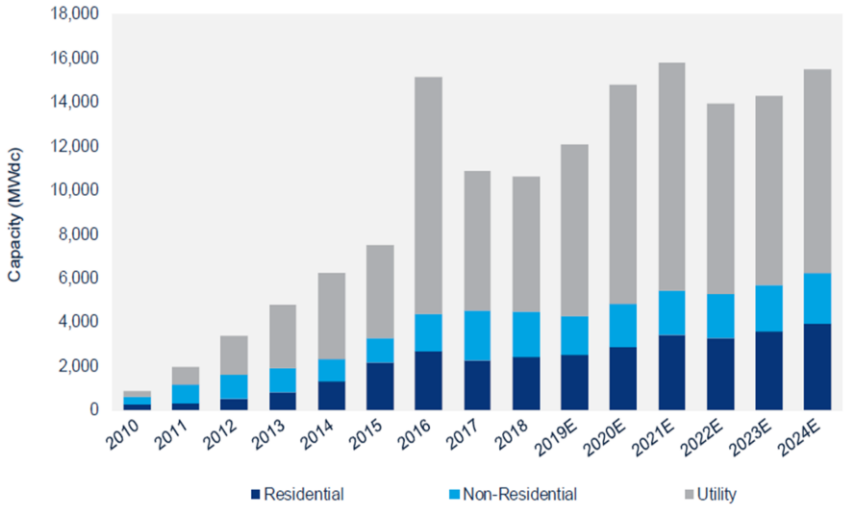

Figure 1.3 U.S. PV Installation Forecast, 2010-2024E [8]

As much as the PV installation forecast in US keep increasing, the national installers declined over the years except in California, which is expected to increase at 1% annually since first quarter of 2018. Clearly, despite the costs invested in the solar energy, the trends could be worrying.

Significant efforts have been made in search for enough, clean, sustainable, and efficient energy supply to our world. The search continues since most of the available energy sources appear

deficient, expensive, or unstable in predictions. We therefore join the search team by providing a very promising platform in the study of methyl- ammonium lead iodide, $MAPbI_3$ as interfaced with fullerene and fullerene derivatives. Perovskite solar cells have attracted much attention with its fast record achieved in power conversion efficiencies [9]. Generally, organic, inorganic, and hybrid perovskites have interesting properties such as ease of processing, good electrical mobility, economic importance, and band gap tunability [10]. Several experimental and theoretical reports have also revealed that the superior photovoltaic performance of these materials is associated with their optoelectronic properties such as high charge carrier mobility, high optical absorption coefficient, low exciton binding energy, and low trap density [11].

Olivine, like perovskite was discovered by mineralogists [12, 13] and has attracted much attention in magnetic and optoelectronic applications. Spontaneous magnetization in Mn_2SiS_4 within a low narrow temperature window makes it applicable to energy particle detectors [14].

1.1 PHYSICS OF SOLAR CELLS

Solar cells rely on the photoelectric effect to convert the energy of light directly into electricity. Solar cells are made of semiconducting material which have the capability of absorbing light and delivering a portion of the energy of absorbed photons to formation of charge carriers-electrons and holes. The energy of the photons depends on the frequency of the light energy. Usually, the energy of the visible photons is enough to excite the bound electrons in solid into a higher energy level where they can readily move. The effectiveness of the solar cell depends on the choice of the absorbent material and the way they are connected to the external circuit.

The Fig.1.4 below shows a schematic diagram of a p-n junction and the behavior of charges in the vicinity of light energy.

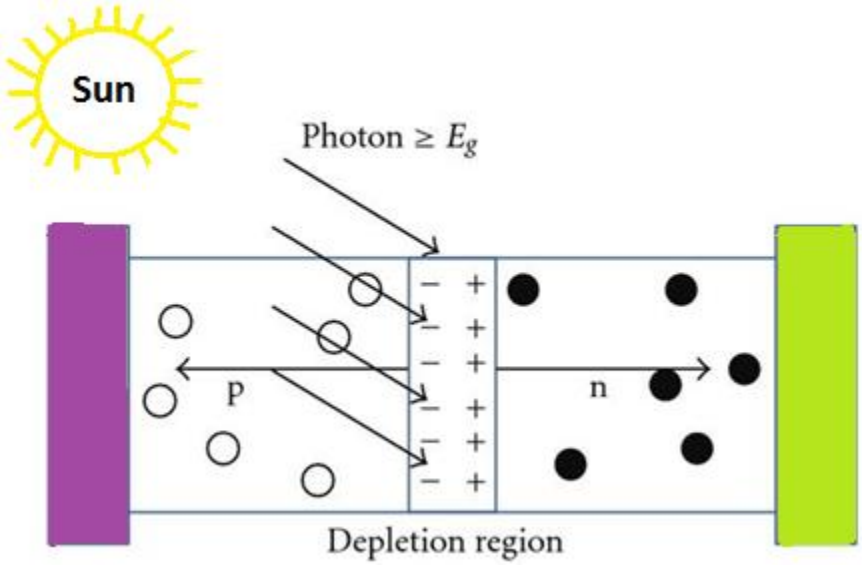

Figure 1.4: Basic p-n junction solar cell showing charge transport

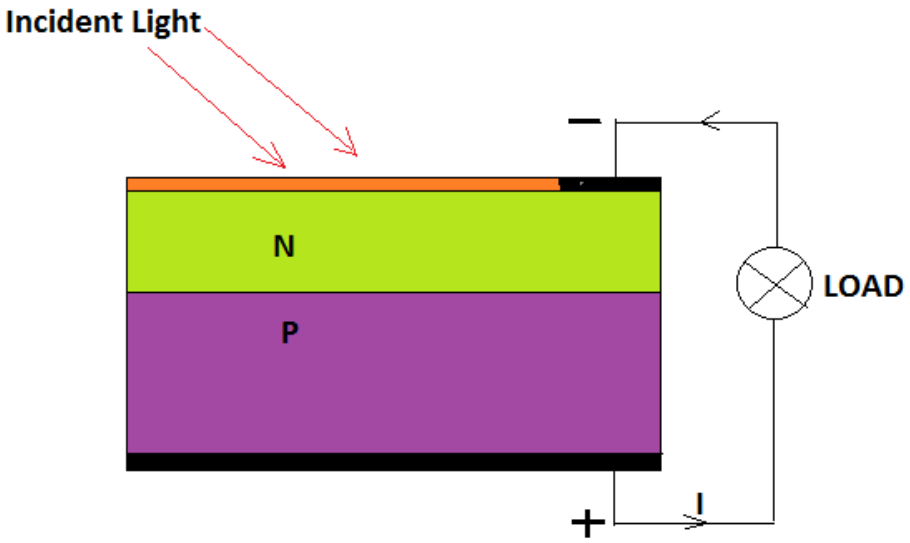

Figure 1.5: Photovoltaic cell

Current generation in a solar cell starts by photons absorption near the p-n junction to create electron-hole pairs. The incident photons must have energy greater than the band gap. The electron-hole pairs are separated due to the action of the electric field at the p-n junction. The front and back electrical contacts short-circuit the solar cell enabling the electron-hole pairs to flow through the external circuit hence constituting the current flow [15]. In our dissertation, a perovskite-fullerene interface in some sense behaves like a p-n junction in a conventional solar cell. The following is the description of some common solar cells.

1.1.1 Silicon based solar cells

These silicon cell types are monocrystalline, polycrystalline, amorphous, and hybrid solar cells. They have a conversion efficiency of up to 20% and about 90% in the photovoltaic market today. The central layer constitutes a single material that absorbs photon.

1.1.2 Dye-Sensitized solar cells (DSC

The DSC has a monolayer of a dye sandwiched between nanostructured electron and hole conductors. The monolayer in this case is the absorbent layer. Charge separation is achieved by the effect of electric field in the central layer. Firstly, the central layer acts as the macro-homogeneous medium through which only the macroscopic electrical field perpendicular to the contact facilitates the transport and collection of electrons and holes [16].

DSC is a type of nanocomposite solar cells where the materials that constitute the conduction bands and the valence bands are different. This greatly ensures the separation of electron-hole pairs which further necessitates charge collection.

1.1.3 Inorganic thin films

These are standard inorganic materials with conductivities that form the intermediate between metals and insulators. The materials are also of a homogeneous class with a layer whose thickness range from a fraction of a nanometers to several micrometers. They have relatively high dielectric permittivities and low exciton binding energies. The lower exciton energies make it easy for charge separation process at low temperatures, specifically at room temperature without the effect of electric field. Once the photogenerated carriers separates, they rapidly form part of the delocalized carriers at the conduction and valence bands respectively [17].

1.1.4 c-Si solar cell

Like in the standard inorganic solar cells, c-Si solar cells have thin region where photogeneration, separation, and collection of charges effectively take place at room temperature. In this case, the pn junction [18] is the one that occupies the small region of this cell's activity. The pn junction ensures that the carriers with opposite polarities diffuse rapidly before recombination thus enhancing charge collection.

1.1.5 Perovskite solar cells

1.1.5.1 The architecture of Perovskite

Any material with the same structure as that of Calcium Titanium oxide, $CaTiO_3$ is called a perovskite [19]. A perovskite solar cell is simply a solar cell with a perovskite structure, usually a hybrid organic-inorganic lead. $MAPbI_3$ acts as the light-harvesting active layer of a perovskite solar cell. These solar cells are generally consisting of hybrid organic-inorganic lead halides (ABX_3) as shown in fig. 1.6.

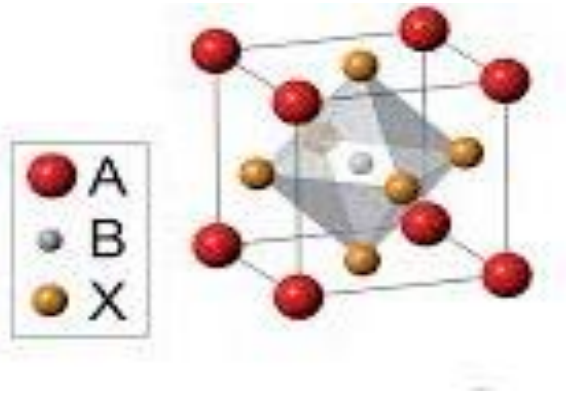

Figure 1.6: Perovskite structure

Here, A is an organic cation like methyl ammonium (MA), B is lead, a cation which is an inorganic, and X a halogen anion which is iodine. A is usually at the origin but can be viewed at the center of the structure while B occupy the origin position without changing the structure.

1.1.5.2 Charge separation and charge collection

If the photons have enough energy to create the electron-hole pair, a photogeneration event is initiated that creates an excitation dipole. Sometimes the excited electrons lose the absorbed photon energy by relaxing back to the holes. This phenomenon is described as recombination. The ability to effectively disturb the recombination process of the electron-hole pairs at thermal equilibrium is called charge separation.

Therefore, based on photovoltaic conversion, the significant effect of negating recombination process is called charge separation. The visibility of this process starts with excitons formation. While at the conduction band, the de-excited electrons will be transported to their respective contacts instead of recombining. Thus, the overall process involving excitons right from the photogeneration, their dissociation into two separate charge carriers of unlike polarities, and eventual transport of both charges to their respective contacts is called charge separation and charge collection.

The central layer may have a given distinct absorbent layer with its own definite relative permittivities. The central layer acts as the depletion zone in conventional solar cell. Different absorbers and their relative permittivities will consequently have different mechanisms of charge separation and charge collection [20].

1.2 ORGANIC/INORGANIC INTERFACE PROPERTIES

1.2.1 Interface study- Perovskite/fullerene interfaces

In this work, we study interfacial characteristics of perovskite/fullerene or fullerene derivative interfaces. Jeng and coworkers [21] in 2003, used C_{60} fullerene and its derivative phenyl-C_{60}-butyric acid methyl ester derivate (PCBM) in perovskite solar cells. In the same study they also used another derivate of fullerene-tetrahydro-di [1,4] methanonaphthaleno [5, 6]fullerene-C_{60} indene bisadduct. The power conversion efficiency found in this study were less than 4%. In recent years, Lin and coworkers [22] reported photochemical efficiency of 18.5% by using Indene-C_{60} bisadduct. Grätzel and co-workers [23] have used PCBM analogue of C_{71} in an inverted perovskite solar cell device and reported efficiencies above 20%. The perovskite acts as the hole transporting layer (HTL) while the fullerene or fullerene derivative the electron extracting layer (EEL). The fullerene addition to the perovskite layer has been found to play an important role in passivating the charge traps at the surfaces and grain boundaries of the thin films. They also help in improving the stability and form a barrier for

moisture. Thus, the addition of fullerenes to the perovskite solar cells not only provide the electron extracting layer but it also helps in improving the stability and in general, in higher device performances. In our study, we have studied C_{60} perovskite interface and C_{80} perovskite interface with emphasis on the later. Several orientations effects have been considered both on $MAPbI_3$ slab and the fullerene. We have considered the topC and topN models for the slab, where, the topC model has the $–CH_3$ groups of MA cations oriented towards vacuum in all layers while in topN model, the MA cations are oriented with their $–NH_3$ groups pointing to vacuum, all in 001 direction.

Other orientation effects for the fullerene are either the pentagonal or hexagonal phase planes adjacent to the interface. The fullerene-PCBM include the functional groups such as -COOH made adjacent to the interface. Therefore, several configurations with different architectures were optimized and the most stable complexes identified for several properties studied.

1.2.2 Electronic energy levels

Niels Bohr formulated a theory for the hydrogen atom in 1913 that revealed why the electrons inside an atom occupy only the allowed orbitals with a specific energy. His model/theory confirmed that the energy of an electron in an atom is quantized. Such a fundamental concept obeys the laws of physics which states that matter is most stable at the lowest possible energy. The atom whose electron is in the lowest energy orbit is said to be at the ground state.

Similarly, this concept can be used to study the electronic structure of matter. The understanding of the electronic energy levels and the physics of photogeneration, charge movement and charge collection at the interface is used in improving the efficiency of our perovskite solar cell. The most common transport properties that we want to discuss in this section are; vacuum level, work function, and the bandgap.

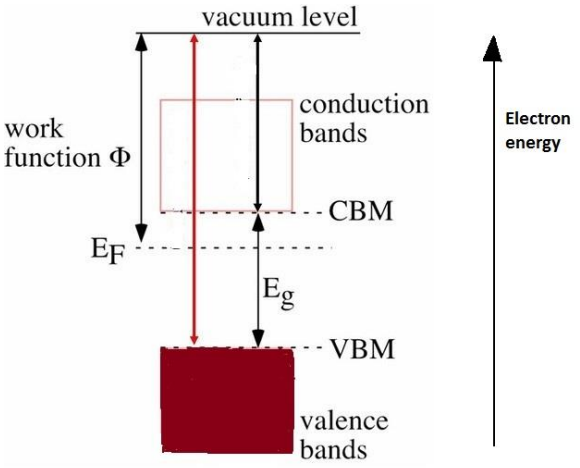

Figure 1.7: Energy diagram of a semiconductor defining vacuum level, work function, conduction band minimum (CBM), Fermi level (EF), and valence band maximum (VBM).

At 0 K, the lowest bands filled with electrons constitute the valence bands while the highest energy states that are unoccupied constitute the conduction bands. The band gap (E_g) is the energy difference between VBM and CBM. In metals, work function is the minimum amount of energy required to dislodge an electron from a metal surface, usually depends on the condition of the surface. The position of the fermi level varies from one material to the other. The vacuum level is the energy of an electron that is positioned at rest point just outside the surface where it could not feel the electrostatic effect [24]. The difference between the vacuum level and fermi level is called work function. The detailed difference is shown in Fig. 1.6.

1.3 MAGNETIC PROPERTIES

When describing magnetic properties, the description is used to mean the behavior of ferromagnets. Magnetic materials are classified into four main categories; paramagnetic, diamagnetic, ferromagnetic, and ferrimagnetic. Paramagnetic are those magnetic materials which are not strongly attracted to a magnet. Their relative permeabilities are usually small and positive

e.g aluminum. At high temperatures, thermal energy exceeds the interaction energy between spins on neighboring atoms thus rendering almost every material paramagnetic at high temperatures.

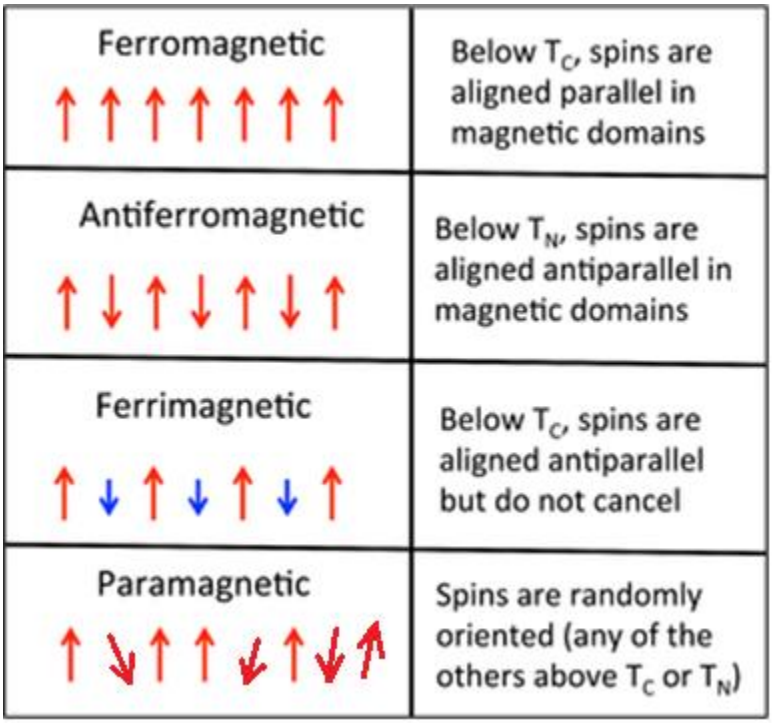

Figure 1.8 Pictorial representation of magnetic ordering [25].

Diamagnetic materials are those magnetic materials that are repelled by the magnet. Their magnetic permeability is usually small (less than one) and only magnetized in a strong magnetic field aligning opposite to the applied field.

Ferromagnetic, antiferromagnetic, and ferrimagnetic which are within our scope are described in Fig. 1.7 above. The Mn-based Olivines were found to be antiferromagnetic and undergo geometric frustration. The detail of olive is elucidated in chapter 4.

1.4 ORGANIZATION OF THIS THESIS

This dissertation is organized as follows. Chapter one, mainly the introduction chapter, is defined to give the reader the relevant background about research work carried out. A little show of a dire energy need is emphasized. It starts by showing how fossil fuels is largely utilized as the energy resource despite its negative environmental effects and its foreseen depletion soon. Other sources of energy are also discussed which are either costlier or unpredictable. Perovskite solar cells are also discussed. Other relevant theories discussed include the magnetic properties which is relevant in understanding the magnetic structure of the Olivines.

Chapter 2 presents the general methods used in this research. It starts with a theoretical overview of DFT followed by VASP description and how it was utilized in this work. Several algorithms within VASP that were the key in the optimization procedures and material property studies are also discussed and their computational details mentioned.

In chapter 3, interfacial studies of perovskite/ fullerene and perovskite/fullerene derivatives are discussed in detail. Specifically, $MAPbI_3/Sc_3N@C_{80}$ and $MAPbI_3/Sc_3N@C_{80}$-PCBM are the interfaces for structural, electronic, electronic related properties such as binding energy, band gap, density of states, partial density of states, and charge difference. Several orientations both at the substrate level and the electron extracting level were considered. The ones with most stable adlayer were determined and identified as viable candidates to perovskite solar cells. These results are summarized in an article that is submitted to Journal of Physics.

In chapter 4, we have investigated the structural, electronic, and magnetic behavior of Mn-based Olivine A2BX4 (A=Mn, B=Si, X=S, Se). The unique magnetic property of Olivines makes them favorable to magnetic and optoelectronic applications. The Olivine Chalcogenides are found to be antiferromagnets and show similar linear trend in the transitional temperature Vs selenium content in Mn2SiS4 and Mn2SiSe4 at 86 K and 66 K respectively. The detailed study of mixed Mn2SiS4-xSex for x = 0 to x = 4 using first principle study calculations for the structural, electronic, and antiferromagnetic spin arrangements of the four different compositions of Mn2SiS4-xSex is shown in chapter 4. A manuscript based on these results has been accepted for

publication in the Physical review B as “Antiferromagnetism and the emergence of frustration in the saw-tooth lattice chalcogenide olivines Mn2SiS4−xSex (x=0–4)”.

Chapter 5 is the summary and conclusion of our research efforts in these projects.

REFERENCES

[1] J. Popp, Z. Lakner, M. H. Rakos and M. Fari, "The effect of bioenergy expansion: Food, energy, and environment," *Renewable and Sustainable energy Reviews,* vol. 32, pp. 559-578, 2014.

[2] A. Shah, P. Torres, R. Tscharner, N. Wyrsch and H. Keppner, "Photovoltaic Technology: The Case for Thin-Film Solar Cells," *Science,* vol. 285, no. 5428, pp. 692-698, 1999.

[3] "Facing the Hard Truths about Energy: Topic Paper No. 19," National Petroleum Council, 2007.

[4] "Bp Statistical Reviews of World Energy," British petroleum, 2006.

[5] G. J. Moridis, T. Collett, R. Boswell, M. Kurihara and M. ,. Reagan, "Toward Production From Gas Hydrates: Assessment of Resources, Technology and Potential," in *SPE UnconventionalReservoirs Conference*, Keystone, 2008.

[6] Hand, M.M.; Baldwin, S.; DeMeo, E.; Reilly, J.; Arent, D.; Porro, G.; Mai, T.; Meshek, M.; Sandor, D. eds. 4 vols. NREL/TP-6A20-52409. Golden, CO: National Renewable Energy Laboratory.

[7] "Wood Mackenzie Power & Renewables," Q4 2018 US. PV.

[8] "Wood Mackenzie U.S. Solar Market Insight 2018 Year in Review".

[9] J. Liang, C. Wang, Y. Wang, Z. Xu, Z. Lu, Y. Ma, Y. H. Hongfei Zhu, C. Xiao, X. Yi, G. Zhu, H. Lv, L. Ma, T. Chen, Z. Tie, Z. Jin and J. Liu, "All-Inorganic Perovskite Solar Cells," *J. Am. Chem. Soc.,* vol. 49, no. 138, pp. 15829-15832, 2016.

[10] D. B. Mitzi, "Templating and structural engineering in organic–inorganic perovskites," *Royal Soc. Chem. ,* pp. 1-12, 2001.

[11] O. Selina and M. Klaus, "Substrate-dependent electronic structure and film formation of MAPbI3 perovskites," *Scientific Reports,* vol. 7, p. 40267, 2017.

[12] S. Nomura, R. Santoro, J. Fang and R. N, *J. Phys. Chem. Solids,* vol. 25, p. 901, 1964.

[13] R. Santoro, R. Newnham and S. Nomura, "Magnetic properties of Mn2SiO4 and Fe2SiO4," *J. Phys. Chem. Solids ,* vol. 27, no. 4, pp. 655-666, 1966.

[14] G. Lamarche, F. Lamarche and A.-M. Lamarche, "A possible 83K magnetic detector for high energy particles," *Physica B: Condensed Matter,* Vols. 194-196, pp. 219-220, 1994.

[15] C. Honsberg, "PV EDUCATION.ORG," 28 02 2019. [Online]. Available: https://www.pveducation.org/pvcdrom/solar-cell-operation/light-generated-current. [Accessed 07 05 2019].

[16] A. M. Gagliardi, A. d. Maur, D. Gentilini, F. d. Fonzo, A. Abrusei, H. J. Snaith, G. Divitini, C. Ducati and A. D. Caelo, *Nanoscale,* vol. 7, pp. 1136-1144, 2015.

[17] J. Bisquert, "Nanostructured Energy Devices: Equilibrium Concepts and Kinetics," CRS Press, Boca Raton, 2014.

[18] X. Y. Zhu, *J. Phys. Chem. lett,* vol. 5, no. 13, pp. 2283-2288, 2014.

[19] Y. Okamoto and Y. Suzuki, "Perovskite-type SrTiO3, CaTiO3, BaTiO3 porous film electrodes for dye-sensitized solar cells," *J. Ceram. Soc. ,* vol. 122, pp. 728-731, 2014.

[20] T. Kirchartz, J. Bisquert, I Mora-Sero, and G. Garcia-Belmonte "Classification of solar cells according to mechanisms of charge separation and charge collection.," *Phys. Chem. Chem. Phys.,* pp. 4007-4014 , 17, 2015.

[21] J.-Y. Jeng, Y.-F. Chiang, M.-H. Lee, S.-R. Peng, T.-F. Guo, P. Chen and T.-C. Wen, *Adv. Mater.,* vol. 25, pp. 3727-3732, 2013.

[22] Y. Lin, B. Chen, F. Zhao, X. Zheng, Y. Deng, Y. Shao, Y. Fang, Y. Bai, C. Wang and J. Huang, *Adv. Mater.,* vol. 29, no. 1700607, 2017.

[23] C.-H. Chiang, M. K. Nazeeruddin, M. Grätzel and C.-G. Wu, *Energy Environ. Sci.,* vol. 10, pp. 808 -817, 2017.

[24] D. Cahen and A. Kahn, "Electron Energetics at Surfaces and Interfaces: Concepts and Experiments.," *Adv. Mater.,* vol. 4, no. 15, pp. 271-277, 2003.

[25] "LibreTexts libraries are Powered by MindTouch® and are supported by the Department of Education Open Textbook Pilot Project, the UC Davis Office of the Provost, the UC Davis Library, the California State University Affordable Learning Solutions Program.".

[26] G. Nishant, A. Githin, P. Ramakrishna, S. Rajneel and P. K. F, Prospects of Nanostructure-Based Solar Cells for Manufacturing Future Generations of Photovoltaic Modules, 2009.

[27] "Photovoltaic Cells – Generating electricity," Images scientiific Instruments.

[28] S. Sharma, K.-K. Jain and A. Sharma, "Solar Cells: In Research and Applications," *Mat. Sci. Appl.,* vol. 6, pp. 1145-1155, 2015.

[29] Dmercer, "Wiki," 28 April 2019. [Online]. Available: https://wiki.analog.com/university/courses/eps/photovoltaic?rev=1556456132. [Accessed 07 May 2019].

CHAPTER 2: GENERAL METHOD

This chapter gives a theoretical overview of the methods used in this thesis. We start with description of the density functional theory (DFT), then introduce the simulation software, Vienna Ab Initio Simulation Package (VASP). We performed DFT calculations using the VASP electronic structure code [1, 2] to perform structural optimizations and to determine the magnetic, and electronic properties. By using the plane wave pseudopotential implementation of the density functional approximation as implemented in VASP, we computed structural configurations, system properties such as total energies, dispersion energies, magnetic, electronic and related properties from the first principles. We also describe the alternative methods to VASP and give the computational details of our work.

2.1 THE SCHRODINGER EQUATION

The Schrodinger equation is a differential equation that describes how the wave function of some physical system changes with time. In the Schrodinger equation (SE) the wave function ψ represents a quantum particle's state under an influence of an external potential V(r). The Schrodinger equation can be classified as time-dependent or time-independent.

2.1.1 The Time-independent Schrodinger equation

The time-independent Schrodinger equation (SE) describes the energy states and the wave function of a system for a given time-independent potential. This equation is used when the system is a stationary state.

The time independent Schrodinger equation is given by,

$$\hat{H}\Psi(r) = E\,\Psi(r), \qquad (2.1)$$

$$[T + V(r)]\,\Psi(r) = E\,\Psi(r)$$

where T + V = $\hat{H}$ with T and V being the kinetic and potential energy operators respectively.

In the equation (2.1), $\hat{H}$ is the Hamiltonian operator, Ψ is the wave function in the stationary state, and E the eigenvalue energy which is the energy of the stationary state Ψ(r).

For a hydrogen atom (single particle), we can solve SE exactly and determine the allowed energy state of the system. The $\hat{H}$ of a single particle is simply the kinetic energy operator (T) plus the potential energy (V) where the potential operator representing the Coulomb potential of the nuclear charge on the electron.

2.1.2 The Time-Dependent Schrodinger Equation

The time-dependent SE describes the system that evolves with time. Consider a particle of interest confined in one spatial dimension and introduce time dependency to SE.

We consider the total energy equation as below,

$$T+V(x) = E_{total} \tag{2.2}$$

where T, V, and E_{total} represent the kinetic energy, potential energy, and the total energy of the one-dimensional system respectively. From Equation (2.1), we get one-dimensional time-independent Schrodinger wave equation. Replacing Ψ(x) in Eq. (2.1) with Ψ(x, t), one obtains

$$\left[\left(\frac{-\hbar^2}{2m}\right)\frac{\partial^2\Psi(x,t)}{\partial x^2} + V(x)\Psi(x,t)\right] = \frac{-\hbar}{i}\frac{\partial}{\partial t}\Psi(x,t) \tag{2.3}$$

The LHS of equation (2.3) represents the Hamiltonian operator, $\hat{H}$, i.e.

$$\hat{H} = \left[\left(\frac{-\hbar^2}{2m}\right)\frac{\partial^2}{\partial x^2} + V(x)\right] \tag{2.4}$$

Comparing (2.3) in (2.4), we write,

$$\hat{H}\boldsymbol{\Psi} = \frac{-\hbar}{i}\frac{\partial}{\partial t}\boldsymbol{\Psi}(x,t) \tag{2.5}$$

Since SE is a partial differential equation for Ψ(x, t) that is a function of two variables, we apply the separation of variables as follows.

First, we introduce a separation constant

$$C = X(x)T(t)$$

Such that,

$$C = \psi(x)f(t) \tag{2.6}$$

Now, using (2.1.4) in the SE, we get

$$\frac{1}{\boldsymbol{\Psi}(x)}\hat{H}\boldsymbol{\Psi}(x) = \frac{i\hbar}{f(t)}\frac{d}{dt}\boldsymbol{f}(t) \tag{2.7}$$

Since any variation in x in the LHS of equation (2.7) is independent of our result in the RHS and vice versa, then both sides of (2.7) are equal and equivalent to a separation constant. Thus from (2.7), we realize two separate ordinary equations.

$$\frac{i\hbar}{f(t)}\frac{d}{dt}\boldsymbol{f}(t) = \boldsymbol{Constant} \tag{2.8}$$

Integrating (2.1.8) on both sides yields

$$\boldsymbol{F}(t) = e^{\frac{-iEt}{\hbar}} \tag{2.9}$$

Now, utilizing (2.9) in (2.6) gives

$$\boldsymbol{\Psi}(x,t) = \boldsymbol{\Psi}(x)e^{\frac{-iEt}{\hbar}} \tag{2.10}$$

which is an equation with time evolution.

In this case, the equation 2.1 has been modified to include time dependence. This equation can be modified to account for many-particle systems [3].

2.2 MANY-PARTICLE SYSTEMS

The Schrödinger equation can only be solved exactly for a single particle system such a hydrogen atom or model systems such as a particle in a box, the simple harmonic oscillator. It is difficult to solve SE explicitly for many-body systems due to interaction between the particles. For many particle systems, it is possible to obtain solution by choosing suitable approximations. Consider N-electron system of q nuclei and N electrons represented below,

$$\hat{\mathrm{H}}\Psi(R_1, R_2, ...R_N, r_1, r_2, ...r_q) = E\Psi(R_1, R_2, ...R_N, r_1, r_2, ...r_q) \tag{2.11}$$

where $\hat{\mathrm{H}}$ is the Hamiltonian operator of the system. The hamiltonian operator is the sum of kinetic energy and potential energy of the system, E represents the energy eigenvalue of the system, and $\Psi(R,r)$ the wave functions that describe the state of the many-body system. R_i denotes the nuclear positions and r_i denotes the electron positions. A detailed description of the Hamiltonian operator is shown in equation (2.12). Typically, the many particle SE is solved within the Born-Oppenheimer approximation which the first step in simplifying the problem by separating the electronic and nuclear degrees of freedom. Such a separation is possible due to the large differences in the mass of nuclei and electrons. The approximation is valid for typical electronic structure calculations where the interest is in the ground state quantities, but it can fail in some cases, for example, when the electron jumps from one potential energy surface to another in the chemical reactions. For the problems studied in the present thesis, the BO approximation is well justified. Below we briefly discuss the BO approximation.

2.3 DENSITY FUNCTIONAL THEORY

2.3.1 Born-Oppenheimer (BO) approximations

The BO approximation is based on the large difference between the masses of the nuclei and electrons. The Hamiltonian of any system is given below,

$$\hat{\boldsymbol{H}} = \hat{\boldsymbol{T}}_{\boldsymbol{n}} + \hat{\boldsymbol{T}}\boldsymbol{e} + \boldsymbol{V}_{\boldsymbol{ee}} + \boldsymbol{V}_{\boldsymbol{en}} + \boldsymbol{V}_{\boldsymbol{nn}} \tag{2.12}$$

where $\hat{T}_n$, and $\hat{T}e$ are kinetic energy operators for nuclei and electrons, V_{ee} is the electron-electron repulsive potential energy, V_{en} is the electron-nuclei electrostatic potential energy, and V_{nn} is the interaction energy due to the nuclei. Equation (2.11) is expressed explicitly as below,

$$\hat{H} = -\sum_{I=i}^{q} \frac{\hbar^2}{2M_I} \nabla_I^2 - \sum_{i=1}^{N} \frac{\hbar^2}{2m_e} \nabla_i^2 + \frac{e^2}{2} \sum_{i=1}^{N} \sum_{j \neq i}^{N} \frac{1}{|r_i - r_j|} - e^2 \sum_{I=1}^{q} \sum_{i=1}^{N} \frac{Z_I}{|R_I - r_i|} + \frac{e^2}{2} \sum_{I=1}^{q} \sum_{J \neq I}^{q} \frac{Z_I Z_J}{|R_I - R_J|} \tag{2.13}$$

where the order of the terms is as shown in equation (2.11). Z_I and M_I represent nuclear charges and masses respectively, R= $\{R_I, I=1,\ldots, q\}$ is a set of q nuclear coordinates, and r =$\{r_i, i=1,\ldots,N\}$ is a set of N electronic coordinates. $\hbar$ is the Planck's constant, e is the charge of an electron. The first two terms in the above equation are the kinetic energies of nuclei and electrons respectively, the third term represents the electron-electron repulsion while the fourth term is due to the attractive interaction between the electrons and nuclei. The last term is the nuclear-nuclear repulsion.

The BO approximation can be explained using the case of hydrogen atom. The nucleus of hydrogen has only a proton which is 1836 times heavier than its electron. This generally means that the nuclei of the systems are heavy and move much slower compared to the electrons. We thus consider the motion of the electrons and nuclei to be independent of each other. With BO approximations, we take the kinetic energy of the nuclei to be zero and the potential energy due to the nucleus to be a constant [4].

Our new H becomes;

$$\hat{H} = \hat{\boldsymbol{T}}_{\boldsymbol{n}} + \hat{H}_{el} \tag{2.14}$$

$$\hat{H} = -\sum_{I=i}^{q} \frac{\hbar^2}{2M_I} \nabla_I^2 - \sum_{i=1}^{N} \frac{\hbar^2}{2m_e} \nabla_i^2 + \frac{e^2}{2} \sum_{i=1}^{N} \sum_{j \neq i}^{N} \frac{1}{|r_i - r_j|} - e^2 \sum_{I=1}^{q} \sum_{i=1}^{N} \frac{Z_I}{|R_I - r_i|} \qquad (2.15)$$

Here, $\hat{H}_{el}$ is the electronic Hamiltonian which is represented by the last three terms in equation (2.15). $\hat{H}_{el}$ depends parametrically on nuclear coordinates, but derivatives with respect to these coordinates do not. Therefore, the electronic problem can be solved for nuclei that are momentarily fixed in space. Using (2.11), we can write

$$\vec{H}_{el}(N,M)\Psi_{el}(N,M) = E_{el}(N,M)\Psi_{el}(N,M)$$

where N and M are the electronic and nuclear coordinates.

We form a separable function by writing a total Born-Oppenheimer wave function as a product of nuclear and electronic wave functions as shown below.

$$\Psi_{BO}(N,M) = \psi_{nuc}(N)\Psi_{el}(N,M)$$

The electronic wave function has a parametric dependence on the nuclear positions. The electrons, in this approximation instantaneously follow the nuclear motion adiabatically, that is, the electrons are towed with nuclei without requiring a finite relaxation time. The large mass difference electrons and nuclei also results in the spatially localized nuclear components of the wave function as compared to the electronic component. In the classical limit, the nuclei can be presented as single classical point charges. For all the properties studied in this thesis, the BO approximation is an excellent approximation and all results reported in this thesis are performed within this approximation where the nuclei are parameters (classical point charges) that enter the electron Hamiltonian.

2.3.2 Evolution of density functional theory (DFT)

In order to simplify the many body problem, Thomas and Fermi [5, 6], (TF) in the 1920s put forth a model to describe atoms as uniformly distributed electrons around nuclei in a six dimensional phase space (momentum and coordinates). This allows the total energy of the system to be written in term of the electron density resulting in an enormous simplification of the many body problem. They formulated DFT to address difficulties associated with Hartree and Hartree Fock. The entire field of density functional theory rests upon two theorems proven by Hohenberg and Kohn in 1964 [7]. While generalizing this theory to any type of electronic system, they expressed the electronic Hamiltonian in equation (2.15) as below,

$$\hat{H}_{el} = -\sum_{i=1}^{N} \frac{\hbar^2}{2m_e} \nabla_i^2 + \sum_{i=1}^{N} V_{ext}(r_i) + \sum_{i=1}^{N} V_{avg}(r_i) = \hat{H}_{eff} \qquad (2.16)$$

where $\hat{H}_{eff}$ is basically the effective Hamiltonian operator for non-interactive electron case. $V_{ext}(\boldsymbol{r})$ and $V_{avg}(\boldsymbol{r})$ is the external potential energy and the average potential energy caused by the rest of the electrons. The expression for equation (2.16) can be expressed as below,

$$\hat{H}_{eff} = -\sum_{i=1}^{N} \frac{\hbar^2}{2m_e} \nabla_i^2 + \sum_{i=1}^{N} V_{eff}(r_i) \qquad (2.17)$$

which is summarized in Hohenberg-Kohn theorems.

2.3.2.1 The Hohenberg-Kohn Theorems

The modern density functional theory is founded on two theorems put forth by Hohenberg-Kohn [8, 7]. The first theorem states that for any system of interacting particles, the ground state energy of a system of fermions is a unique functional of its charge density. In an external potential, the ground state charge density $\boldsymbol{\rho}(\boldsymbol{r})$ determines the external potential $V_{ext}(r)$ completely. Since, in turn $V_{ext}(r)$ fixes $\hat{H}_{eff}$, we see that the full many particle ground state is a unique functional of $\rho(r)$. Therefore, there cannot be two different $V_{ext}(r)$ that give the same $\rho(r)$ for their ground state.

The ground state charge density $\rho(r)$ thus determines the number of electrons N and $V_{ext}(r)$, and hence all the ground state properties ($T[\rho]$, $V[\rho]$, and $E_{Total}[\rho]$). Hohenberg and Kohn thus

proved the determination of the ground state energy, wave function Ψ, and all other molecular properties uniquely from the exact electron density ρ(r).

The second theorem states that the functional attains its minimum when the density has the correct ground state charge density of that system. According to this theorem the energy functional E[ρ] that yields the ground state (lowest) energy if and only if the input charge density is the true ground state density [9]. Therefore, E[ρ] is defined by the ground state charge density ρ(r) for any $V_{ext}(\boldsymbol{r})$. The true/exact ground state charge density that delivers the global minimum value of E[ρ] is $\rho(r_0)$. According the HK theorems the ground state density contain all possible information about the system as the wavefunction in the Schrodinger theory.

2.3.2.2 The Kohn-Sham method

Kohn and Sham made DFT more feasible [10] by formulating the ground state charge density of the interacting particles as equivalent to that of non-interacting one. The ground state charge density of fictitious non-interacting particles opened new grounds for independent particle equations that are solved exactly.

In the Kohn-Sham formalism the particles (electrons) interact with each other through a common effective potential given by

$$V_{eff}(r_i) = V_{ext}(\boldsymbol{r}) + V_H(\boldsymbol{r}) + V_{XC}(\boldsymbol{r}) \qquad (2.18)$$

$V_H(\boldsymbol{r})$ is the Hartree potential and $V_{XC}(\boldsymbol{r})$ the exchange-correlation potential is obtained as the functional derivative of the unknown functional of the exchange energy,

$$V_{xc}(\boldsymbol{r}) = \frac{\delta E_{xc}[\boldsymbol{\rho}(\boldsymbol{r})]}{\delta \boldsymbol{\rho}(\boldsymbol{r})} \qquad (2.19)$$

For a single particle,

$$\hat{H}_{KS} = -\frac{\hbar^2}{2m}\nabla^2 + V_R(r)$$

which is one-electron Hamiltonian of single particle orbitals $\varphi_i(r)$ that gives N lowest energy eigenfunctions. The solution to the one-electron Schrodinger equation is shown below,

$$\hat{H}_{KS}\ \varphi_i(r) = E_i\ \varphi_i(r)$$

Therefore, the Kohn-Sham energy functional is given by,

$$E\ [\boldsymbol{\rho}(\boldsymbol{r})] = T_R[\rho(r)] + \int \rho(r) V_{ext} dr + \frac{1}{2}\iint \frac{\rho(r)\rho(r')}{|r-r'|\,\delta}\ dr'dr' + E_{xc}[\rho(r)] \qquad (2.20)$$

The first term at the right-hand side of this equation is the kinetic energy functional given by,

$$T_R[\rho(r)] = -\frac{\hbar^2}{2m}\sum_{i=1}^{N}\left\langle \phi_i \middle| \nabla^2 \middle| \phi_i \right\rangle$$

and the electronic charge density $\rho(r)$ is given by,

$$\rho(r)\ = \sum_{i=1}^{N} |\phi_i(r)|^2$$

The first three terms of the right-hand side in Eq. (2.20) have known analytical forms while the analytical form of the fourth term, exchange-correlation functional, is unknown.

2.3.3 The Exchange-Correlation Functionals

The major problem in solving the Kohn-Sham equations is that a true form of the exchange-correlation functional is undetermined with an exception of the free electron gas. Since the exact form of this functional is unknown, several approximations provide viable parameterization of the exchange-correlation potential (V_{xc}). Thus, accuracy of the density functional calculations depends on the accuracy of the approximations made for the exchange-correlation energy and functional.

The relationship between the exchange-correlation potential $V_{xc}(r)$ and the functional derivative of the exchange-correlation energy with respect to the electron density is shown in $Eq.(2.19)$. The efforts to determine the functional form of $E_{xc}[\rho(r)]$ exactly are on course. Several approximate functionals have been proposed over the past decades, the simplest of all being the local density approximation (LDA). In LDA, the value of $E_{xc}[\rho(r)]$ is determined by

the exchange-correlation energy of an electron in a uniform electron gas of the same electron density $\rho(r)$ [11]. The equation below assumes the relationship where the exchange-correlation energy is expressed as a function of the exchange-correlational functional per electron gas, ε_{xc} particle.

$$E_{xc}^{LDA}[\rho(r)] = \int \rho(r)\varepsilon_{xc}[\rho(r)]dr$$

The LDA exchange-correlation functional centrally depends on the position of electron density only, i.e. it is a functional of the local value of the electron density at each point in space regardless of any other information. The mathematical expression for the correlation term within LDA was first reported by Vosko et. al. [12]. More sophisticated approximations such as generalized gradient approximations (GGA), the approximations that depend on the kinetic energy density of electrons- meta-GGA etc have been proposed and are widely used. For the simulations performed in this thesis we have used the GGA approximation. One route to improve the performance/accuracy of the calculations is to include some fraction of the Hartree-Fock exchange in the exchange-correlation term. This approach goes beyond the standard Kohn-Sham approach as the Hartree-Fock exchange is nonlocal and orbital dependent. Such equations are usually solved within the generalized Kohn-Sham scheme.

2.3.4 Pseudopotentials and Plane Wave Basis Set

Plane waves are used in calculations that involve periodic boundary conditions because of Bloch's theorem [13]. This theorem uses the periodicity of a crystal structure to reduce the infinite number of one electron wavefunctions to the number of electrons in a unit cell of the crystal. A unit cell is the smallest and simplest repeating unit that has the full symmetry of a given crystal structure. The repeating unit cell that contains the primitive cell forms the supercell. For calculation of the isolated molecule using a periodic boundary condition, the simulation box is made large, enough to avoid spurious interactions between periodic images.

The DFT codes such as VASP utilize plane wave basis sets in combination with pseudopotentials [14]. All electron implementations using plane wave basis sets is not realistic due

to the need of very large number of plane waves needed. Therefore, the plane waves are used to describe the valence electrons in combination with effective potential or pseudopotential. The pseudopotentials or effective potentials account for the effects caused by the core electrons and the nuclei [15, 16]. Throughout my thesis project, I have used VASP as my methodical approach. In the next section, some aspects of the VASP are explained.

2.4 VASP

The Vienna Ab initio Simulation Package (VASP) is a computer program for atomic scale materials modeling. It was initially written by Mike Payne at the Massachusetts Institute of Technology. Others who contributed to VASP development include J. Hafner, J. Furthmüller, and G. Kresse [1, 2, 17]. The VASP code solves a variety of problems including electronic structure calculations and quantum mechanical molecular dynamics from first principles. It is a DFT code that employs periodic boundary conditions in all its three spatial coordinates. In our calculations, however, the periodicity is only along x and y-directions for the surfaces and interfaces. The z-direction is chosen to the direction normal to the surface. Five layers are were found to be sufficiently thick to model the surface. The bottom layer was fixed to mark the periodicity in the z-direction.

The fullerene/$MAPbI_3$ and fullerene derivatives/$MAPbI_3$ interface were separated by a vacuum region which was chosen in such way that there was no interaction between the surface and its images. This region was no less than 20 Å and 23 Å for PbI_2T and MAIT surfaces respectively. The detailed parameters utilized in our VASP calculations follows as described in their respective input files and computational details section.

2.4.1 VASP INPUT Files

The followings are the four central input files that must exist in a working directory for a VASP calculation to be executed.

INCAR file

This file is responsible for 'what to do and how to do.' The file has many parameters by default which makes it longer. The user is encouraged to leave them as default if not sure. The following are the INCAR flags and their meaning.

1. SYSTEM

This tag defines the name for the system under investigation. The name provided does not affect the computations or any sort of the outcome, but it is for users to make a comment about their calculation. Typically, the name of the material or structure description is given. Most people don't change this name whenever they decide to perform other different calculations since it is independent of the results. It's always the first line in the INCAR file.

2. NWRITE

The NWRITE flag determines how much information is written to the output file usually found in the OUTCAR file. The possible NWRITE value ranges from 0 to 4. The NWRITE=0 or NWRITE=1 should be used when running a molecular dynamics (MD) calculation. The NWRITE=2 is utilized for short runs and is usually the default value. In case when a calculation goes wrong, setting NWRITE=3 may provide a user some useful information. NWRITE=4 is used for debugging purposes only. This NWRITE values thus dictates the amount of information be written in the OUTCAR file. Such information includes forces, stress, eigenvalues, charge density, total energy and convergence, and the timing information. We use the value 2 in this work.

3. ENCUT

The ENCUT (E_{cut}) tag specifies the plane-wave basis cutoff energy in eV. The basis set only allows those plane-waves whose kinetic energy is less than E_{cut}. The mathematical expression is shown as

$$|G + K| < G_{cut}$$

$$E_{cut} = \frac{\hbar^2}{2m} G_{cut}^2$$

This choice of E_{cut} value is set in such a way that the total energy converges with respect to the plane-wave-basis size. The default value of ENCUT is always set to ENMAX in the POTCAR file. If the POTCAR has more than one element, the maximum cutoff becomes ENMAX of the calculation. Since our molecules have several elements, we set the ENMAX value and provide it in the INCAR file. This value also varies depending on the accuracy and type of the calculation.

4. ISPIN

The ISPIN tag is used to determine whether spin-polarized calculations are to be performed. The ISPIN values are 1 or 2 where ISPIN=1 means non-spin polarized calculations while SPIN=2 is for spin-polarized. Magnetism can be studied if the MAGNOM tag is combined with ISPIN. In this case, we set MAGNOM =1.

5. ISTART

The ISTART flag determines whether to read the file WAVECAR or not. The set-up is to be started from scratch or restarted from information acquired from a previous job. The default value of ISTART is 0 if no WAVECAR from a previous job is present. This setting instructs VASP to start a job from scratch with an initial guess for the charge density. If the previous job did not converge and a WAVECAR was written-out, the default value of ISTART used is 1. Here, the VASP will continue with the calculation by reading the wavefunction solutions to the Kohn-Sham equations from the WAVECAR file written after an earlier job, to produce an initial charge density.

This helps reducing the time to reach convergence since the charge density from the wavefunction solutions is typically close to the converged wavefunctions.

6. IBRION

When performing a geometry optimization, we are in a constant search for the global minimum energy that provides the most stable structures as described in the previous section i.e. a system at the most stable state. During this process of atomic relaxation, the IBRION tag is used to instruct VASP on how to move and update the ionic positions. The right choice for the most appropriate minimization algorithm is very vital for efficiently finding the global minima. The IBRION values range from -1 to 8 and then 44. Their meanings and tag values are described below.

➢ IBRION=-1: single SCF calculation. There is no update and ions are not moved, but NSW is performed in the outer loop. NSW defines the number of ionic steps.

➢ IBRION=0: a standard ab-initio molecular dynamic calculation is performed.

➢ IBRION=1: the RMM-DIIS algorithm is used [18]. The details of the algorithm are discussed in the next section.

➢ IBRION=2: initializes the optimization algorithm to conjugate gradient algorithm. We utilize this algorithm in our calculations. It is used to relax the ions into their instantaneous ground state [19]. The details of the algorithm are discussed in the next section.

➢ IBRION=3: uses damped molecular dynamics. The POTIM value must be chosen reasonably. Large POTIM values may result in divergence, while too small ones slow down the convergence.

➢ IBRION=5 and IBRION=6 are only supported by VASP versions 4.5 and 5.6 respectively. They both determine the Hessian matrix and the vibration frequencies. The finite difference is used in the calculation of the Hessian matrix where every ion is displaced in the direction of each Cartesian coordinate and Hessian matrix finally determined from the forces.

7. POTIM

The POTIM tag serves as a scaling constant for the forces of the minimization algorithms IBRION=1, 2, and 3 in VASP. For IBRION=0, i.e. molecular dynamics, POTIM determines the time step in femtoseconds (fs).

8. EDIFF

The EDIFF simply specifies the SCF tolerance, which is the allowed error in the total energy, of the system. The tag specifies the break condition for the electronic self-consistent loop. This loop is demonstrated in the inner loop of the VASP flowchart. The relaxation of the electronic degrees of freedom stops whenever the total energy change between two electronic steps are both smaller than the set value of the EDIFF. The default value is always set to EDIFF=10^{-4}. In this default case, the total energy obtain has accuracy of 4 significant figures.

9. EDIFFG

The EDIFFG simply means the break condition for the ionic relaxation loop. This loop is demonstrated in the outer loop of the VASP flowchart below. If the value of EDIFFG is positive, the relaxation will be stopped when the change in the total energy is smaller than EDIFFG between two ionic steps. If the value of EDIFFG is negative, the relaxation will be stopped when all the forces are smaller than |EDIFFG|. The negative value is usually most preferred. The default value of EDIFFG=EDIFF×10. If the EDIFFG is set to 0, the ionic relaxations will stop when all the NSW steps are completed.

10. LWAVE

The LWAVE tag takes logical value of TRUE or FALSE and determines whether or not the wave function solutions to the Kohn-Sham equations are written to the output file as WAVECAR file. The WAVECAR file can be used to continue the calculations if the calculations stopped before the set threshold of EDIFF and/or EDIFFG or before convergence. However, the

WAVECAR file can be large, order v10 MB to v1GB, and could require large amounts of storage. The default value is LWAVE=.TRUE.

11. LCHARG

The LCHARG determines whether (TRUE) or not (FALSE) the charge densities are written to the output CHG and CHGCAR file. The CHGCAR file can be used to compute the band structure and (local) density of states or (L) DOS.

12. NSW

The NSW tag sets the maximum number of ionic steps. The default is always NSW=0. If the EDIFF convergence threshold is not met before, at most NELM electronic self-consistent loops will be performed within each ionic step. The exact Hellmann-Feynman forces and stresses are calculated for each ionic step.

POSCAR file

The POSCAR file contains the geometry information. It includes the lattice geometry and ionic positions. This file may contain velocities if it's copied from its corresponding output file called CONTCAR. An example of the POSCAR file is shown in Figure 2.1.

```
MA-Pb-I
1.0
      18.8703613281     0.0000000000       0.0000000000
       0.0002330819 18.8216705308 0.0000000000
      -0.2605156557               -0.0010100316
50.3548122154

 C    N     H      Pb   I
36   36   216   27   90
Selected dynamics
Cartesian
    5.667712521        0.004278237        6.201503400   F F F
    5.667867909       12.552056121        6.201503400   F F F
    5.667790215        6.278167439        6.201503400   F F F
   18.247952094        0.004278237        6.201503400   F F F
   18.248108607       12.552056121        6.201503400   F F F
   18.248029788        6.278167439        6.201503400   F F F
   11.957832026        0.004278237        6.201503400    F F F
   11.957987414       12.552056121        6.201503400    F F F
   11.957909720        6.278167439        6.201503400    F F F
    5.584365928       12.523313902       12.502235380  T T T
    5.584288234       6.249425221       12.502235380    T T T
    5.584443622       18.797204827       12.502235380  T T T
   18.164606064       12.523313902       12.502235380  T T T
```

Figure 2.1: A section of a POSCAR file for $MAPbI_3$ surface.

The first line in POSCAR is always a comment line similarly to the SYSTEM tag in the INCAR. This line may be used for labeling the simulation. In Figure 2.1, our first line is described by "MA-Pb-I", an acronym that reminds us that our system is methylammonium lead Iodide. The second line is a universal scaling factor. We put the scaling factor as 1.0. Next three lines represent three lattice vectors that define the size of a unit cell. The sixth and seventh lines show the type and number of atoms per species constituting the system under study. The order of atoms is very significant and should be consistent with the order in which the pseudopotentials are stored in the POTCAR file. The eighth line is like the control since it determines the atoms that will be fixed (F) or relaxed (T). The coordinates can either be Cartesian or fractional.

POTCAR file

This file contains all the required PAW datasets for all atomic species specified in the POSCAR. For instance, when working on $MAPbI_3$, we concatenate the POTCAR files of Carbon, Hydrogen, Nitrogen, Lead, and Iodine in the same order as in the POSCAR file. If only one species is used, then concatenation is not required. POTCAR file also contains the atomic masses, valence, the cut-off energy (ENMAX and ENMIN) for each species among other features. The energy tag should be left as default in the INCAR file. In fact, in POTCAR file, no alteration is required. Every data set should be used as supplied by VASP. The only thing required is the order of concatenation for the species in the calculation.

KPOITS file

The KPOITS file contains all the information regarding the K-point coordinates and weights for creating the K-point grid. We use the automatic K-mesh generation method. The method only requires the input of a division of the Brillouin zone in every direction and the origin of the K-mesh. An illustration of this file is shown below.

Automatic mesh

0

Monk horst pack

1 1 1

0 0 0

The first line of the KPOINTS file is treated as a comment line. The second line represents the number of k-points. In this example, the value given is '0', which has no meaning for the number of k-points and thus the value activates the automatic generation scheme. The third line is the type of automatically generated mesh which is Monkhorst-Pack throughout this thesis project. The fourth line indicates the number of k-point divisions to be taken along each reciprocal lattice vector. During K-point convergence, the number of k-points (i.e. divisions) is always varied until the total energy converges. In our simulations we checked the convergence of the total energy with respect to number of electrons. Since the simulation cells employed were rather large, a single k-point (Gamma point) was enough in most cases. It should be noted that as the unit cell increases in size, the size of the Brillouin zone, or reciprocal lattice unit cell, decreases in size. Therefore, in real space, larger cells require fewer k-points to sample the smaller reciprocal space.

2.4.2 OUTPUT Files

VASP produces several output files. The following are some of the important output files selected for description.

CONTCAR File

The format of this file is very similar to that of POSCAR. This file is usually used when jobs continuation is desired from the previous executions. It contains the information regarding actual coordinates, velocities and predictor-corrector coordinates that could be desired for next runs. It also contains the positions of the last ionic step of the relaxation runs. In the case of

unconverged relaxation runs, we need to copy CONTCAR to POSCAR before continuing. CONTCAR can be considered as a snapshot of the POSCAR file.

OSZICAR File

OSZICAR is the file with a detailed information regarding the following:

• A summary of the self-consistency cycle.

• Convergence of energy and charge density.

• Total energies and the total magnetic moment of the cell.

• Forces.

• Convergence speed and the current steps.

The Figure 2.2 shows a section of our OSZICAR file.

```
   N      E                    dE             d eps       ncg     rms          rms(c)
DAV:   1    0.883950268631E+04    0.88395E+04   -0.36292E+05  4352   0.719E+02
DAV:   2    0.316343690245E+03   -0.85232E+04   -0.81138E+04  5904   0.171E+02
DAV:   3   -0.136156896916E+04   -0.16779E+04   -0.16657E+04  5296   0.791E+01
DAV:   4   -0.144336391417E+04   -0.81795E+02   -0.81522E+02  5824   0.214E+01
DAV:   5   -0.144553893549E+04   -0.21750E+01   -0.21696E+01  5872   0.355E+0
```

Figure 2.2: Our OSZICAR file

2.5 SIESTA

Studies performed in herein could also haven been carried out with alternative simulation software. An example of which is SIESTA code [20]. SIESTA [21], is an acronym for Spanish Initiative for Electronic Simulations with Thousands of Atoms. This program has the capabilities of performing electronic structure calculations and ab initio molecular dynamics of molecules and solids. SIESTA utilizes a linear combination of atomic orbitals (LCAO) basis set [22, 23] while VASP utilizes a plane wave basis set. Just like plane-wave codes do, SIESTA uses pseudopotentials within the calculation of the electron-ion interactions. The type of pseudopotentials utilized in SIESTA is the "norm-conserving" type generated by the Pseudo which is the atomic program. What follows are the general characteristics of the SIESTA software package;

- It utilizes local density (LDA-LSD) and generalized gradient approximations (GGA) as formulated in the Kohn-Sham self-consistent density functional method. It also encompasses non-local functional with Van der Waals interactions (VDW-DF).
- Their fully non-local form uses norm-conserving.
- Both serial and MPI parallel compilation.
- It is written in Fortran 95, and memory is allocated dynamically.
- Has real-space grid projection for both electron wave functions and density.
- Uses atomic orbitals as a basis set.

SIESTA versions 3.0 and up have the TRANSIESTA module that enables the capabilities for models that applies to open-boundary systems. With TRANSIESTA module, one can calculate the electronic properties such as the I-V characteristics and zero bias conductance [24]. The electron density is computed using non-equilibrium Green's Function (NEGF) method within DFT.

2.6 QUANTUM ESPRESSO

This software package is one of the most widely used open source software. It is a density functional implementation using plane wave basis set and pseudopotentials. It also allows Car-Parrinello molecular dynamics (CP) simulations.

2.7 COMPUTATIONAL DETAILS

We relax all our structures using VASP. The projector augmented wave (PAW) method is utilized to model electron-ion interaction [25, 26, 27]. We consider 2S2 2P2, 2S2 2P3, 1S1, 6S2 6P2, and 5S2 5P5 as the electronic orbitals for the valence states of C, N, H, Pb, and I respectively. We optimize our structures first at $\Gamma-$ centered (1x1x1) k-grid point for relatively faster and accurate optimization. The cut-off energy during this process is set to 400eV. This K-mesh is based on the Monkhorst-Pack scheme [28] at the gamma point. The structural optimization is performed using conjugate-gradient algorithm until the Hellmann-Feynman forces are smaller than 0.01eV/Å. We set the kinetic energy for the plane-waves to be 400eV while the convergence criterion for electronic self-consistent loop utilized is 10^{-8} eV.

2.8 ALGORITHMS USED IN VASP

We use VASP in determining the most stable structures. The process starts by optimizing the atomic positions and obtaining the ground state charge density that minimizes the energy for our configured systems. VASP has the capability of solving the Kohn-Sham equations self-consistently with an iterative diagonalization coupled with Pulay mixing method [18, 29] for charge density. The overall process can be summarized in two steps: the first one involves the refinement of the charge density and wavefunctions while the other one is the optimization of the atomic positions. This process is made efficient with the implementation of some algorithms that utilize the iterative matrix-diagonalization scheme in VASP. We now briefly describe some algorithms implemented in VASP with slightly more details provided for the conjugate gradient.

2.8.1 Conjugate Gradient.

One of the algorithms used in VASP for the refinement of the wavefunctions and charge density is the conjugate gradient scheme [30, 31]. This algorithm utilizes the current and previous information to construct a search direction that would be conjugate to the previous one. The successive number of conjugate gradient steps helps in optimizing the expectation value of the Hamiltonian. The details of the conjugate gradient algorithm can be found in Ref [32, 33, 34]. We describe the algorithm in steps as below, from a mathematics point of view in determining the convergence. We later apply the scheme in the optimization procedures as used in VASP.

We consider the conjugate gradient to be efficient for the systems of the form

$AX = b$

where x is an unknown vector, b is a known vector, and A is a known symmetric positive-definite and square matrix of nxn. Thus we can write

$$A = A^T$$

where A^T represents the transpose matrix of A.

We also note that any two vectors, say u and v, are said to be conjugate with respect to A if

$$u^T Av = 0 .$$

By the symmetric relation, we further state that if u is conjugate to v, then v is also conjugate to u.

Since we are using the conjugate gradient method as the iterative method, we need a better initial guess to realize the convergence in fewer steps. The choice for the conjugate vectors p_k is paramount. A better p_k choice helps realize a good approximation to the solution with fewer conjugate vectors.

Suppose we denote the initial guess for x_+ by x_0. We approximate x_0 to 0. Now starting from x_0, we search for the solution in each iteration and compare with x_+. The metric is evaluated to check whether the solution obtained is closer x_+ . The metric also helps us to confirm that x_+ is also a unique minimizer of the function $f(x)$ below.

$$f(x) = \frac{1}{2} X^T AX - X^T b$$

If the minimizer of $f(x)$ is very small or closer to zero in a given iteration, then it will be getting closer to x_+. The gradient of f(x) is given by

$AX_0 - b$ while $p_0 = AX_0 - b$ since our initial guess is estimated as x_0.

This leads us to the determination of the residual. We denote the residual for k steps as r_k .

$$r_k = AX_k - b$$

The value for r_k is always of a negative gradient of a function $f(x)$ at x = x_k.

If we take our first search direction to be r_0 at x = x_0, we have its residue expressed as,

$r_0 = AX_0 - b$.

Then next search direction can be built out of the current residue. The preceding residues will also be built based on their current residues and all previous search directions until r_k .

The conjugate gradient constraint is an orthonormal-type constraint and hence the algorithm such as Gram-Schmidt orthonormalization can be expressed as,

$$p_k = r_k - \sum_{i<k} \frac{p_i^T A r_k}{p_i^T A P_i} P_i$$

With this direction noted, the next optimal position is given by

$$X_{k+1} = X_k + \alpha_k p_k$$

where

$$\alpha_k = \frac{p_k^T b}{p_k^T A p_k} = \frac{p_k^T (r_{k-1} + AX_{k-1})}{p_k^T A p_k}$$

$$\alpha_k = \frac{p_k^T r_{k-1}}{p_k^T A p_k}$$

thus

$$\frac{p_k^T (r_{k-1} + AX_{k-1})}{p_k^T A p_k} = \frac{p_k^T r_{k-1}}{p_k^T A p_k}$$

since pk and x_{k-1} are conjugate.

Since the algorithm shows r_{k+1} to be conjugate to pi for all i < k, then only r_k , p_k , and x_k are needed to construct r_{k+1} , p_{k+1} , and x_{k+1} . We, therefore, need only one matrix-vector multiplication in each iteration. This way makes the process less complicated and computationally economical, otherwise, we would have stored all the search directions used and residue vectors which would be computationally expensive.

2.8.2 Block Davidson scheme

The Block Davidson scheme [35, 36] is one of the iterative matrix-diagonalization schemes implemented in VASP. The flag IALGO in the INCAR file is set to 38 to activate this algorithm in VASP 4.5 versions and up.

2.8.3 Residual minimization scheme

The Residual minimization scheme-direct inversion in the iterative subspace (RMMDIIS) [37, 38] is also implemented in VASP and most often, combined with Block-Davidson Scheme.

In general, most algorithms used in VASP are similar since they all utilize the residual vector as the central quantity in the refinement. The only point of diversion for these algorithms is the way their algorithm implementation is incorporated with the residual vector. VASP treats these algorithms as “black boxes” giving the user very little control over the behavior of the algorithm. The method used for the computations in our work was the conjugate gradient. RMMDIIS combined with stable block Davidson scheme is also used but only at the initial stages of optimizations. There are two approaches employed into achieving optimization of the structures: static or dynamic computations and automated approach. Static or dynamic computations utilize several independent computations and consequently update the ionic positions manually. This method is used when determining the bulk structural properties for simple structures. To obtain the absolute minimum in total energy, the lattice constants are varied and fit into a parabolic

equation as a function of total energy. The approach applies to the simple structures that possess little or no internal parameters. The second approach, which is the method employed in our study, relies on a dynamic process where the positions are updated automatically during the computation process.

VASP utilizes the minimization of the free energy of the system with respect to the atomic positions to compute the forces. These forces are generally the derivative of the generalized free energy functional F, where F depends on the wavefunctions ψ, partial occupancies f, and atomic positions R. The variational property of this functional determines the ground state of the system. The variations with respect to ψ and f are expected to be 0 at the ground state. We provide the initial guess which serves as a starting point for our algorithms and optimization procedure follows as described in the algorithms above.

Thus, the force is defined as the derivative of the free energy functional F with respect to the atomic position R.

The $force = \frac{dF(\psi,f,R)}{dR} = \frac{\partial F}{\partial R}$

Once at the electronic ground state, the initial configuration of both ψ and f becomes constant. It's now easy to compute the force as the partial derivative of the free energy functional with respect to only atomic position. The problem is now simplified into minimizing the forces due to atomic positions into obtaining the final minimum energy configuration. There are three algorithms implemented in VASP to find this minimum force including the Quasi-Newton (DIIS) method, the conjugate gradient method and damped molecular dynamics. The difference in the methods being the way in which the algorithm determines the forces to update the atomic positions. In all cases, the configuration is at the minimum energy when the change in energy of the newly updated configuration, with respect to the energy of the previous configuration, has fallen below a certain value previously defined by the user.

REFERENCES

[1] J. Popp, Z. Lakner, M. H. Rakos and M. Fari, "The effect of bioenergy expansion: Food, energy, and environment," *Renewable and Sustainable energy Reviews,* vol. 32, pp. 559-578, 2014.

[2] A. Shah, P. Torres, R. Tscharner, N. Wyrsch and H. Keppner, "Photovoltaic Technology: The Case for Thin-Film Solar Cells," *Science,* vol. 285, no. 5428, pp. 692-698, 1999.

[3] "Facing the Hard Truths about Energy: Topic Paper No. 19," National Petroleum Council, 2007.

[4] "Bp Statistical Reviews of World Energy," British petroleum, 2006.

[5] G. J. Moridis, T. Collett, R. Boswell, M. Kurihara and M. ,. Reagan, "Toward Production From Gas Hydrates: Assessment of Resources, Technology and Potential," in *SPE UnconventionalReservoirs Conference*, Keystone, 2008.

[6] S. B. E. D. J. M. R. T. M. D. A. G. P. M. M. a. D. S. M. M. Hand, "Renewable electricity futures," *Golden, Co: National Renewable Energy Laboratory,* 2012.

[7] "Wood Mackenzie Power & Renewables," Q4 2018 US. PV.

[8] "Wood Mackenzie U.S. Solar Market Insight 2018 Year in Review".

[9] J. Liang, C. Wang, Y. Wang, Z. Xu, Z. Lu, Y. Ma, Y. H. Hongfei Zhu, C. Xiao, X. Yi, G. Zhu, H. Lv, L. Ma, T. Chen, Z. Tie, Z. Jin and J. Liu, "All-Inorganic Perovskite Solar Cells," *J. Am. Chem. Soc.,* vol. 49, no. 138, pp. 15829-15832, 2016.

[10] D. B. Mitzi, "Templating and structural engineering in organic–inorganic perovskites," *Royal Soc. Chem. ,* pp. 1-12, 2001.

[11] O. Selina and M. Klaus, "Substrate-dependent electronic structure and film formation of MAPbI3 perovskites," *Scientific Reports,* vol. 7, p. 40267, 2017.

[12] S. Nomura, R. Santoro, J. Fang and R. N, *J. Phys. Chem. Solids,* vol. 25, p. 901, 1964.

[13] R. Santoro, R. Newnham and S. Nomura, "Magnetic properties of Mn2SiO4 and Fe2SiO4," *J. Phys. Chem. Solids ,* vol. 27, no. 4, pp. 655-666, 1966.

[14] G. Lamarche, F. Lamarche and A.-M. Lamarche, "A possible 83K magnetic detector for high energy particles," *Physica B: Condensed Matter,* Vols. 194-196, pp. 219-220, 1994.

[15] A. M. Gagliardi, A. d. Maur, D. Gentilini, F. d. Fonzo, A. Abrusei, H. J. Snaith, G. Divitini, C. Ducati and A. D. Caelo, *Nanoscale,* vol. 7, pp. 1136-1144, 2015.

[16] J. Bisquert, "Nanostructured Energy Devices: Equilibrium Concepts and Kinetics," CRS Press, Boca Raton, 2014.

[17] X. Y. Zhu, *J. Phys. Chem. lett,* vol. 5, no. 13, pp. 2283-2288, 2014.

[18] Y. Okamoto and Y. Suzuki, "Perovskite-type SrTiO3, CaTiO3, BaTiO3 porous film electrodes for dye-sensitized solar cells," *J. Ceram. Soc. ,* vol. 122, pp. 728-731, 2014.

[19] J. B. I. M. S. a. G. G. B. T. Kirchartz, "Classification of solar cells according to mechanisms of charge separation and charge collection.," *Royal Soc. of Chem.,* pp. 10, 1039, 2015.

[20] D. Cahen and A. Kahn, "Electron Energetics at Surfaces and Interfaces: Concepts and Experiments.," *Adv. Mater.,* vol. 4, no. 15, pp. 271-277, 2003.

[21] "LibreTexts libraries are Powered by MindTouch® and are supported by the Department of Education Open Textbook Pilot Project, the UC Davis Office of the Provost, the UC Davis Library, the California State University Affordable Learning Solutions Program.".

[22] G. Nishant, A. Githin, P. Ramakrishna, S. Rajneel and P. K. F, Prospects of Nanostructure-Based Solar Cells for Manufacturing Future Generations of Photovoltaic Modules, 2009.

[23] "Photovoltaic Cells – Generating electricity," Images scientiific Instruments.

[24] S. Sharma, K.-K. Jain and A. Sharma, "Solar Cells: In Research and Applications," *Mat. Sci. Appl.,* vol. 6, pp. 1145-1155, 2015.

CHAPTER 3: PEROVSKITE-METALLOFULLERENE INTERFACE

3.1 INTRODUCTION

Methyl ammonium lead halide ($MAPbX_3$) perovskite based solar cells have recently emerged as a promising class of materials for photovoltaic applications with efficiencies reaching ~22%. The available experimental and theoretical studies have revealed that the superior photovoltaic performance of these materials is associated with their optoelectronic properties such as high charge carrier mobility, high optical absorption coefficient, low exciton binding energy, and low trap density [1]. A plethora of perovskite photovoltaic device architectures has been designed with improved power conversion efficiencies (PCE) ever since the pioneering work done by Kojima et. al. [2] using $CH_3NH_3PbI_3$ as visible-light sensitizers in photoelectrochemical cells. Recent reports indicate that the use of hybrid organic-inorganic lead halides, $MaPbX_3$ (MA = CH_3NH_3, X = Cl, Br and I) as semiconducting absorber layers can lead to PCEs of 22% in photovoltaic devices [3]. $MAPbI_3$ is currently one of the most widely used organic-inorganic hybrid perovskites with outstanding photovoltaic performance [4,5]. Its photon-to-current conversion ratio have greatly improved over the years with the solar cell efficiency reaching over 20% [4, 6, 7, 8]. $MAPbI_3$ is also a low cost [9], easily synthesized material that has excellent solution processability [10, 11], and therefore it is an interesting material for low energy fabrications [12]. Other characteristics that makes $MAPbI_3$ very competitive include, unique chemical-physical properties, charge carrier properties and mobilities, adjustable band gap [7] , and reduced bimolecular charge recombination [13] among others. Over the years, researchers have shown that $MAPbI_3$ offers tunable optical and electrical properties and has attracted attention due to their potential application non-linear optics and thermistors [14] apart from solar cells [2, 15, 16].

$CH_3NH_3PbI_3$ perovskite (abbreviated as $MAPbI_3$ perovskite) generally has two kinds of surfaces arising from different surface terminations; one terminated by the methyl ammonium iodide (abbreviated as MAI-T), and the other terminated with the PbI_2 (abbreviated as PbI_2 -T). The structural, electronic, and optical properties of perovskite surfaces and interfaces are crucial

in achieving high PCEs. Theoretical calculations have contributed significantly in providing useful insights into the fundamental structural and electronic properties of perovskite materials, their surfaces and interfaces. Numerous literature reports [17, 18, 19] underline the influence of specific surface terminations on the stability and water-induced degradation pathways of perovskite. Haruyama et. al. investigated the termination dependence on the structural stability and electronic states of various terminations of the tetragonal $MAPbI_3$ surfaces using density functional theory (DFT) calculations [20]. Using various types of PbI_x terminations with and without vacancy, they suggested that a vacant termination is more stable than flat termination under thermodynamic equilibrium conditions. First principle calculations by Geng et. al. has shown that while both terminations are effective solar energy absorbers in the visible light spectrum, MAI-T is thermodynamically more stable than the PbI_2-T [5]. The band gap of MAI-T decreases with increasing slab thickness, while the band gap of PbI_2-T is insensitive to slab thickness. Very recently, Quarti et. al. investigated the surface termination effects on the energies of the frontier crystal orbitals in $CH_3NH_3PbI_3$ perovskite and reported that PbI-terminated surface shows valence and conduction band edge energy approximately 1 eV below the corresponding levels in the MAI-terminated surface. Car–Parrinello molecular dynamics simulations [21] used to understand the perovskite-water interfaces indicate that MAI-terminated surfaces are easily prone to solvation while PbI-terminated surfaces are more resistant to water degradation.

Typically, in perovskite solar cells, the perovskite layer where the photon conversion takes place, is sandwiched between an electron transport layer (ETL) and a hole transport layer (HTL) which consist of either organic, inorganic, or a combination of both organic and inorganic materials [22]. Various perovskite solar cells with both mesoporous and thin-film architectures are devised where the perovskites are interfaced with different electron transport materials and hole transport materials [5]. Although the bulk properties of perovskite are important, the interface between the perovskite and the charge transport layers is also critical for efficient charge transport and hence solar cell efficiency. Immense efforts have gone into the development and understanding of interfacial engineering between perovskite and ETLs for effective charge carrier

separation [23]. Semiconducting metal oxides such as ZnO and TiO_2 are widely employed as ETLs to facilitate electron transport in planar heterojunction devices. The widespread use of fullerene-derivatives as acceptors in organic electronics has motivated the test of different fullerene derivatives as ETLs in perovskite solar cells. Fullerene layers deposited on the top of the perovskites reduce the charge trap density by several orders of magnitude, eliminating the photocurrent hysteresis, and doubling the power conversion efficiency of $CH_3NH_3PbI_3$ solar cells [24, 25]. Jen and coworkers showed a clear correlation between the electron mobility of fullerenes and the resulting performance of derived devices and demonstrated that the high electron mobility of fullerene derivatives effectively promotes charge dissociation and charge transport making them promising ETLs [26]. Recent reports indicate that phenyl-C_{61}-butyric acid methyl ester ($PC_{61}BM$) can be used as an excellent alternative to metal oxide layers since it provides more efficient charge extraction from perovskite than metal oxides [27, 28] . DFT simulations by Quarti et. al. on the interface between $MAPbI_3$ and C_{60} have shown that there is an uplift in the electronic level of C_{60} on interaction with MAI-terminated surfaces due to the electron transfer from perovskite to C_{60} whereas a downshift is observed in the case of PbI-terminated surfaces [4]. Zhang et. al. recently showed that perovskite solar cells using methanofullerenes (C_{61}PCBM and C_{71}PCBM) as ETMS exhibit higher power conversion efficiencies compared to the ones using pristine fullerenes [29] .

The perovskite-fullerene interface is expected to vary depending on the type of fullerenes used as the ETL. In this work we use DFT calculations to provide insights into the energetics and interface formation between the perovskite layer and fullerene derivatives in MAI- terminated surface of $MAPbI_3$. We have chosen endohedral metallofullerene and its PCBM-analogue namely, $Sc_3N@C_{80}$ and $Sc_3N@C_{80}$PCBM because of their outstanding electronic and photophysical properties as well as their use as efficient electron acceptors in organic photovoltaic cells. The charge separations and charge collections at the interfaces are also investigated. The interfacial characteristics and the effect of endohedral metallofullerene derivatives on perovskite electronic properties revealed from this work can help in determining the effectiveness of the fullerenes as an electron transporting layer in the perovskite solar cells.

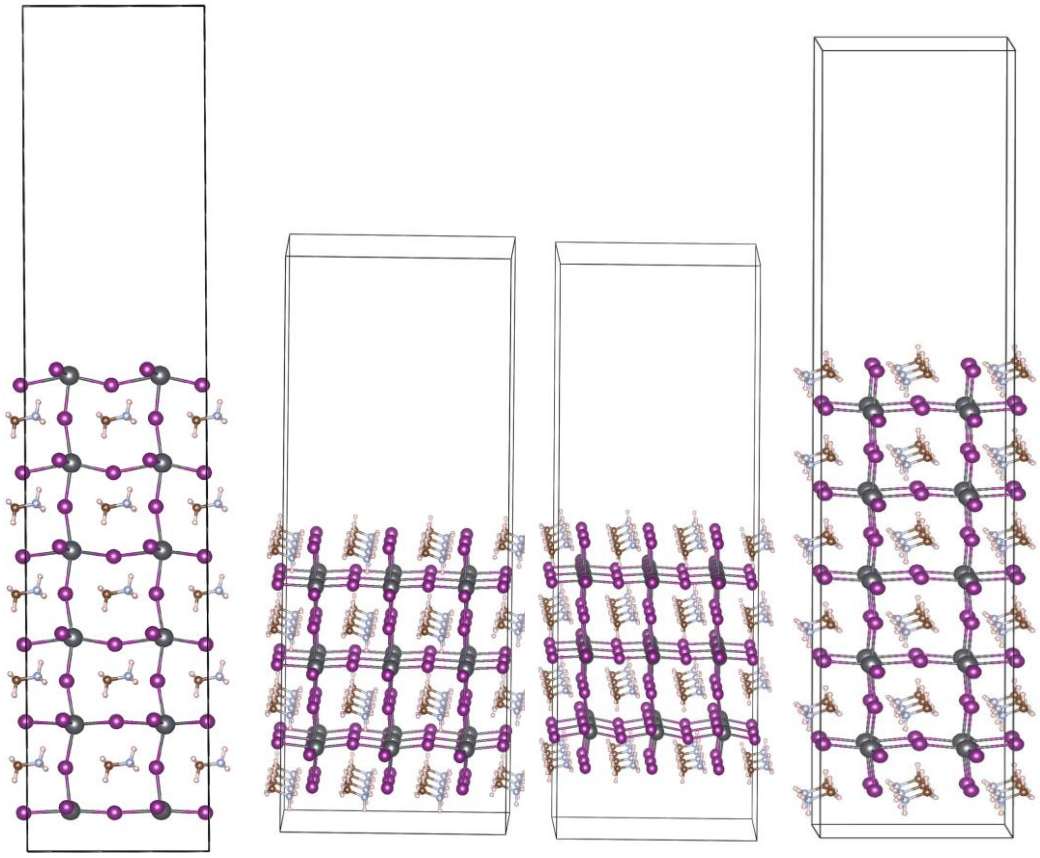

Figure 3.1: Slab models used in this work: (a) 2x2x5 PbIT slab model, (b) 3x3x3 MAIT topC slab model, (c) 3x3x3 MAIT topN slab model, and (d) 2x2x5 MAIT topC slab model.

3.2 COMPUTATIONAL DETAILS

$MAPbI_3$ is known to exhibit three stable crystal structures with temperature dependent transitions that occur as temperature is decreased - cubic to tetragonal at 330K, and tetragonal to orthorhombic at 160 K, respectively [30]. With the transformation of the crystal structure from orthorhombic (lower symmetry) to tetragonal (higher symmetry), band gap of $MAPbI_3$ decreases and hence enables greater absorption for a much longer wavelength. Transformation into a cubic structure with an increased symmetry is expected to further decrease the optical band gap, thus matching the solar spectrum better leading towards an enhanced optical absorption. Most of the $MAPbI_3$ devices reported so far use tetragonal crystal structure obtained by solution processing or vacuum deposition [31, 32]. The utilization of cubic structure of $MAPbI_3$ perovskites for the improvement of perovskite solar cells remains somewhat unexplored.

The MA cations have been shown to be dynamically disordered in the high temperature cubic phase of $MAPbI_3$ perovskites, moving in an isotropic potential at a rate approaching that of the freely rotating MA cation. However, the MA cations possess preferred orientations in the tetragonal phase which is stable at room temperature [31] . The simple cubic model has been widely employed in ab initio methods for investigating the properties of $MAPbI_3$ perovskites. We have used the simple cubic α-phase of $MAPbI_3$ in our calculations.

We consider $MAPbI_3$ slab models of the (001) surface, the most stable perovskite surface [4, 31]. Only MAI-terminated topologies are considered since MAI-terminated surfaces have been reported to be significantly more stable in the (001) direction compared to other crystallographic directions [31]. To include the orientation effects, we have considered both topC and topN models where the topC model has the $–CH_3$ groups of MA cations oriented towards vacuum in all layers while in topN model, the MA cations are oriented with their $–NH_3$ groups pointing to vacuum. All the slab models are neutral and symmetric with respect to the central Pb–I plane. All calculations are performed using DFT as implemented in Vienna Ab initio Simulation Package (VASP). The projector augmented wave (PAW) method is used to describe the ion-electron interactions. The valence configurations considered are 1s for H, *2s2p* for both C and N, *5s5p* for I, and *5d6s6p* for

Pb. The generalized gradient approximation (GGA) using Perdew-Burke-Ernzerhof (PBE) exchange-correlation functional is used to treat exchange-correlation interaction. The cut off for the plane-waves is set to 400 eV while the convergence criterion for electronic self-consistent loop used is 10^{-8} eV. The structures are relaxed with conjugate-gradient algorithm until the Hellmann-Feynman forces on atoms are smaller than 0.01 eV/ Å on the atoms that are relaxed. Most the forces that we realized are less than 0.001eV/ Å.

To simulate the (001) surface of the cubic MAPbI3, we started with the optimized bulk structure of the $MAPbI_3$ perovskite in the cubic phase. The surface was simulated using three to five layers of the perovskite along the c axis followed by a vacuum layer while keeping the periodicity of the solid in the other two directions same as in bulk $MAPbI_3$. We kept the positions of the lowest layer of the perovskite frozen at the bulk positions and allowed the atoms of the top layers to relax. The size of the vacuum layer was determined such that the spurious interaction between the surface and its periodic image along the c-axis is minimal. We find that a minimum of 25 Å thick vacuum layer is needed to minimize the interaction between the periodic slabs. For the interface with the fullerene and its PCBM analogue we considered larger supercells of size 2x2x5 and 3x3x3 of the bulk unit cell, respectively. In all simulations we maintained a minimum 25 Å of vacuum layer. We used the Monkhorst-Pack scheme for k-point integration. Since the super cells are large, we used only one k-point of the Brillouin zone for the calculations on the interface.

Two different surface terminations are considered - surface terminated with PbI (PbI-T) and terminated with MAI (MAI-T). Vacuum layers of 25 Å and 30 Å between a slab and its periodic replica for PbI- and MAI- terminated models respectively are used in the calculations to minimize the spurious interaction between periodic slabs. The interface binding energies are calculated as follows: interaction energy of the complex = sum of the energy of isolated relaxed components of the interface model – total energy of the whole interface after relaxation. Since the complexes are bound by Van der Waals interactions, DFT-D3 parameters with Becke–Johnson damping model as implemented in VASP code is used for calculating the binding energies.

3.3 RESULTS

3.3.1 MAI vs. PbI terminated surfaces

The $MAPbI_3$ has tetragonal structure at room temperature. The various surfaces of the tetragonal phase of $MAPbI_3$ has been computationally studied. On the other hand, the structure and surfaces of the other phases of the $MAPbI_3$ has not been explored as widely. Our focus here is on the cubic phase of the material which is a high temperature phase. The transition from the tetragonal phase to the cubic phase occurs at 60ºC in ambient conditions. We have optimized the (001) surface with two different terminations as mentioned above. The PbI termination leads to a smooth surface that contains only Pb and I atoms on the top. On the other hand, the MAI termination does not include any Pb atom and produces a more corrugated surface. Since the two terminations have different number of atoms, we compare the energy per atom of the two surfaces.

Another consideration is the orientation of the methyl ammonium ions in the MAIT surface. We consider two orientations of the MA ions - one in which the methyl is on top and the other one in which the ammonia is on top. We find that the two orientations of the MA ions produce a difference of 0.03 eV per atom or 6.5 eV in total energy for a 2x2x5 supercell with 26 Å of vacuum. The methyl on top orientation is more favorable compared to the ammonia on top. We cannot compare MAI-T and PbI2-T directly because of the different non-stoichiometric contents. The 2×2×5 units of MAI-T have the formula unit $C_{24}N_{24}H_{144}Pb_{20}I_{64}$ while 2×2×5 units of PbI_2-T have $C_{20}N_{20}H_{120}Pb_{24}I_{68}$. To obtain structures with similar non-stoichiometric matter, the PbI_2-T terminated surface needs 4MA while that of MAIT needs Pb_4I_4. An addition or subtraction of the missed units to the structures is necessary, and calculations done in the same environment setting are needed to achieve the two models that can be compared directly.

Since the stoichiometry of the two different termination is different, we compare the binding energy per atom for the two surfaces. We find that the PbI terminated surface has binding energy of 2.98 eV per atom whereas the MAIT surface has binding energy of 3.08 eV per atom. Moreover, the band gap of the two surfaces are also quite different with the gap of the MAIT surface being 0.56 eV larger than that of the PbIT surface. From these results we conclude that the

MAIT surface is more stable compared to the PbIT surface. We have not considered any effect of vacancies in our calculations. Claudio et. al have found that presence of vacancies in PbIT surface tends to stabilize the surface but a comparison with MAIT surface was not done [4]. Another point is that the possible rotations of the MA units are not considered. Rotation of the methyl ammonia on the surface can lead to creation of dipoles on the surface.

Table 3.1: Relative energies of MAI-terminated slab models in eVs.

Slab model	Orientation	Total energy, E_{tot} (eV)	No. of atoms, n	Binding energy per atom (eV)
2×2×5 MAIT	topC	-1184.49	276	-4.29
2×2×5 MAIT	topN	-1177.93	276	-4.26
3×3×3 MAIT	topN	-1752.47	405	-4.33
3×3×3 MAIT	topC	-1751.31	405	-4.32
2x2x5 PbIT	N/A	-1040.08	252	-4.12

3.3.2: Fullerene

When exposed to sunlight, the $MAPbI_3$ absorbs light in visible region which leads to creation of charge carriers in the material. The large diffusion length of this material is instrumental for very good efficiency of the photovoltaic cell. Typically, the active material is sandwiched between electron and hole transporting layers. The fullerenes are known to have enhanced electron affinity due to the nature of their bonding. In this work we examine the interface between a fullerene-based electron transporting layer and the perovskite surface. We have considered four different fullerene and its derivatives as the electron extracting layer – $Sc_3N@C_{80}$, $Sc_3N@C_{80}$-PCBM, C_{60}, and C_{60}-DME. We discuss the results on the interface with $Sc_3N@C_{80}$ and its

derivatives first which is followed by the results of the studies done on the interface with C_{60} and C_{60}-DME.

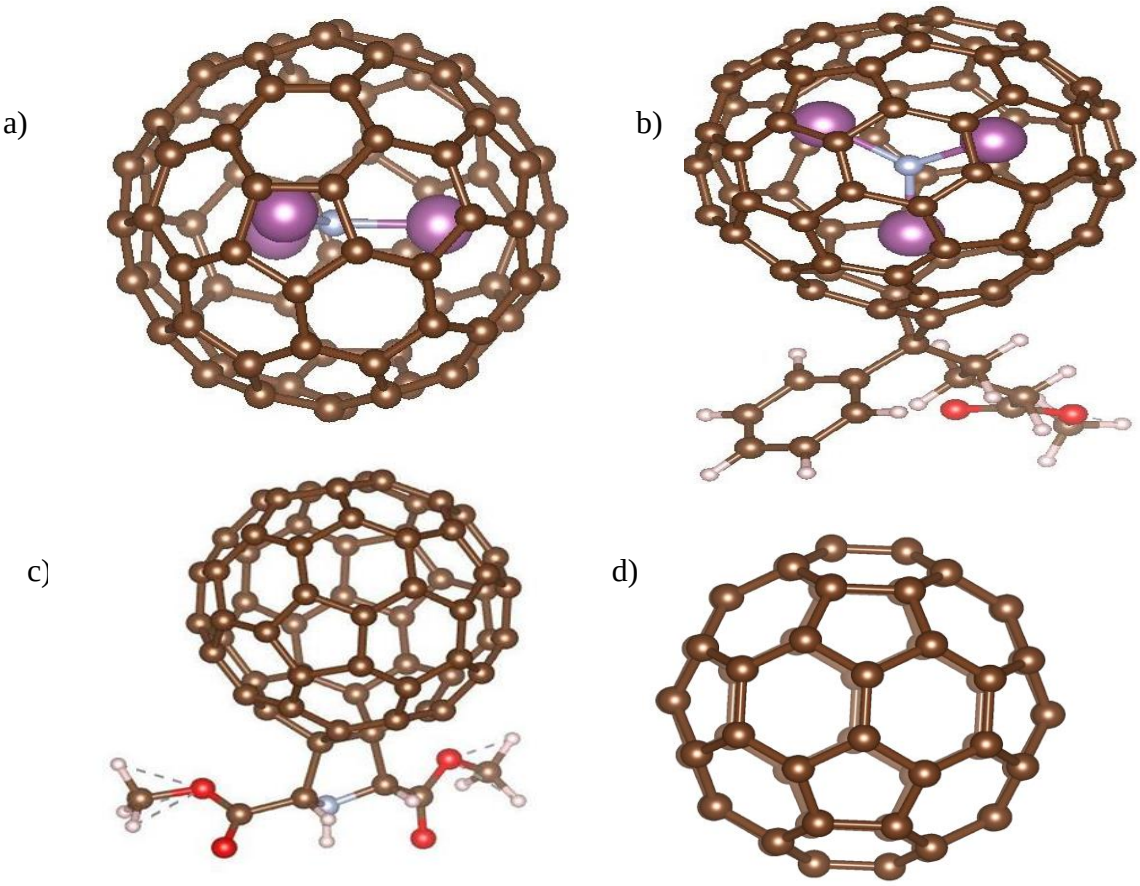

Figure 3.2: Optimized geometries of (a) $Sc_3N@C_{80}$, (b) $Sc_3N@C_{80}$PCBM, (c) C_{60}-DME, and (d) C_{60}-fullerene.

3.3.3: Interfaces of $MAPbI_3$ and metallofullerenes

We consider the $Sc_3N@C_{80}$ fullerene and its PCBM analog as the electron transporting layer. Figure 3.2(a) shows the $Sc_3N@C_{80}$ which consists of the endohedral (Sc_3N) encapsulated within a C_{80} carbon cage. Among the endohedral fullerenes which contain an endohedral unit encapsulated within a carbon cage, the $Sc_3N@C_{80}$ fullerene is the most abundant. This is noted as the third most abundant fullerene after C_{60} and C_{70}. In isolation, both the encapsulated molecule Sc_3N and the C_{80} cage are unstable. The bonding of the trimetallic nitride unit to the carbon cage is not fully understood. An idealized bonding concept is that in the encapsulated form, six electrons are transferred from the Sc_3N unit to the outer cage which makes the whole system stable. Various isomers of $Sc_3N@C_{80}$ have been identified where the structure of the outer C_{80} cage is different. The most stable among them is the one with an icosahedral outer C_{80} cage. In this study we employ an icosahedral C_{80} (Ih-C80) cage with Sc_3N units. Electrochemical measurements have established that the reduction potential of $Sc_3N@C_{80}$ (Ih) is higher than that of C_{60} which indicates higher electron accepting potential.

The endohedral Sc_3N moiety consists of Sc-C and N-Sc bonds with calculated bond lengths of 0.226 nm and 0.203 nm respectively. The carbons on the carbon cage form the pentagonal and hexagonal rings. The pentagonal C-C rings have calculated bond lengths of 0.143 – 0.145 nm while the hexagonal C-C rings are at 0.143 nm – 0.148 nm. The other group of C-C has bond lengths between 0.142 nm – 0.144 nm. The latter group of C-C bonds form the hexagonal ring that neither join the atoms that bond with Scandium atoms. The bond distances of 0.226 nm, 0.203 nm, and 0.142 nm for Sc-C, N-Sc, and C-C are comparable to the values reported in Ref [32, 33] and that of the experimental value of 0.142 nm [34, 35] for the C-C.

Shown in figure 3.2(b) is the PCBM endohedral $Sc_3N@C_{80}$. This compound is essentially the same structure in Figure 3.2 (a) plus the functional groups which consist of 6-member -C-C- ring, -C-C- straight chain coupled with -C-O-C-, -C=O, and -C-H. This molecule can be classified as a Trimetallic nitride templated (TNT) endohedral metallofullerenes [36] which, in this case, is

distinguished by Sc_3. For the 6-member ring, the -C-C- and -C=C- have an equal magnitude of about 1.4 Å. The -C-C- bonds connecting 6-member ring and the straight chain functionals (butyric acid methyl esters) to the edge carbon atom connected to the C_{80} carbon cage are 1.52 Å and 1.51 Å. The C-C bond length value of 1.51 Å is the same as the one in 1, 1, 1-Tribromoethane [37].

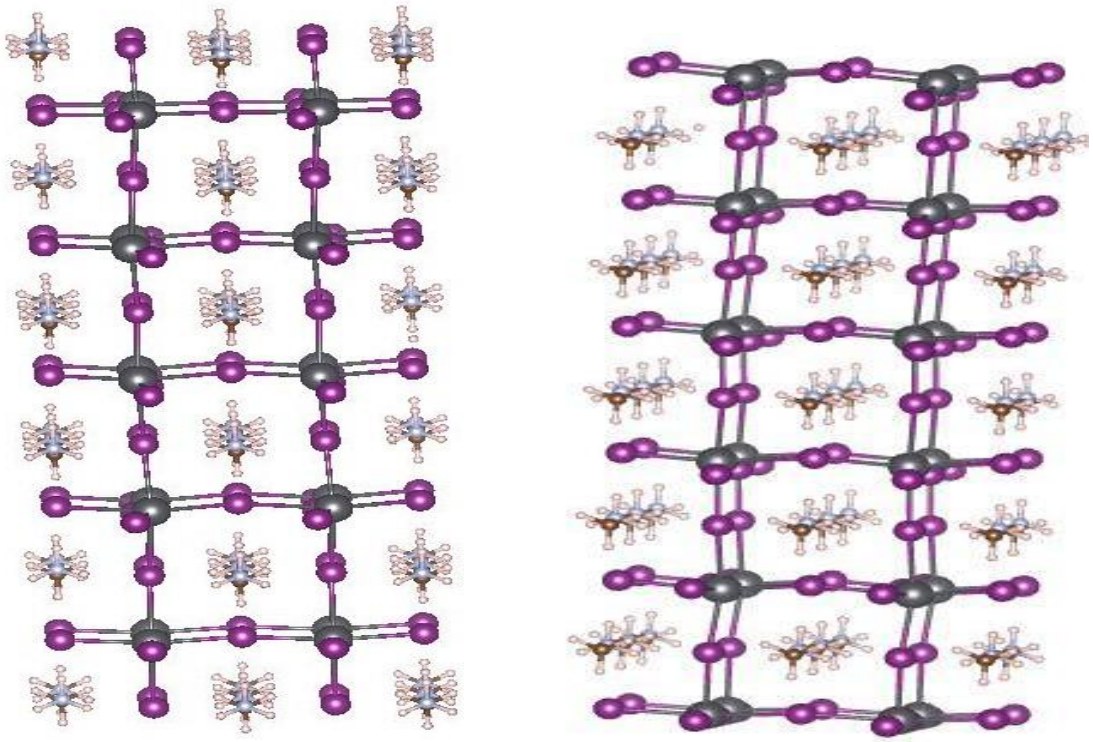

Figure 3.3: Optimized geometries of MAIT and PbI_2 T perovskite for a (001) slab of 2x2 periodicity for 5 layers (from left to right).

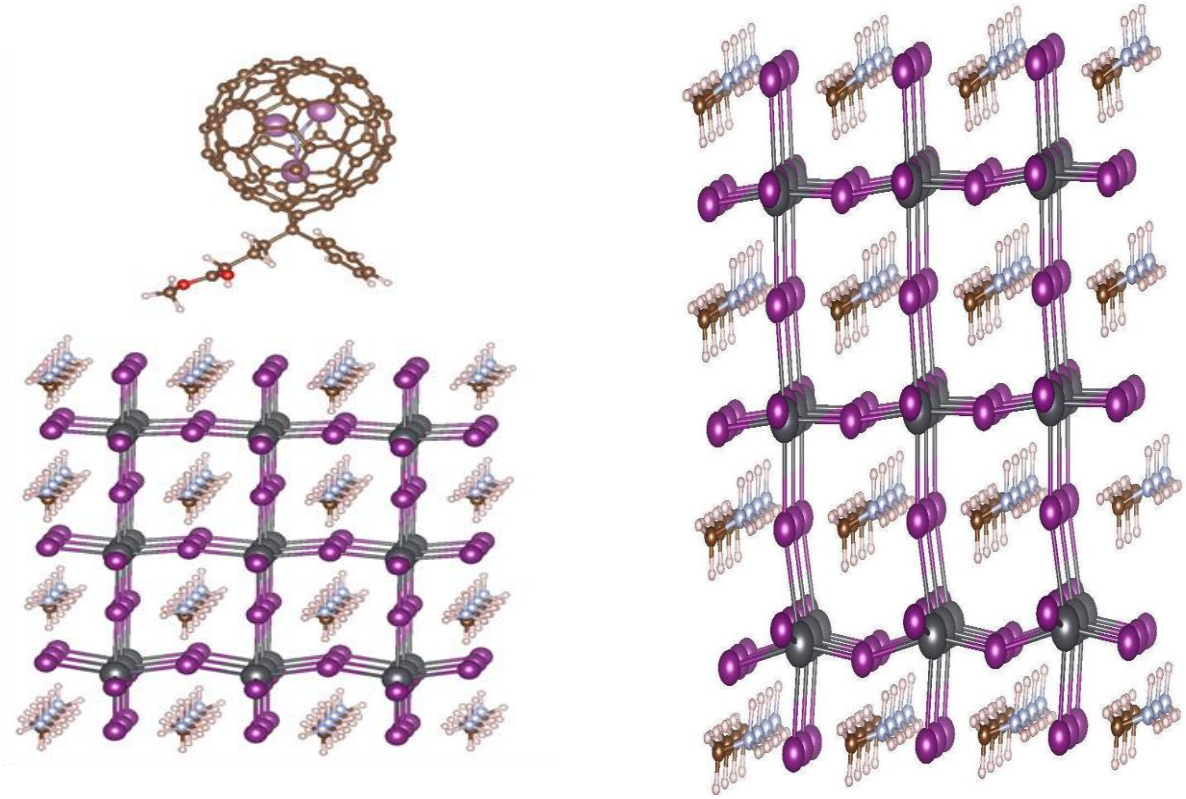

Figure 3.4 MAIT for a (001) slab of 3x3x3 unit perovskites interfaced with a PCBM fullerene (left) and its corresponding surface (right). The top surface of the MAIT surface consist of the NH_3 (topN) with the H pointing up. The Sc3N@C_{80}PCBM fullerene consist the Sc_3N endohedral element.

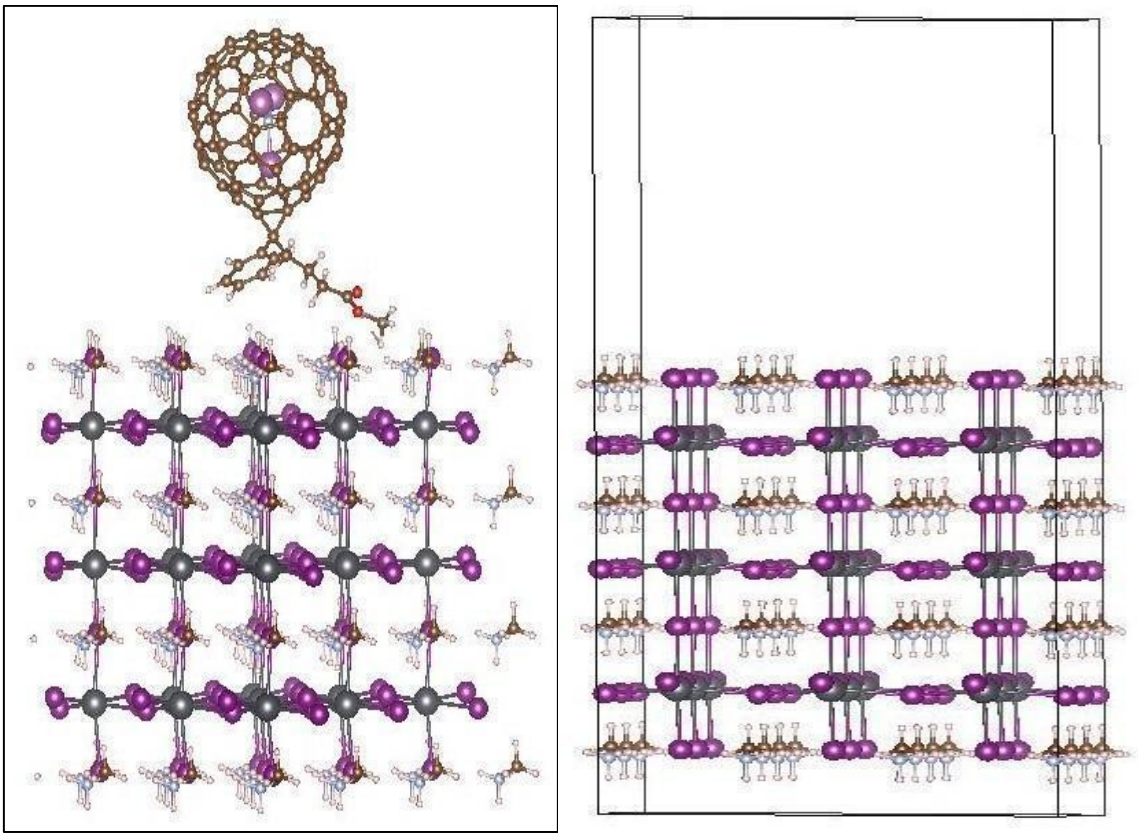

Figure 3.5: MAIT for a (001) slab of 3x3x3 unit perovskites interfaced with a PCBM fullerene(left) and its corresponding surface (right). The top surface of the MAIT surface consist of the CH_3 with the H pointing up. The $Sc_3N@C_{80}$ - PCBM fullerene contains the Sc_3N endohedral element.

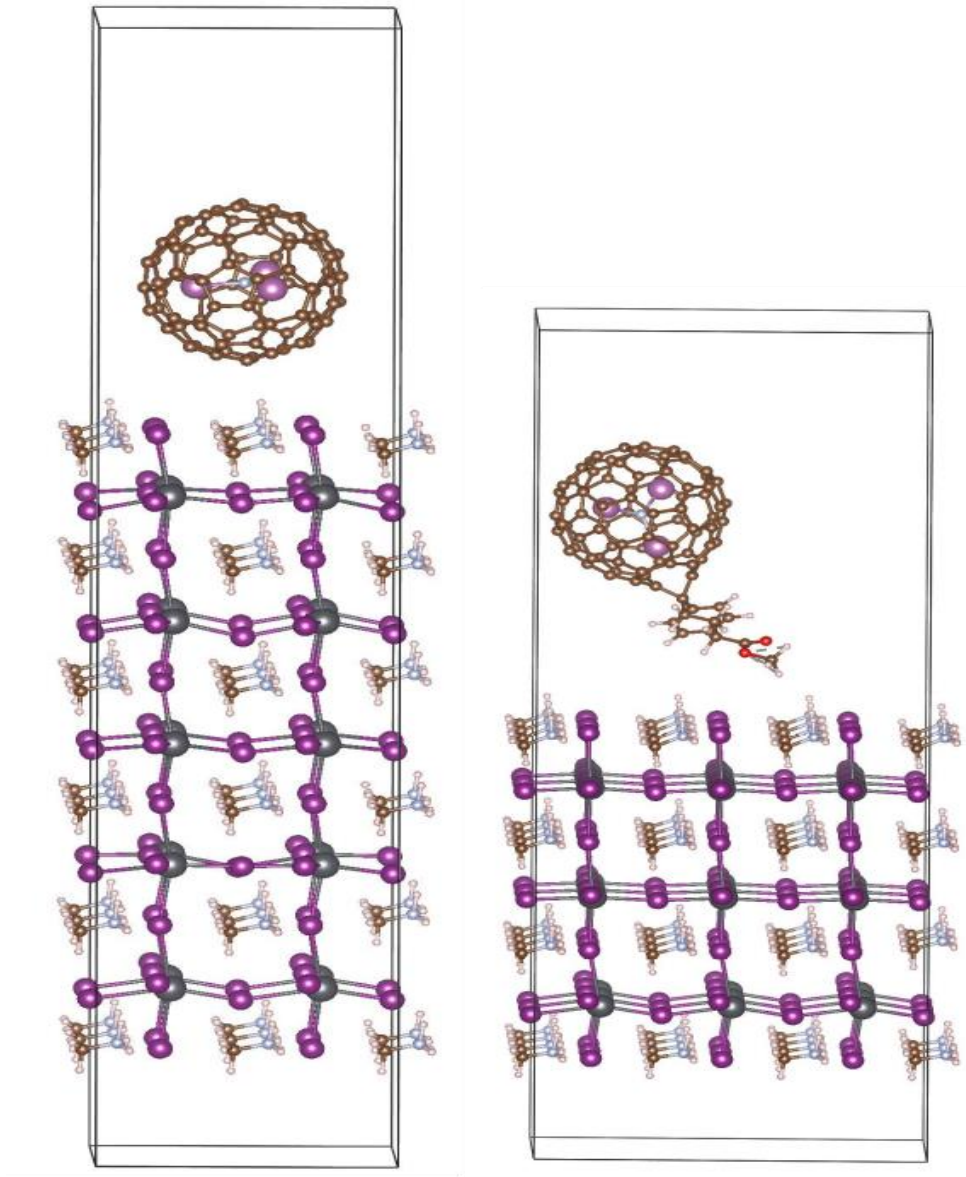

Figure 3.6: The optimized geometries of fullerene/perovskite interfaces: (a) interface of 2x2x5 MAIT topN slab model with $Sc_3N@C_{80}$ and (b) interface of 3x3x3 MAIT topN slab model with $Sc3N@C_{80}$-PCBM.

3.3.4 Binding of metallofullerenes on $MAPbI_3$ surface

Figures 3.4 – 3.6 shows the interfaces studied here. Figure 3.6 (a) shows the optimized geometry of fullerene-perovskite interface which consists of MAI-T surface interfaced with $Sc_3N@C_{80}$. Since the C_{80} cage is formed by pentagonal and hexagonal carbon rings, we consider two orientations of the fullerene - with pentagonal ring facing the perovskite and one with hexagonal ring facing the perovskite. For the MAIT perovskite surface also we consider two orientations of the methyl ammonium - the one with methyl groups exposed (C-top) and the other with ammonium groups exposed (N-top). For these calculations a 2x2x5 supercell of the perovskite is considered with the fullerene on top. The binding energies of the interface is calculated as

B.E.= E(total) - E(fullerene) - E(surface).

The calculated binding energies of the interface with C-top and N-top surface is presented in Table 3.2. Our DFT calculations indicate that at the PBE level, the highest calculated binding energy is 1.05 eV for an N-top surface. Since the van der Waals interaction is important for these systems, we have also included DFT-D3 calculation of the binding of the surface and the fullerene. Inclusion of DFT-D3 parameters for van der Waals interaction increases the binding energy to 1.22 eV. The shortest distance of 2.88 Å is observed between a C of C_{80} and H from NH_3 of the MAIT surface. Similar binding energy of 1eV is also reported in Ref [33].

In case of $Sc_3N@C_{80}$-PCBM, the binding energies at the DFT level are negative for the topN surface which indicates that at DFT-only level the fullerene layer does not bind to the perovskite surface. Inclusion of the van der Waals interaction however changes the results with a binding energy of 0.11 eV per fullerene. In the case of the PCBM the top C orientation is significantly more favored than the top N orientation. Our calculations show that the binding of the fullerene is 0.5 eV higher than the PCBM. The reason could be that the carbon cage is more easily polarized by the surface dipoles than the PCBM. The carbon cage is further away from the surface when a PCBM is deposited on the surface and the interaction between the fullerene and the surface is reduced. For the fullerene deposited interface the shortest distance between the

carbon of the cage and the NH_3 from the $MAPbI_3$ is 2.88 Å whereas the shortest distance between the methyls of PCBM and the surface is 2.41 Å which shows that the carbon cage is further away from the surface in the latter case.

Table 3.2: Interface binding energies (eV) and shortest interaction distances (Å) for the perovskite/fullerene interfaces studied. The interactions corresponding to the shortest interfacial interaction distances are given in parentheses.

Interface	Model	Shortest interaction distance (Å)	PBE Binding Energy (eV)	PBE-D3 Binding Energy (eV)
2×2×5 MAIT/ $Sc_3N@C_{80}$ -Pent	topN	3.41 (C...H)	0.26	0.38
2×2×5 MAIT/ $Sc_3N@C_{80}$ -Hex	topN	2.88 (C...H)	1.05	1.22
3×3×3MAIT/$Sc_3N@C_{80}$-PCBM	topN	2.99 (H...H)	-0.038	0.113
3×3×3MAIT/$Sc_3N@C_{80}$-PCBM	topC	2.41 (H...H)	0.042	0.692

3.3.5 Electronic Properties

The PBE band structure of cubic bulk $MAPbI_3$ along the high symmetry k-path is shown in Figure 3.7 where the Fermi level have been translated to 0.0 eV. This structure has a direct bandgap of 1.61 eV at R point which agrees with the available experimental values [38, 39]. The site projected density of states is shown in Figure 3.8, which shows that the states that dominate the conduction band minimum (CBM) and valence band maximum (VBM) mainly arise from the PbI_3. The CBM and VBM occur at the same reciprocal point, which makes $MAPbI_3$ a direct band gap material. The orbital projected density of states (DOS) clearly show that the CBM is mostly dominated by Pb-p orbitals, and the VBM is contributed mostly by the p orbitals of the I-p [40]. The optimized lattice parameters are calculated to be 6.36 Å, which is comparable to the experimental value of 6.328 Å [41].

DOS plot for $MAPbI_3$ surface with MAIT surface exposed in 001 direction for three and five layers is shown in Figure 3.9. The band gap in MAI-T surfaces decreases as their thickness increases. The 3x3x3 surface with three layers has a band gap of 2.24 eV while that with five layers (2x2x5) has a band gap of 1.68 eV. As the layers of the surface increases the gap will move towards the bulk band gap value. The size of the unit cells used in this calculation is 6.36 Å x 6.36 Å x 50 Å and 6.36 Å x 6.36 Å x 61 Å for three and five layers in the respective order. This trend is consistent with the findings reported by Geng et. al. [5] where they determined the band gap of MAI-T to approach that of the bulk as thickness of the material increases. With increased surface area, the same trend is observed. We computed three and five layers but with their surface area increased to 19.02 Åx19.02 Å and 12.72 Åx12.72 Å (DOS shown in Figure 3.14) and obtained bandgaps of 2.38 eV and 1.45 eV. The band gap of MAI-T surface tends to converge to a single value as the number of layers increases.

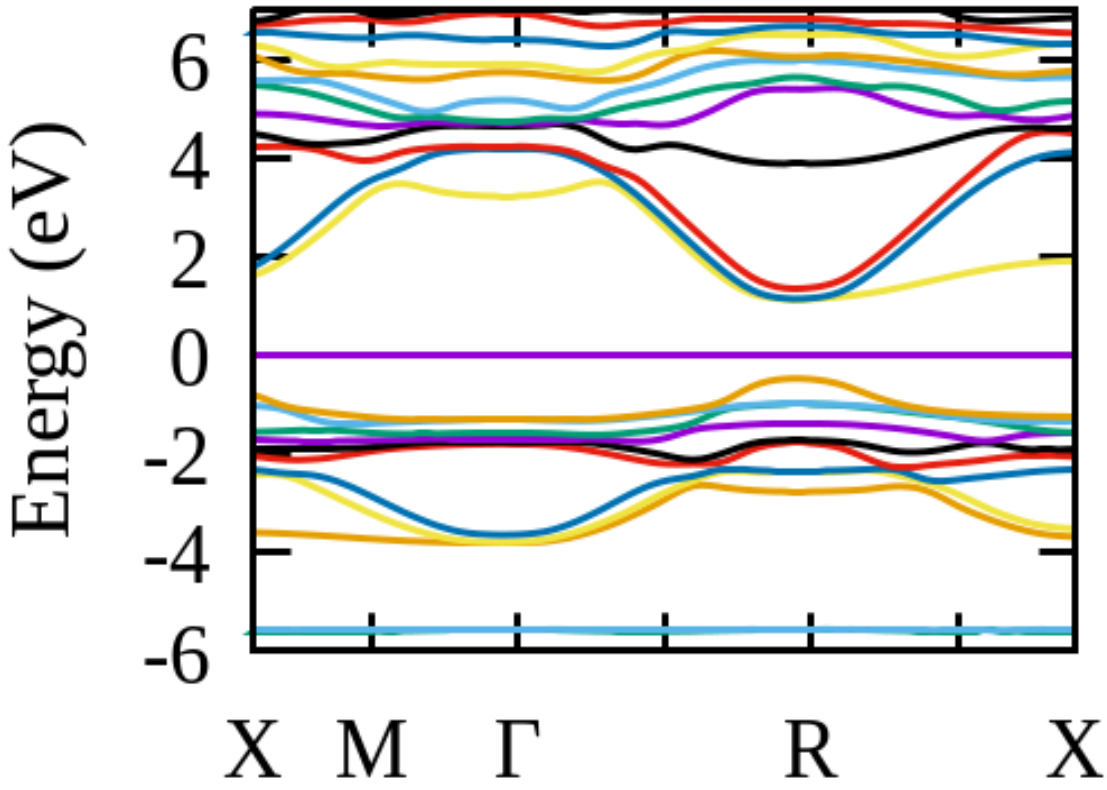

Figure 3.7: Band structure plot for $MAPbI_3$ bulk system. The lattice parameter utilized was 6.36 Å.

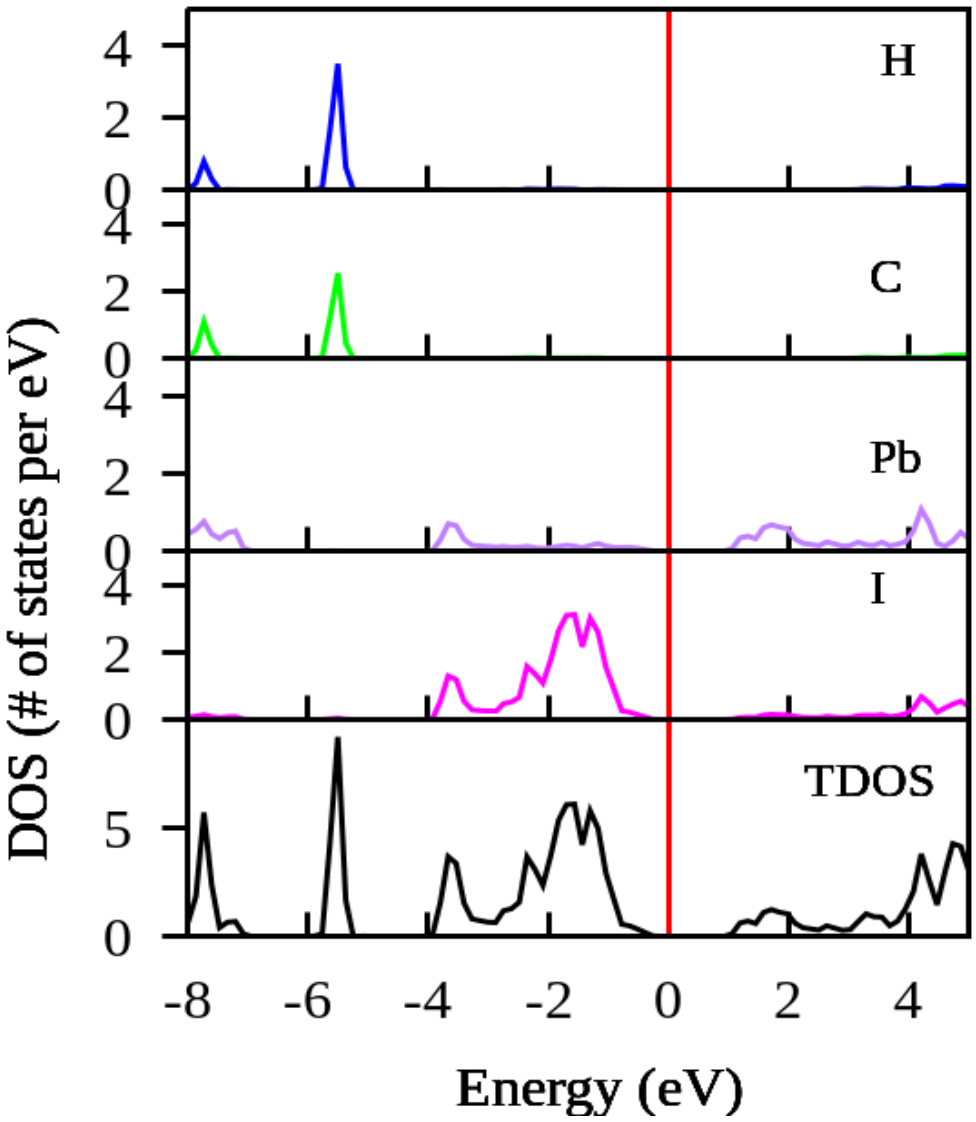

Figure 3.8: Projected density of states and total density of states (TDOS) for the $MAPbI_3$ bulk cubic structure.

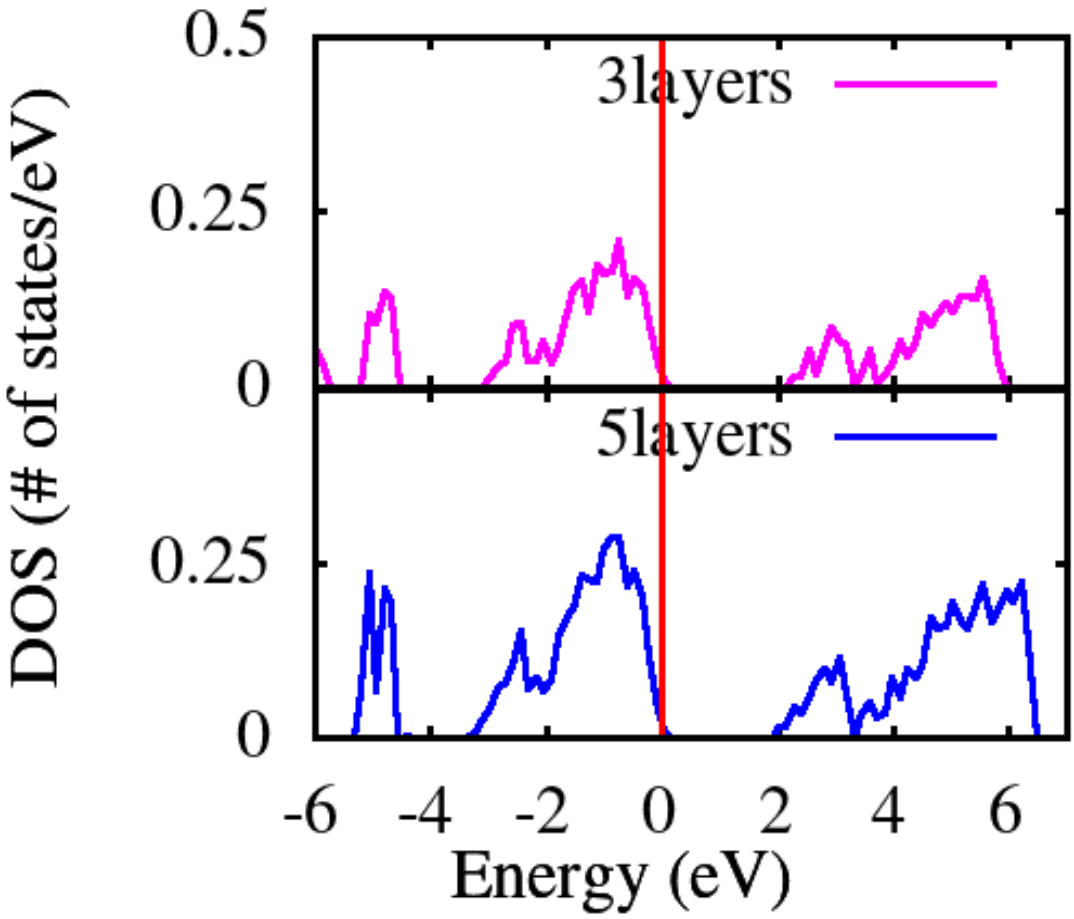

Figure 3.9: DOS plot for $MAPbI_3$ surface with methyl ammonium ions terminated (MAIT) surface exposed in 001 direction for three and five layers. These surfaces are free standing (isolated).

The results of 2×2×5 MAI-T surface interfaced with endohedral tri-scandium nitride at C_{80} (225MAI-T/Sc3N@C_{80}) are reported in Figures 3.10-12. The dimension of the surface is a = 12.72 Å x b = 12.72 Å. In Fig. 3.10, we show the plot of the partial DOS of 225MAI-T/Sc3N@C_{80} complex divided in three panels along the y-axis with a common x-axis. The top layer is methyl ammonium lead iodide surface with methyl ammonium Iodide termination ($MAPbI_3$ with MAI-T). The middle panel shows the fullerene DOS, and the total densities within the complex (TDOS) at the bottom. $MAPbI_3$ surface within the complex has a narrow band gap of 1.175 eV. The p-orbitals dominate at the VBM up to a width of about 11 eV below the Fermi level with its highest

peak approaching 60 states/eV. The s-orbitals are predominant at lower energy levels. The sp-hybridized characteristic is more pronounced between -5 eV and -9 eV as seen in the partial DOS plot (Fig. 3.10). The p-orbitals also dominate the conduction bands where the large contribution is from the substrate. The middle layer represents the contributions from $Sc_3N@C_{80,}$ where p-orbitals contributed more at VBM while p- and d-orbitals dominate at the CBM leaving the HOMO-LUMO gap of 0.24eV. Similar behavior is observed with the total density of states which is the sum of pDOS from the surface and fullerene.

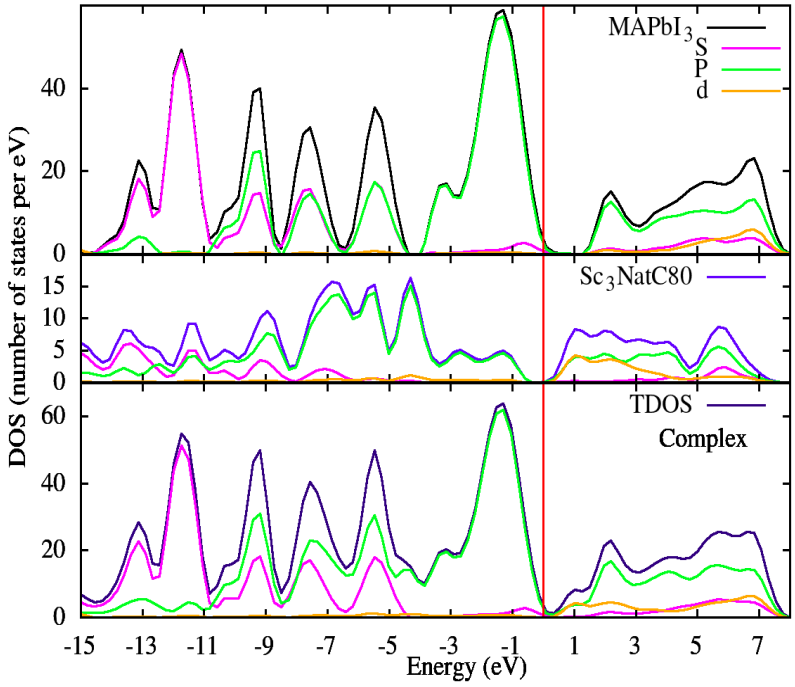

Figure 3.10: Partial density of states (pDOS) of Sc3N@C80 binding on the $MAPbI_3$ surface. The three pDOS plots are presented: (top) $MAPbI_3$, (middle) fullerene, and (bottom) the complex.

To better understand the partial density of states of the fullerene layer within the complex (Fig. 3.10, middle graph) we plotted the density of states site-projected onto the carbons of the cage and on the endohedral (Sc_3N) unit as shown in Fig. 3.11. It's clear from this diagram that p-

orbitals from the fullerene cage (carbon) also dominate the top of the valence band and the bottom of the conduction band, while d-orbitals from Sc contribute the bottom of the conduction band.

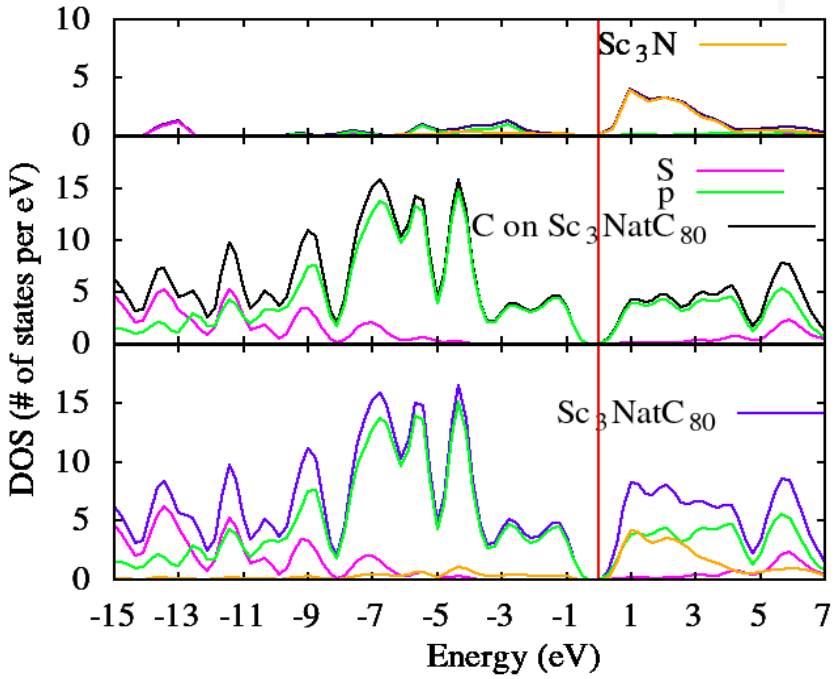

Figure 3.11: Partial density of states for tri-Scandium nitride, fullerene cage, and $Sc_3N@C_{80}$ while interfaced with $MAPbI_3$ within the complex.

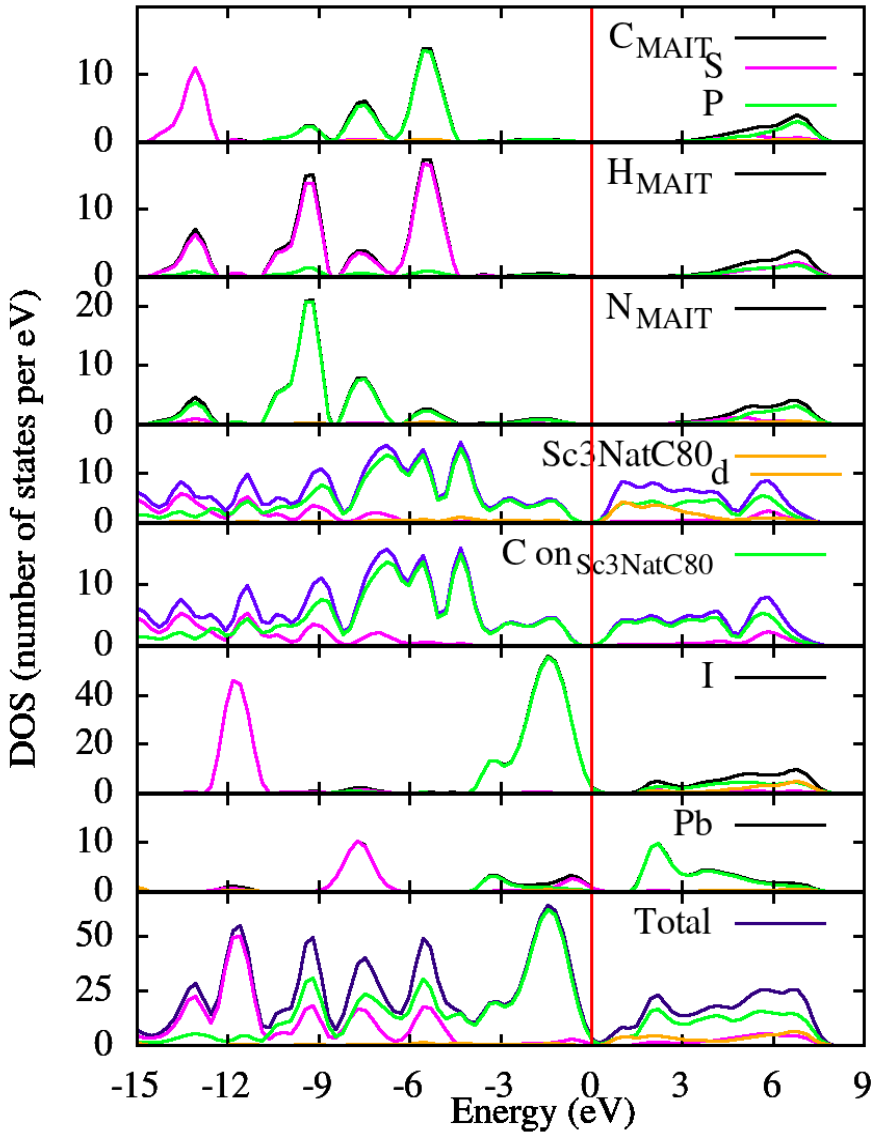

Figure 3.12: Projected DOS and pDOS of $MAPbI_3/Sc_3N@C_{80}$. $Sc_3N@C_{80}$ is the fullerene.

For the interest of understanding the overall behavior of this complex entirety, we plot projected elemental density of states in Figure 3.12. This plot shows that the states near the Fermi level, which determines the characteristics of the material are the Pb and I valence orbitals with very little contribution from the organic molecules.

We investigated the DOS of the free-standing fullerene where a fullerene is not interfaced with perovskite (Figure 3.13). It shows a band gap of 1.35 eV, which is a contrast to the fullerene in the complex in Fig. 3.11 whose band gap is 0.24 eV. The perovskite destabilizes the LUMO of the fullerene which shifts p-orbitals by -1.11eV. This value is comparable to the downshift of 0.69 eV [33] at Graphene-C_{60} interface.

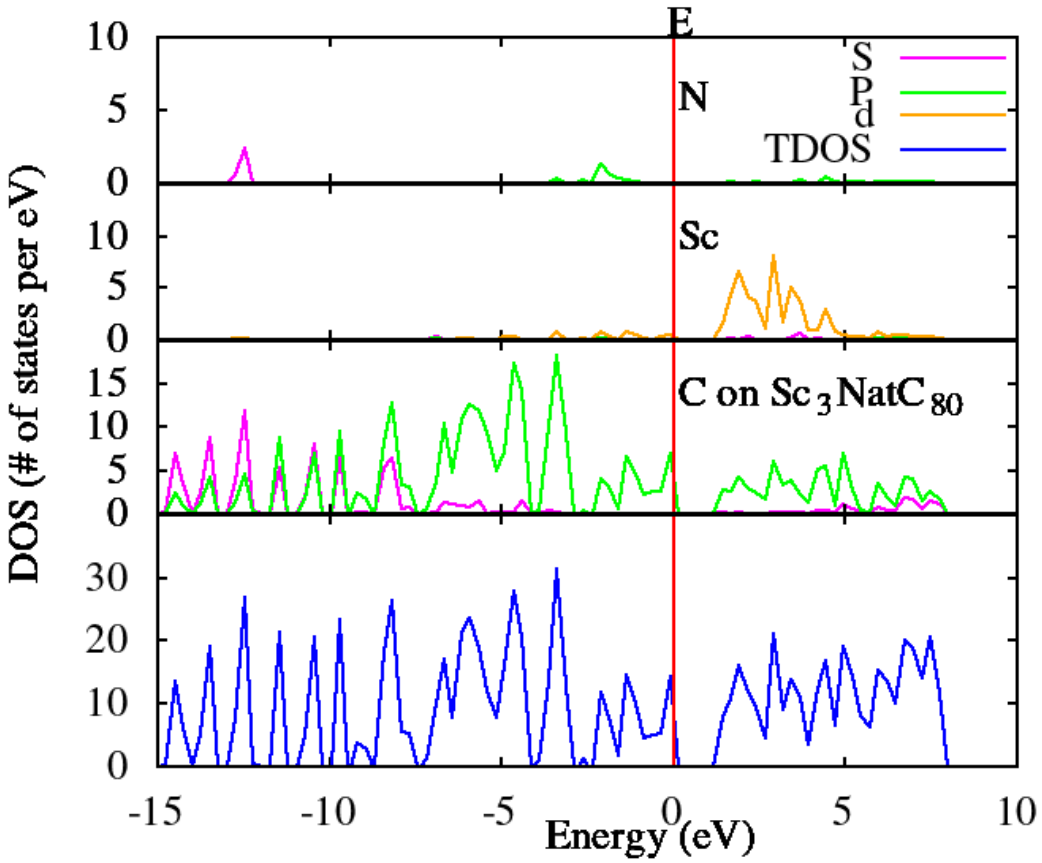

Figure 3.13: The representation of $Sc_3N@C_{80}$ when not interfaced with $MAPbI_3$. The Joint density of states of Scandium, nitrogen, carbon, and total density of states of the isolated endohedral fullerene are shown.

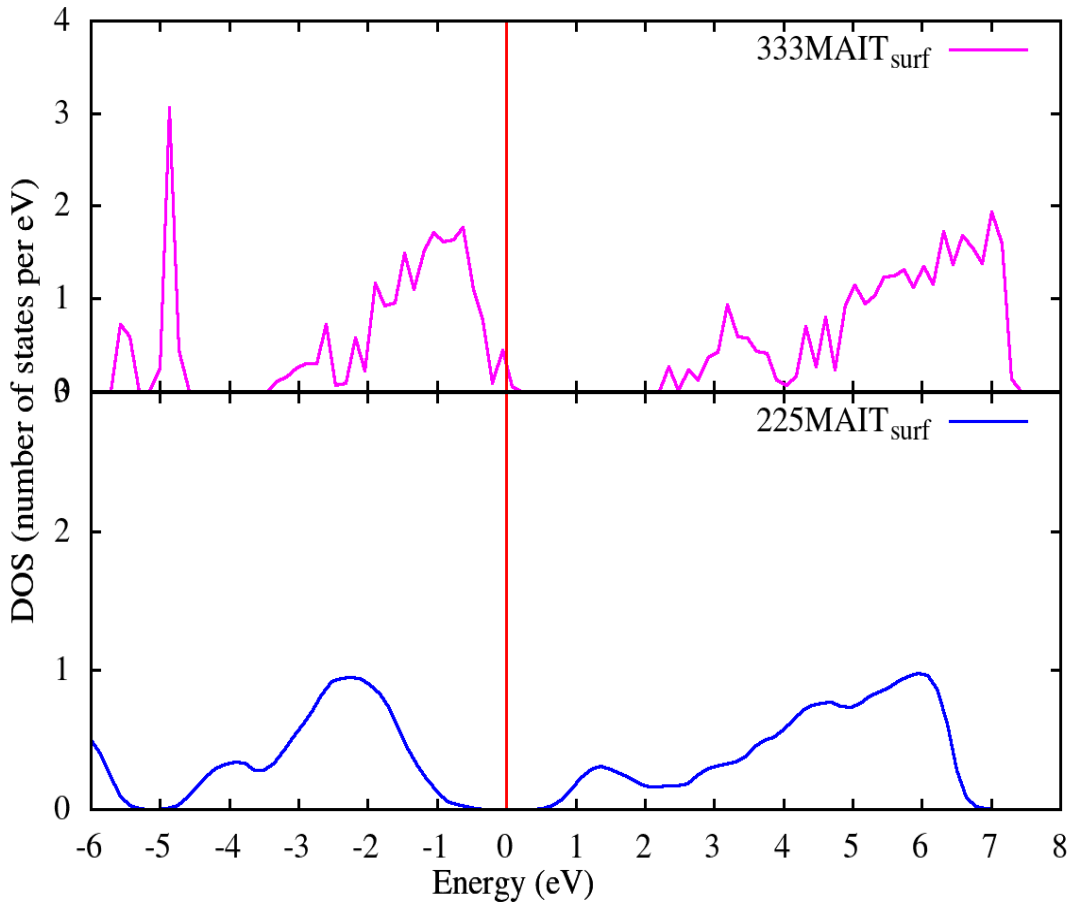

Figure 3.14: DOS plot for $MAPbI_3$ surface with methyl ammonium ions terminated (MAIT) surface exposed in 001 direction for three and five layers. The surfaces contain 3 x 3 and 2 x 2-unit cells of about 6.36 Å for each cell. These surfaces are free-standing (not interfaced with electron extracting layer).

The free-standing $MAPbI_3$ surfaces (whose DOS are shown in Figs. 3.9 and 3.14) have larger band gaps compared to the surfaces within the complexes. The smaller gap of the complexes arises due to the interaction of the surface with the fullerene layer. The most important aspect of the complex electronic structure is that the fullerene virtual states form the bottom of the conduction band which shows that the fullerene layer can work as an electron transporting layer.

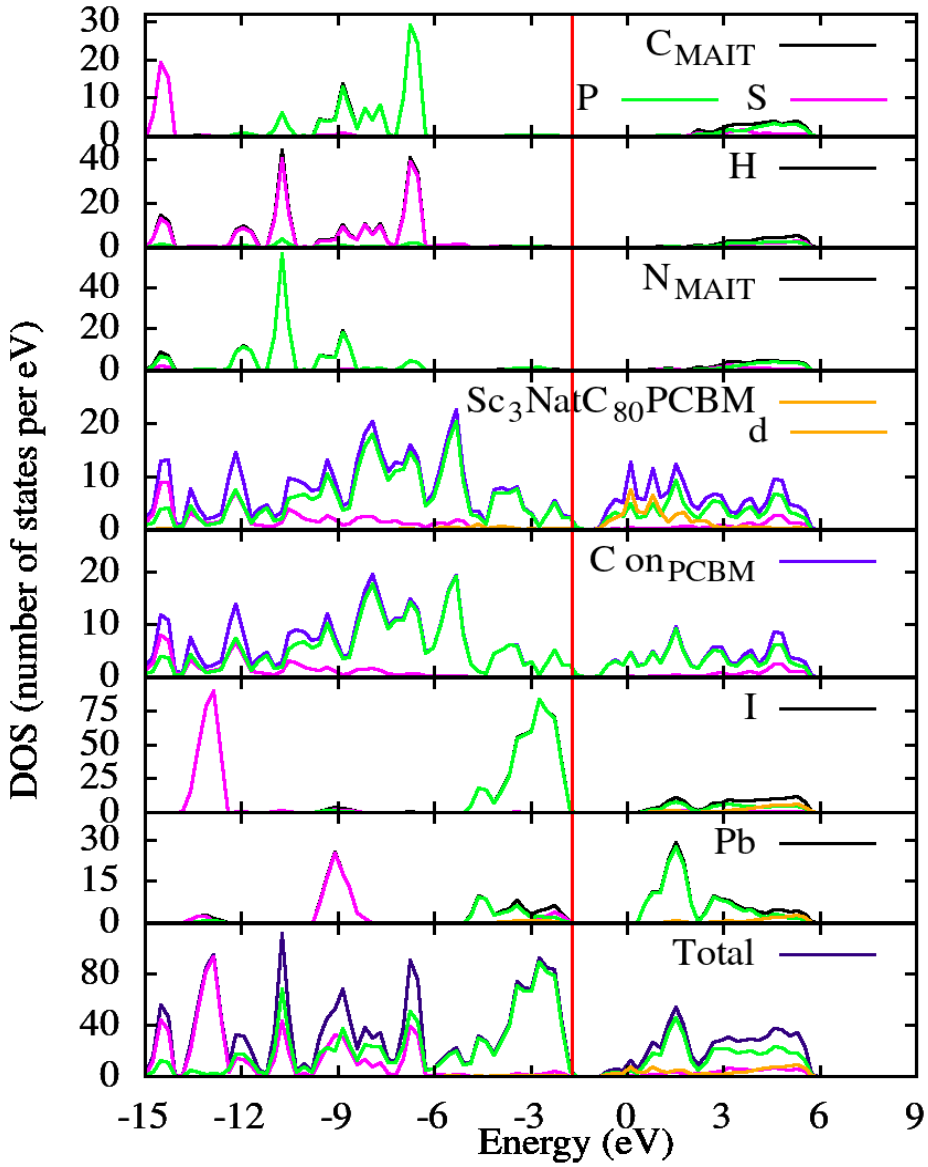

Figure 3.15: Projected density of states of the complex of 333MAIT/$Sc_3N@C_{80}$PCBM. The bottom graph consists of the total contribution of the complex.

Similar analysis is presented below for the $Sc_3N@C_{80}$PCBM-$MAPbI_3$ interface. The density of states of this complex is shown in Fig. 3.15-3.16. Due to the larger extent of the PCBM, we have used a laterally larger supercell made of 3x3x3 unit cells. Similar to the fullerene-

perovskite interface, the bottom of the conduction band has a large contribution from the PCBM layer. The reduced number of perovskite layer results in a larger band gap. In the case of PCBM-perovskite interface too, the PCBM virtual states lie lower than those of the surface resulting in a lower band gap. The largely contributing VB at the Fermi level comes from the I-p, followed by Pb-s and C-p respectively. Similar to the interface with the Sc_3N@C80, the overall band gap of the interface is lowered to 0.55 eV. The standalone $Sc_3N@C_{80}$PCBM has a bandgap of 0.61 eV compared to the 0.55 eV gap with the complex.

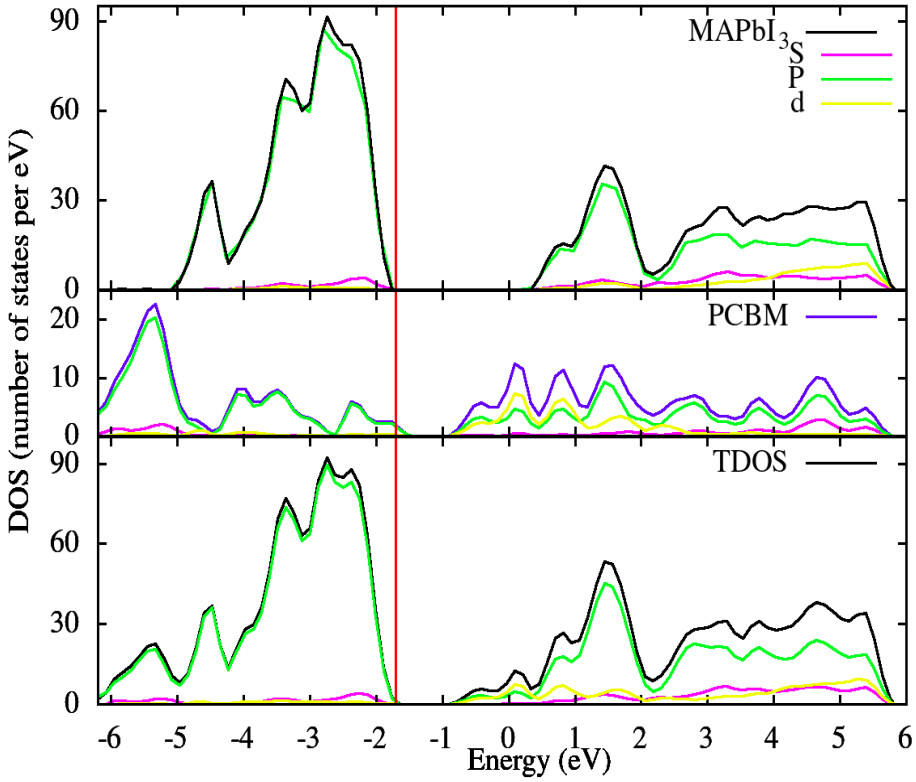

Figure 3.16: Partial density of states for 3x3x3MAIT, PCBM, and complex.

3.3.6: Local Potential and Charge density difference

Table 3.3: Vacuum Potential, Fermi level energy, and work function of complex structures, their corresponding surfaces, and $Sc_3N@C_{80}$ and $Sc_3N@C_{80}$-PCBM

	Vacuum Potential, E_{vac} (eV)	Fermi level E_{fermi} (eV)	Work function W (eV)
2x2x5MAIT	4.03	-0.36	4.40
$Sc_3N@C_{80}$	3.75	-1.50	5.25
2x2x5MAIT/$Sc_3N@C_{80}$-Pent	4.10	-0.08	4.19
3x3x3 MAIT	3.30	-1.78	5.08
$Sc_3N@C_{80}$-PCBM	1.21	-3.52	4.73
3x3x3 MAIT/ $Sc_3N@C_{80}$-PCBM	2.88	-1.54	4.41

Work function values are shown in Table 3.3. These values are calculated by subtracting Fermi level energy from vacuum potential E^{vac}. The work function of $Sc_3N@C_{80}$ is higher than 2×2×5 MAIT surface. Depending on the number of perovskite layers, the calculated work function of the MAIT surface ranges from 4.4 - 5.1 eV. The alignment of work function at the junction implies charge transfer at the interface. The flow and distribution of charge is expected to continue until the surface and the fullerene attains the same Fermi level. When their Fermi level get aligned, the system attains its electronic equilibrium state. The charge transfer is occurring in Fig. 3:18 at the interface region as evidenced their work function. The fullerene can easily extract electrons from the perovskite surface.

The work function of the complex (2×2×5 MAIT/ $Sc_3N@C_{80}$ -Pent) is lower by 0.21 eV and 1.06 eV than its corresponding isolated perovskite and fullerene, respectively. Similarly, its Fermi level is shifted by +1.146 eV and +1.423 eV compared to the isolated perovskite and fullerene. Similar lowering is also seen in case of the PCBM.

The above results confirm that significant changes in the electronic structure of the perovskite and the fullerene layer occurs due to the adsorption of the fullerene/PCBM on the perovskite surface. Our calculations show that the van der Waals interaction plays a significant role in the formation of the interface. Photoabsorption in the perovskite leads to generation of free carriers. Our calculations show that the virtual orbitals of the fullerene/PCBM layer lie below the perovskite unoccupied states. As a result, the excited or free electrons can easily move from the conduction band of the perovskite to the conduction band of the fullerene layer. Thus, the fullerene/PCBM can effectively serve as electron conductor at the interface.

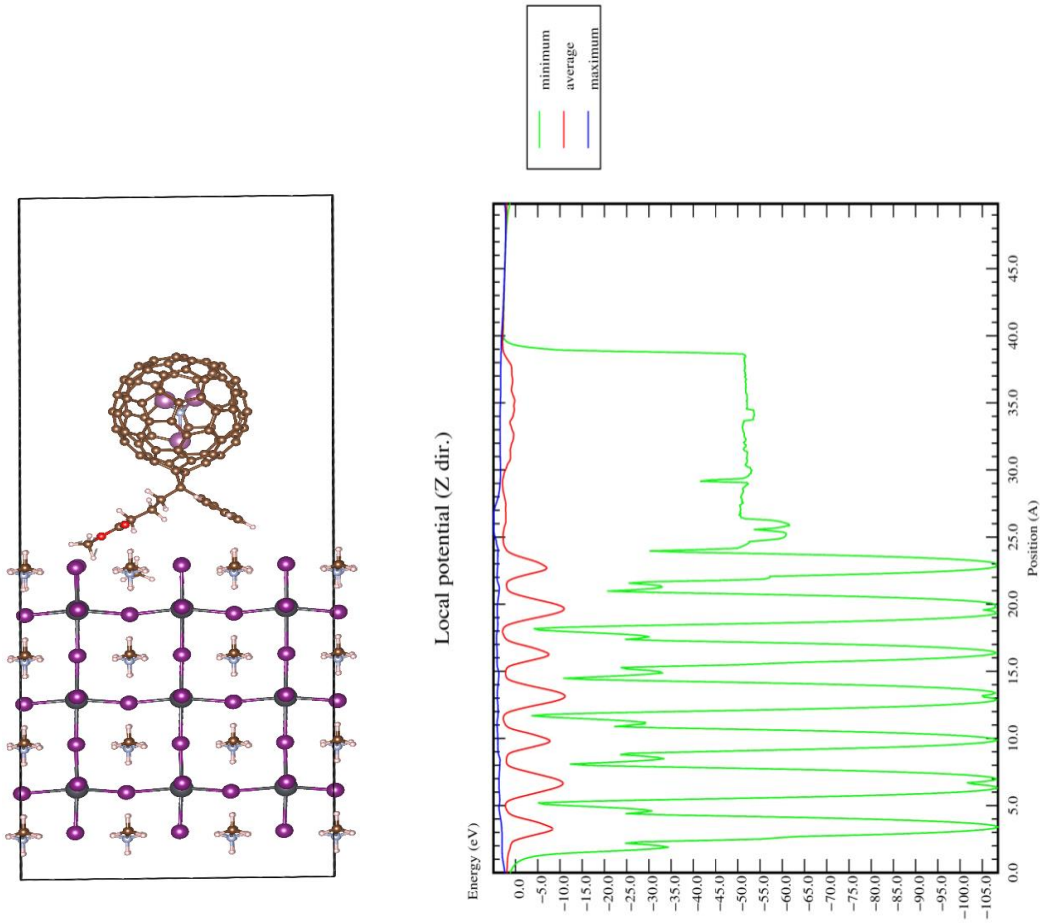

Figure 3.17: Local Potential of perovskite interface with $Sc_3N@C_{80}$-PCBM (3x3x3MAIT-$Sc_3N@C_{80}$-PCBM) in the Z-direction. Legend: the average vacuum potential (red), the maximum potential (blue), and the minimum potential (green).

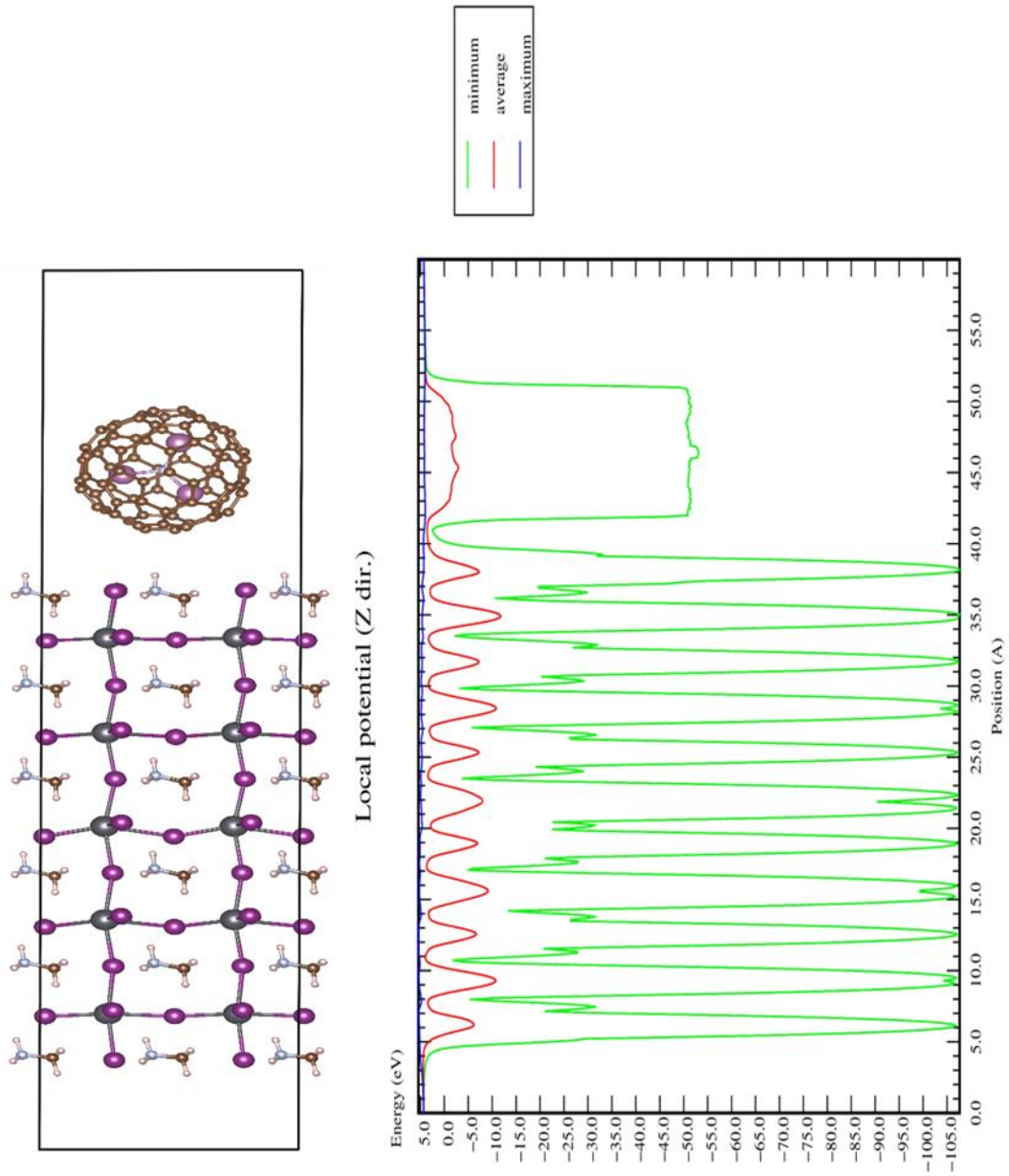

Figure 3.18: Local Potential of perovskite interface with $Sc_3N@C_{80}$ (3x3x3 MAIT-$Sc_3N@C_{80}$) in the Z-direction. Legend: the average vacuum potential (red), the maximum potential (blue), and the minimum potential (green).

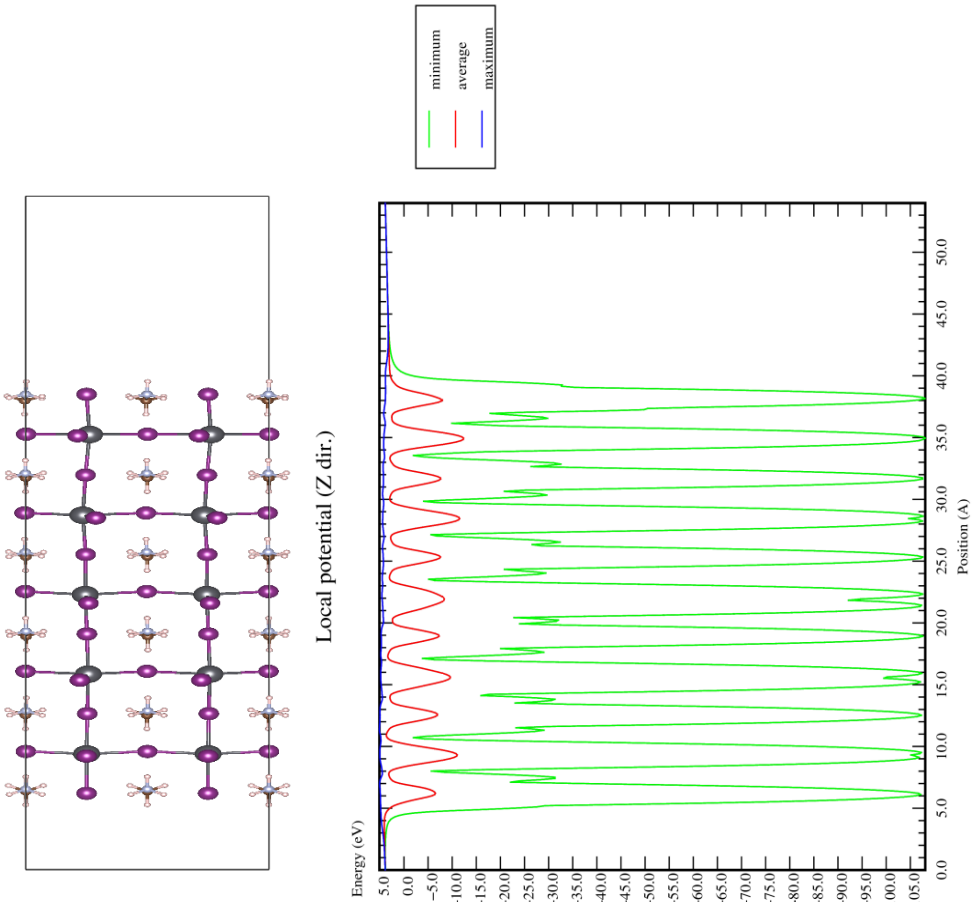

Figure 3.19: Local Potential of perovskite surface (2.2.5MAIT-Ntop) in the Z-direction. Legend: the average vacuum potential (red), the maximum potential (blue), and the minimum potential (green).

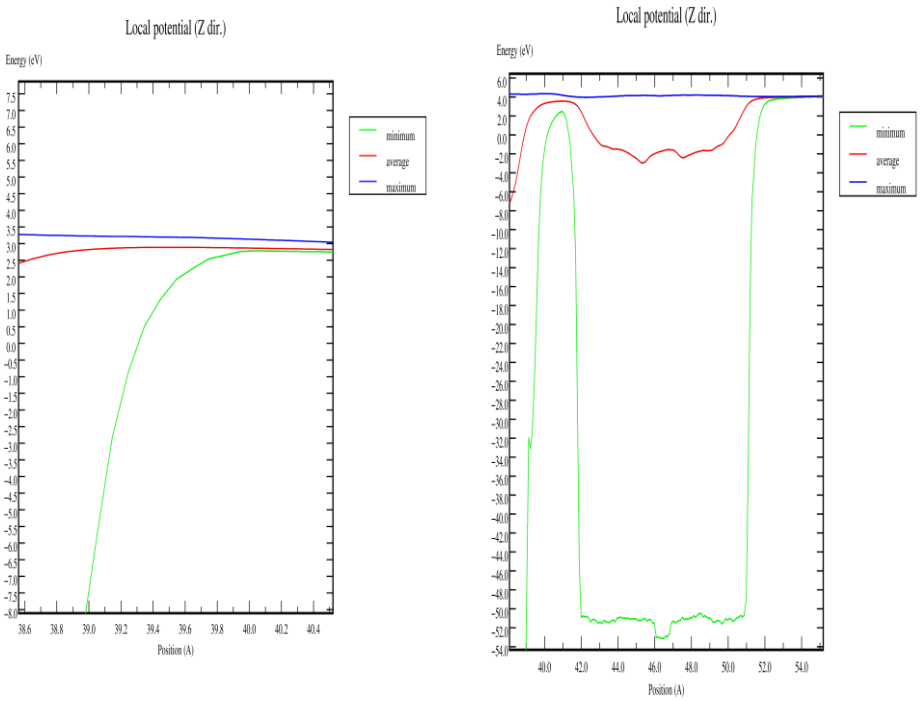

Figure 3.20: Local Potential of $Sc_3N@C_{80}$-PCBM and $Sc_3N@C_{80}$ in the Z-direction zoomed to show the average vacuum potential. Legend: the average vacuum potential (red), the maximum potential (blue), and the minimum potential (green).

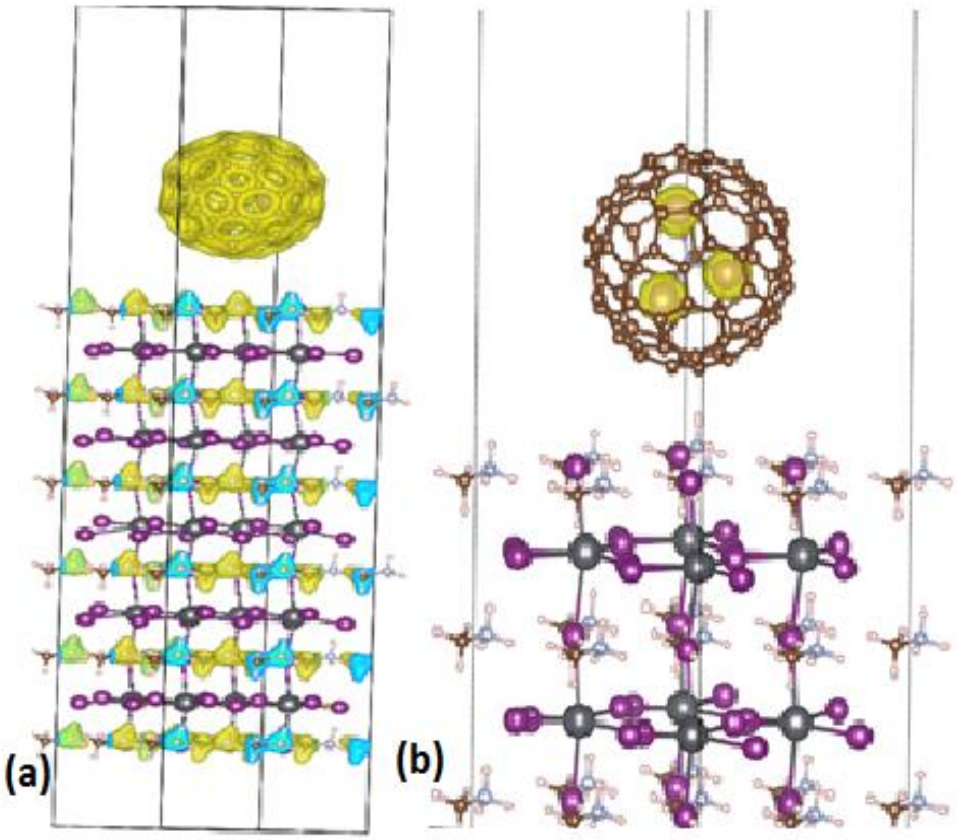

Figure 3.21: Charge density plot for (a) 2x2x5 MAIT/$Sc_3N@C_{80}$ before and (b) subtracting the charge densities of the isolated substrate and the fullerene. Only two layers of the substrate adjacent to the interface are shown in (b).

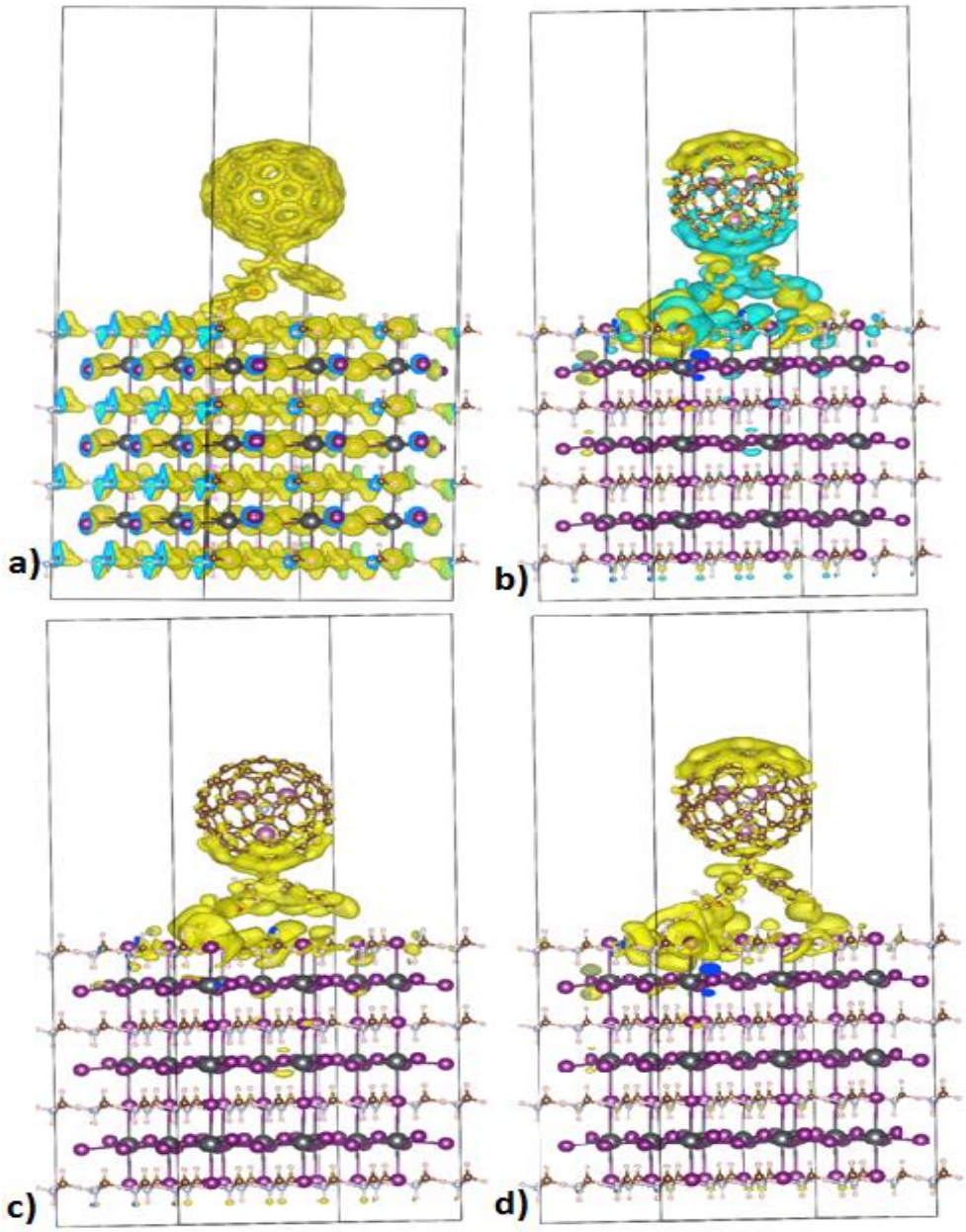

Figure 3.22: Charge density plots of (a)3x3x3 MAIT-$Sc_3N@C_{80}$-PCBM, (b) difference of density of 3x3x3 MAIT-Sc3N@C80-PCBM and the isolated components where positive difference is shown in yellow and negative difference is shown in blue, (c) only negative charge density difference is shown in yellow, and (d) only positive charge difference shown in yellow.

Table 3.4: Charge density difference values

SYSTEM	Threshold	minimum (e/Bohr3)	maximum (e/Bohr3)
225MAIT/Sc3N@C80	0.283	-0.0157	1.4129
333MAIT/Sc3N@C80-PCBM	0.283	-0.0042	0.0061

To understand the changes in the charge density that occurs due to interaction of the surface with the fullerene/PCBM layer, we plotted the charge density distributions of the interfaces. Charge density distribution before subtracting the corresponding surface and molecule are shown in Figs. 3.21 (a) and Fig. 3.22 (a). In Fig. 3.22 (b), the charge density difference plot is shown with positive charges represented by yellow and negative charges represented by green. To clearly understand the identity of charge distribution, we plotted only negative charges in Fig. 3.22 (c) while positive charges are hidden, and only positive charges while negative charges are hidden as shown in Fig. 3.22 (d). Both charges are represented by yellow in Figs. 3.22 (c) and (d). This picture shows accumulation of electron density on the fullerene and large charge density changes at the interface. Fullerene have high electron affinities and the flow of the electron toward fullerene at the interface occurs because of that.

In Table 3.4, the minimum and maximum values of charge densities together with their threshold values are presented. For better and meaningful comparison, the same threshold is used for both complexes. We notice that 225MAIT/Sc3N@C80 has higher charge concentration compared to the PCBM analogue complex.

The results for the local potential of these complexes and their corresponding isolated systems in the z-direction are shown in Figs 3.17-20. In these Figures, every geometry and its corresponding plot of the local potential in eV against its size in z-direction in Å is shown. The length of the supercell in Fig. 3.17 is 50 Å which includes the surface and $Sc_3@C_{80}$-PCBM between 2 Å and 23 Å, and the rest is filled with vacuum.

3.3.7: Interface with C_{60} Fullerenes and C60-DME

In this section, we consider C_{60} fullerene and its dimethyl-ether (DME) analogue as the electron transporting layer. The DME, 2.2.5MAIT surface, and their complex have a minimum energy of -155.03 eV, -1173.93 eV, and -1333.76 eV respectively. This system has binding energy of 0.8 eV at the PBE level. Figure 3.23 represents the DOS of DME showing a larger band gap of 4.21 eV.

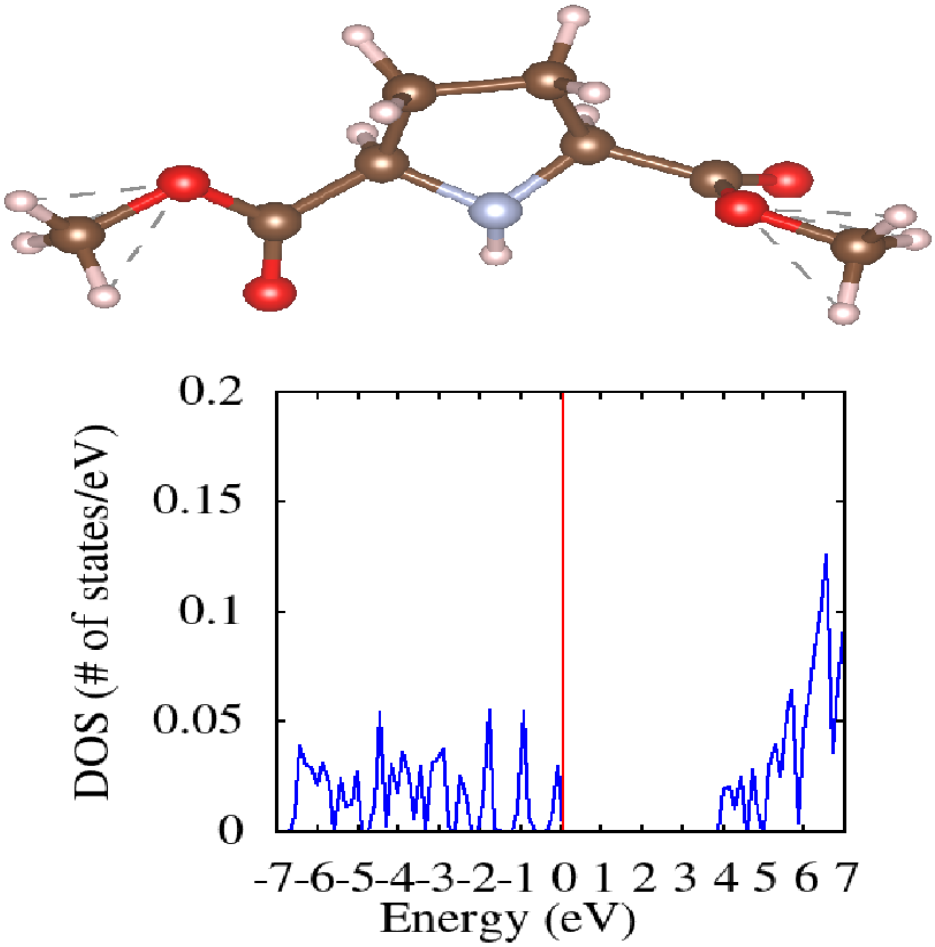

Figure 3.23: DOS and structure of dimethyl-ether (DME) molecule.

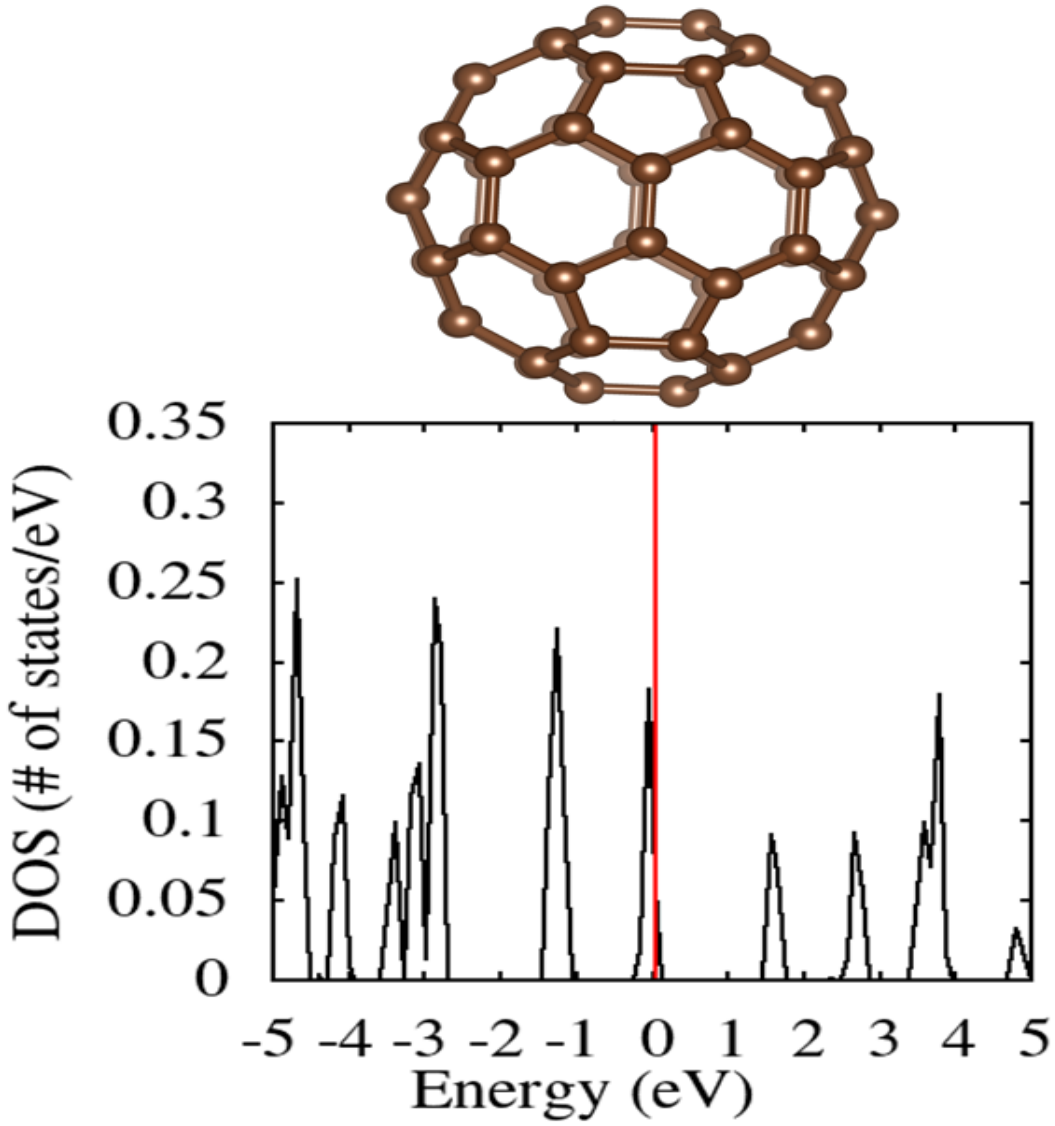

Figure 3.24: DOS and structure of C_{60} fullerene molecule.

The DOS for the isolated molecule of C_{60} fullerene is shown in Figure 3.24. Our calculated band gap of 1.63 eV is comparable to the photoemission measurements of C_{60}^- ions [42, 43].

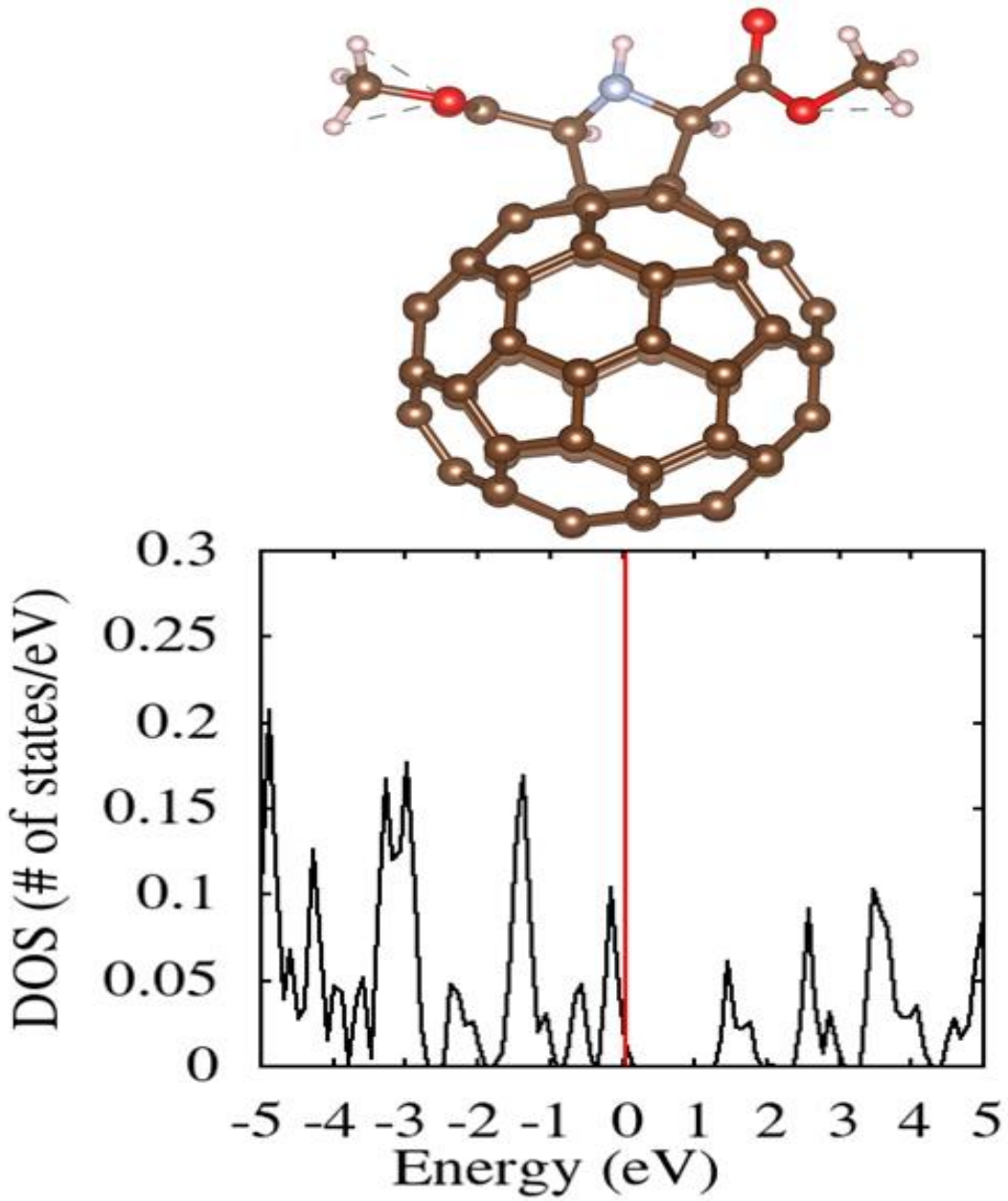

Figure 3.25: DOS and structure of C_{60}-DME molecule.

In Figure 3:25, the DOS of C_{60}-DME molecule has a band gap of 1.47 eV which is 0.16 eV lower than the C_{60} fullerene cage and 2.74 eV lower than the isolated DME. The C_{60}-DME is therefore a better electron extracting layer compared to the isolated C_{60} and isolated DME.

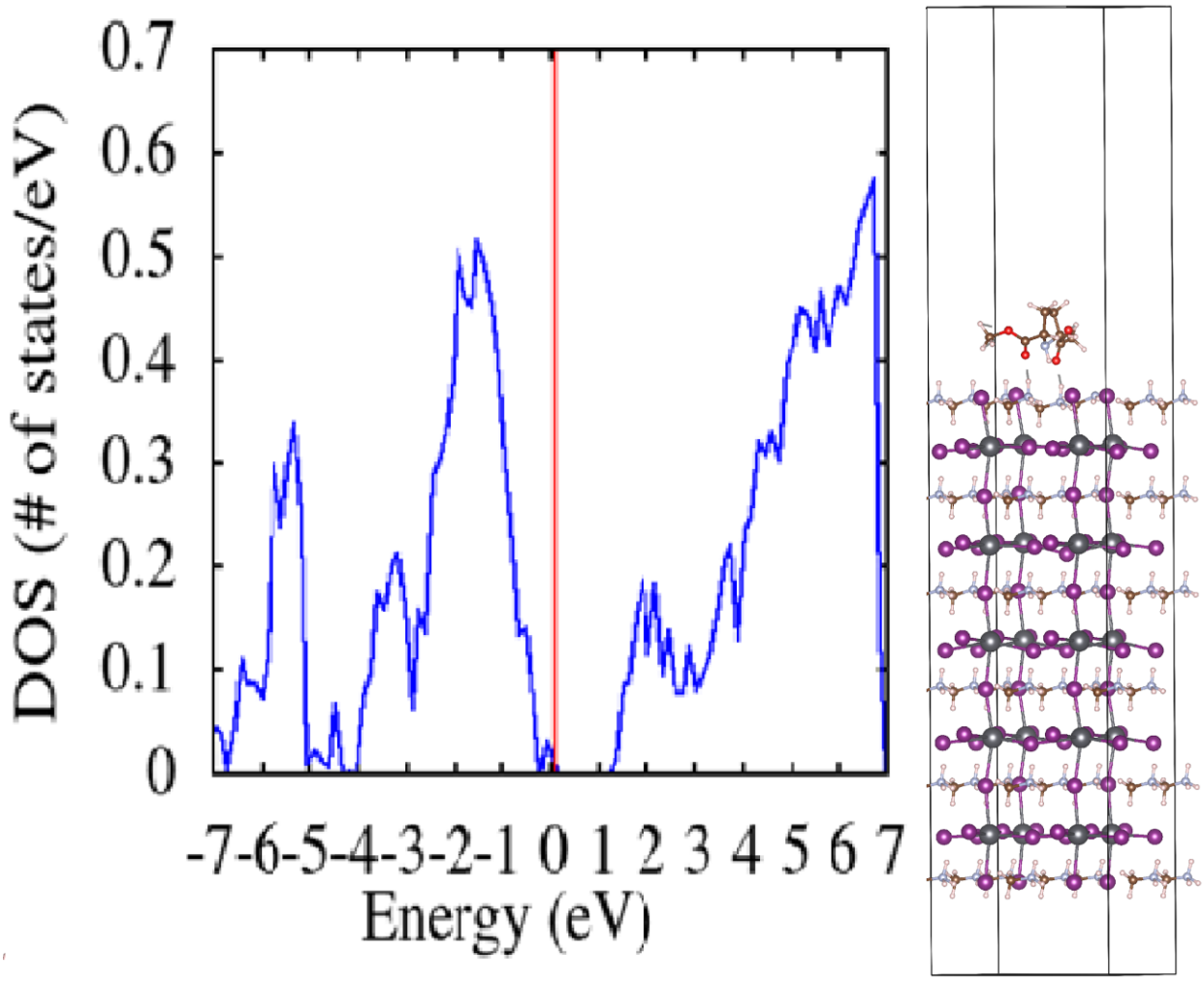

Figure 3.26: DOS and structure of 2.2.5MAIT-DME complex.

In Figure 3:26, the band gap obtained is 1.46 eV. This gap is lower than both the isolated surface and DME. Introducing the DME on the 2.2.5MAIT-Ntop surface creates an interface with an attractive PBE-binding energy of 0.8 eV. These configuration favors electrical conductivity than the isolated surface or DME. However, the perovskite interfaced with C_{60}-DME as in Figure 3.27 has a bandgap of 0.54 eV, a much smaller bandgap compared to the interface in Figure 3.26. The C_{60}-DME with the DME side (2x2x5MAIT/C_{60}DME_dn in figure 3.28) forming an interface with the perovskite is thus a better ETL compared to the fullerene side interfaced with the fullerene side (2x2x5MAIT/C_{60}DME_up in figure 3.27) . Table 3.5 shows a summary of PBE binding energies and the band gaps of C_{60}, DME, and their associated complexes.

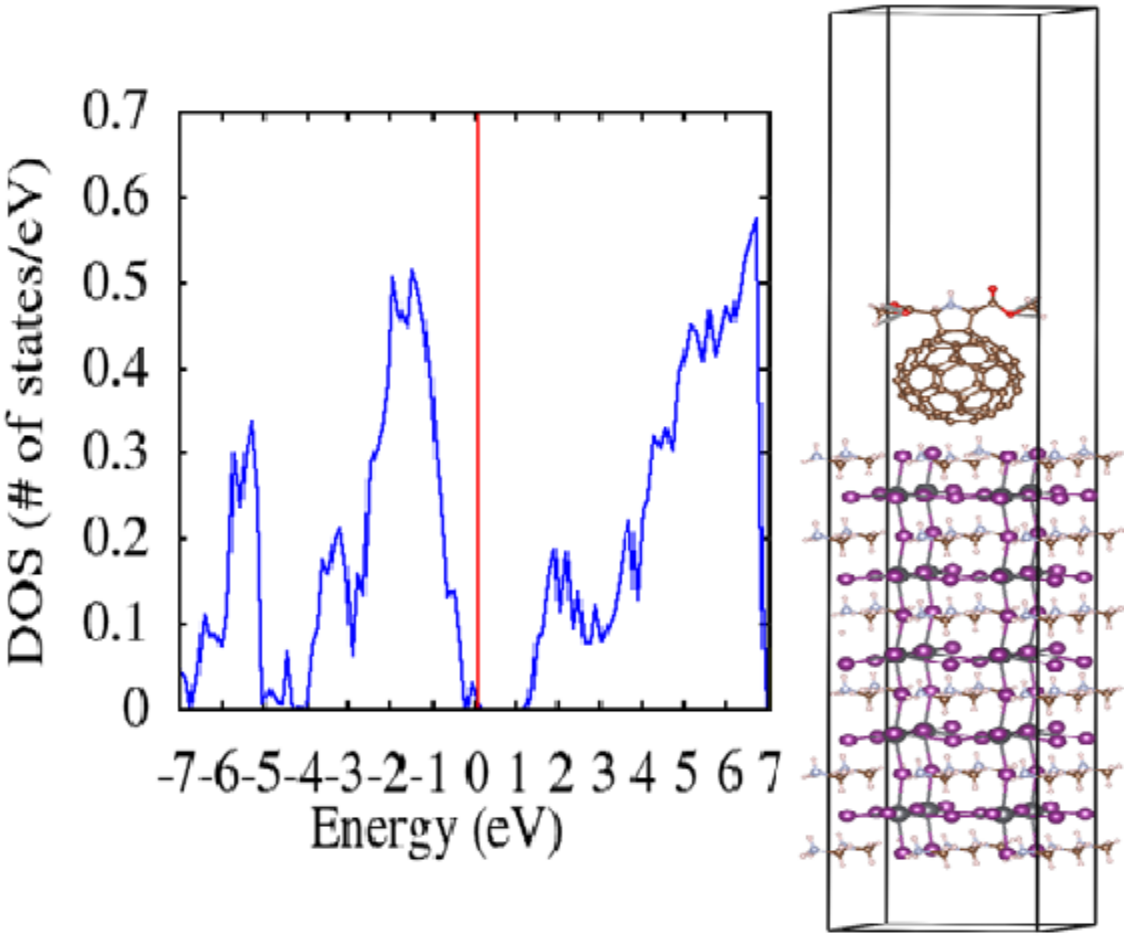

Figure 3.27: DOS and structure of 2x2x5MAIT/C60-DME complex with pentagonal face interfaced with perovskite surface

Table 3.5: Binding Energies and Band gaps of DME, C60, and their associated complexes.

	Total Energy (eV)	PBE-Binding energy (eV)	Band gap (eV)
DME	-155.03		4.2
2x2x5MAIT/DME	-1333.76	0.8	1.46
2X2x5MAIT surf	-1177.93		
2x2x5MAIT/C_{60}DME_dn	-1832.11	0.89	0.49
C_{60}	-531.31		1.63
DME-C_{60}	-653.29		1.47
2x2x5MAIT/C_{60}DME_up	-1831.3	0.08	0.54
2X2X5MAIT/C_{60}			

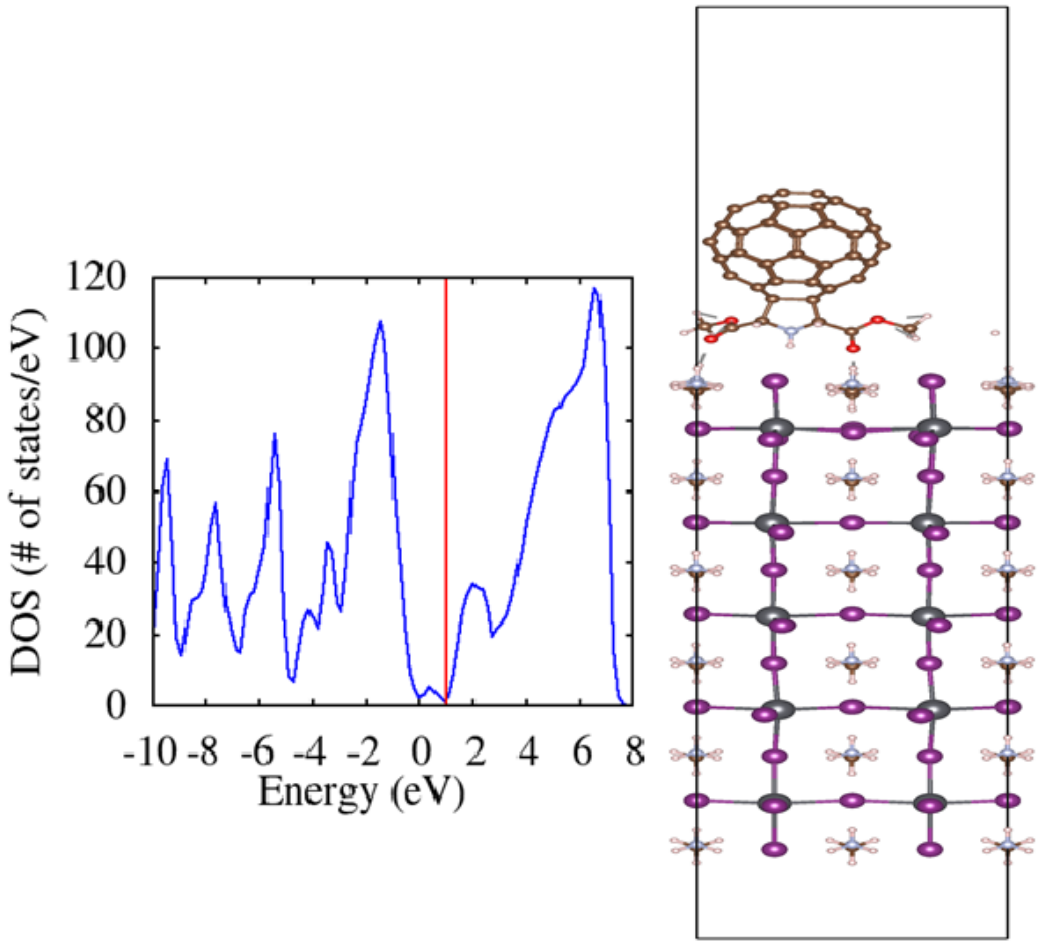

Figure 3.28: DOS and structure of 2x2x5MAIT/C60-DME complex with DME interfaced with perovskite surface.

In Figure 3.28, the DOS plot has the lowest band gap of 0.49 eV. This structure also has an attractive PBE binding energy of 0.89 eV. The highest binding energy in this structure among the C60 based complexes makes it more stable. It's also favored with absorptions in longer wavelength regions than other C_{60} complexes due to its lowest band gap.

3.4 CONCLUSION

We have investigated the interface formation between MAI- terminated surface of $MAPbI_3$ perovskite layer and endohedral metallofullerene derivatives viz, $Sc_3N@C_{80}$ and $Sc_3N@C_{80}$PCBM using DFT calculations. It is seen that C_{80} orientation in $Sc_3N@C_{80}$ has an important effect on the stability of the adlayers. The adlayer of $Sc_3N@C_{80}$PCBM with the topC perovskite surface becomes more stable with an interface binding energy increased by 0.65 eV in the presence of Van der Waals forces. The pentagonal face of $Sc_3N@C_{80}$ exhibits a repulsive interaction with topC surface of the perovskite in the absence of Van der Waals forces. However, the hexagonal face of the fullerene ring of $Sc_3N@C_{80}$ forms a stable interface with topN slab model with binding energy of 1.05 eV and 1.22 eV with and without Van der Waals interaction. Thus, the calculated binding energies show that it would be possible to adsorb metallofullerenes on perovskite surfaces, thereby opening the possibility of these molecules to serve as effective electron transport layers in perovskite solar cells.

REFERENCES

[1] O. Selina and M. Klaus, "Substrate-dependent electronic structure and film formation of MAPbI3 perovskites," *Scientific Reports,* vol. 7, p. 40267, 2017.

[2] A. Kojima, K. Teshima, Y. Shirai and T. Miyasaka, "Organometallic halide perovskites as visible-light sensitizers for photovoltaic cells," *J. of the American Chem. Soc.,* vol. 13, no. 17, p. 6050–6051, 2009.

[3] M. Saliba, T. Matsui, K. Domanski, J.-Y. Seo, A. Ummadisingu, S. M. Zakeeruddin, J.-P. Correa-Baena, W. R. Tress, A. Abate, A. Hagfeldt And M. Grätzel, "Incorporation of rubidium cations into perovskite solar cells improves photovoltaic performance," *American Association for the Advancement of Science,* vol. 354, no. 6309, pp. 206-209, 2016.

[4] Claudio, A. F. De and D. Beljonne., "Influence of surface termination on the energy level alignment at the $CH_3NH_3PbI_3$ perovskite/C60 interface," *Chem. Mater.,* vol. 29, no. 3, pp. 958-968, 2017.

[5] W. Geng, C.-J. Tong, Z.-K. Tang, C. Yam, Y.-N. Zhang, W.-M. Lau and L.-M. Liu, "Effect of surface composition on electronic properties of methylammonium lead iodide perovskite," *Journal of Materiomics,* vol. 1, no. 3, pp. 213-220, 2015.

[6] M. Kulback, D. Kahen and G. Hodes, "How important is the organic part of lead halide perovskitephotovoltaic cells? efficient CSPbBr3 cells.," *Phys. Chem. Lett.,* vol. 6, no. 13, pp. 2452-2456, 2015.

[7] W. S. Yang, J. H. Noh, N. J. Jeon, Y. C. Kim, S. Ryu, J. Seo and S. I. Seok, "High Performance photovoltaic perovskite layers fabricated through intramolecular exchange," *Science ,* vol. 348, pp. 1234-1237, 2015.

[8] Q. Lin, A. Armin, P. L. Burn and P. Meredith, "Organohalide perovskites for solar energy conversion," *Accounts of chemical Research ,* vol. 3, pp. 545-553, 2016.

[9] W.-J. Yin, J.-H. Yang, J. kang, Y. Yan and S.-H. Wei., "Halide Perovskite materials for solar cells: a theoretical review," *J. Mater. Chem. A,* vol. 3, pp. 8926-8942, 2015.

[10] P. Gao, M. Gratzel and M. K. Nazeeruddin, "organohalide lead perovskites for photovoltaic applications," *Energy and Environmental Science,* vol. 8, pp. 2448-2463, 2011.

[11] T. C. Sum and N. Mathews, "Advancements in perovskite solar cells: photophysics behind the photovoltaics," *Energy and environmental Sience,* vol. 8, pp. 2518-2534, 2014.

[12] P. Schulz, E. Edri, S. Kirmayer, G. Hodes, D. Cohen and A. Kahn, "Interface energetics in organ-metal halide perovskite-based photovoltaic cells," *Energy & Environmental Science,* vol. 7, no. 4, p. 1377–1381, 2014.

[13] C. Wehrenfennig, G. E. Eperon, M. B. Johnston, H. J. Snaith and L. M. Herz, "High charge carrier mobilities and lifetimes in organolead trihalide perovskites," *Advanced Materials,* vol. 26, no. 10, p. 1584–1589, 2014.

[14] W. A. Dunlap-Shohl, E. T. Barraza, A. Barrette, K. Gundogdu, A. D. Stiff-Roberts and D. B. Mitzi, "MAPbI3 Solar Cells with Absorber Deposited by Resonant Infrared Matrix-Assisted Pulsed Laser Evaporation," *ACS Energy Lett. ,* vol. 3, no. 2, pp. 270-275, 2018.

[15] J. H. Heo, D. H. Song, B. R. Patil and S. H. Im, "Recent progress of innovative perovskite hybrid solar cells," *Israel Journal of Chemistry,* vol. 55, no. 9, p. 966–977, 2015.

[16] J.-H. Im, C.-R. Lee, J.-W. Lee, S.-W. Park and N.-G. Park, "6.5% efficient perovskite quantum-dot-sensitized solar cell," *Nanoscale,* vol. 3, pp. 4088-4093, 2011.

[17] E. Mosconi, J. M. Azpiroz and F. D. Angelis, "Ab Initio Molecular Dynamics Simulations of Methylammonium Lead Iodide Perovskite Degradation by Water," *Chem. Mater. ,* vol. 13, no. 27, pp. 4885-4892, 2015, 27, 13, .

[18] J. Huang, S. Tan, P. D. Lund and H. Zhou, "Impact of H2O on organic–inorganic hybrid perovskite solar cells," *Energy Environ. Sci,* vol. 10, pp. 2284-2311, 2017.

[19] R.-P. Xu, Y.-Q. Li, T.-Y. Jin, Y.-Q. Liu, Q.-Y. Bao, C. O. Carroll and J.-X. Tang, "In Situ Observation of Light Illumination-Induced Degradation in Organometal Mixed-Halide Perovskite Films," *ACS Appl. Mater. Interfaces ,* vol. 10, no. 7, pp. 6737-6746, 2018.

[20] J. Haruyama, K. Sodeyama, L. Han and Y. Tateyama, "Termination Dependence of Tetragonal $CH_3NH_3PbI_3$ Surfaces for Perovskite Solar Cells," *The Journal of Physical Chemistry Letters,* vol. 5, no. 16, pp. 2903-2909, 2014.

[21] E. Mosconi, J. M. Azpiroz and F. D. Angelis, "Ab Initio Molecular Dynamics Simulations of Methylammonium Lead Iodide Perovskite Degradation by Water," *Chemistry of Materials,* vol. 27, no. 13, pp. 4885-4892, 2015.

[22] F. Zu, P. Amsalem, M. Ralaiarisoa, T. Schultz, R. Schlesinger and N. Koch, "Surface State Density Determines the Energy Level Alignment at Hybrid Perovskite/Electron Acceptors Interfaces," *ACS Applied Materials & Interfaces ,* vol. 9, no. 47, pp. 41546-41552, 2017.

[23] Y. Liu, M. Bag, L. A. Renna, Z. A. Page, P. Kim, T. Emrick, D. Venkataraman and T. P. Russell, "Understanding Interface Engineering for High-Performance Fullerene/Perovskite Planar Heterojunction Solar Cells," *Adv. Energy Mater.,* vol. 6, p. 1501606, 2016.

[24] Y. Shao, Z. Xiao, C. Bi, Y. Yuan and J. Huang, "Origin and elimination of photocurrent hysteresis by fullerene passivation in CH3NH3PbI3 planar heterojunction solar cells," *Nature Communications,* vol. 5, p. 5784, 2014.

[25] Q. Wang, Y. Shao, Q. Dong, Z. Xiao, Y. Yuan and J. Huang, "Large fill-factor bilayer iodine perovskite solar cells fabricated by a low-temperature solution-process," *Energy & Environmental Science,* vol. 7, no. 7, pp. 2359-2365, 2014.

[26] P. Liang, C. Chueh, S. T. Williams and A. K. Jen, "Roles of Fullerene-Based Interlayers in Enhancing the Performance of Organometal Perovskite Thin-Film Solar Cells," *Adv. Energy Mater.,* vol. 5, p. 1402321, 2015.

[27] L. K. Ono and Y. Qi, "Surface and Interface Aspects of Organometal Halide Perovskite Materials and Solar Cells," *The Journal of Physical Chemistry Letters,* vol. 7, no. 22, pp. 4764-4794, 2016.

[28] J. H. Heo, H. J. Han, D. Kim, T. K. Ahn and S. H. Im, "Hysteresis-less inverted $CH_3NH_3PbI_3$ planar perovskite hybrid solar cells with 18.1% power conversion efficiency," *Energy & Environmental Science,* vol. 8, no. 5, pp. 1602-1608, 2015.

[29] K. Zhang, H. Yu, X. Liu, Q. Dong, Z. Wang, Y. Wang, N. Chen, Y. Zhou and B. Song, "Fullerenes and derivatives as electron transport materials in perovskite solar cells," *Sci China Chem.,* vol. 60, no. 1, pp. 144-150, 2017.

[30] P. S. Whitfield, N. Herron, W. E. Guise, K. Page, Y. Q. Cheng, I. Milas and M. K. Crawford, "Structures, Phase Transitions and Tricritical Behavior of the Hybrid Perovskite Methyl Ammonium Lead Iodide," *Scientific Reports,* vol. 6, p. 35685, 2016.

[31] C. Quarti, E. Mosconi and F. D. Angelis, "Interplay of Orientational Order and Electronic Structure in Methylammonium Lead Iodide: Implications for Solar Cell Operation," *Chemistry of Materials,* vol. 26, no. 22, pp. 6557-6559, 2014.

[32] E. B. N and M. O'Keeffe, Complexes Clusters and Crystal Chemistry., Berlin: Springer, 1992.

[33] J. Ulises, N. N. Karle, T. Baruah and R. Zope, "Electronic and Structural Properties of C60 and Sc3N@C80 Supported on Graphene Nanoflakes," *Phys. Chem,* 2016.

[34] W. I. F. David, R. M. Ibberson, J. C. Matthewman, K. Prassides, T. J. S. Dennis, J. P. Hare, H. W. Kroto, R. Taylor and D. R. M. Walton, "Crystal Structure and bonding of ordered C60," *Nature,* vol. 353, pp. 147-149, 1991.

[35] D. R. Cooper, D. Benjamin, G. Nageswara and etal, "Experimental review of graphene," *Condensed Matter Phys,* vol. 2012, pp. 1-56, 2012.

[36] S. Stevenson, G. Rice, T. Glass, K. Harich, F. Cromer, M. R. Jordan, J. Craft, E. Hadju, R. Bible, M. M. Olmstead, K. Maitra, A. J. Fisher, A. L. Balch and H. C. Dorn, *Nature,* vol. 401, pp. 55-57, 1999.

[37] W. M. Haynes, CRC Handbook of Chemistry and Physics, 94th Edition, New York: CRC Press, 2016.

[38] Y. Yamada, T. Nakamura, M. Endo, A. Wakamiya and Y. Kanemitsu, "Near-band-edge optical responses of solution-processed organic–inorganic hybrid perovskite CH3NH3PbI3 on mesoporous TiO2 electrodes," *Appl. Phys. Express,* vol. 7, no. 3, p. 032302, 2014.

[39] C. Lung-Chien and W. Chiao-Yu, "Optoelectronic Properties of MAPbI3 Perovskite/Titanium Dioxide Heterostructures on Porous Silicon Substrates for Cyan Sensor Applications," *Nanoscale Research Lett.,* vol. 10, p. 404, 2015.

[40] Y. Yuan, R. Xu, H-T. Xu, F. Hong, F. Xu, and L-J Wang, "Nature of the bandgap of halide perovskites s ABX3 (A = CH3NH3, Cs; B= Sn, Pb; X = Cl, Br, I): First-principles calculations," *J.. Chinese Physics B,* vol. 2411, no. 11, p. 116302, 2015.

[41] A. Poglitsch and W. D, "Dynamic disorder in methylammoniumtrihalogenoplumbates (II) observed by millimeter-wave spectroscopy," *J. Chem. Phys.,* vol. 87, p. 6373, 1987.

[42] R. E. Haufler, Y. Chai, L. P. F. Chibante, M. R. Fraelich, R. B. Weisman, R. F. Curl and R. E. Smalley, "Cold molecular beam electronic spectrum of C60 and C70," *J. Chem. Phys.,* vol. 95, p. 2197, 1991.

[43] B. Miller, J. M. Rosamilia, G. Dabbagh, R. Tycko, R. C. Haddon, A. J. Muller, W. Wilson, D. W. Murphy and A. F. Hebard, "Photoelectrochemical behavior of C60 films," *J. Am. Chem. Soc.,* vol. 113, no. 16, p. 6291–6293, 1991.

[44] J. Liang, C. Wang, Y. Wang, Z. Xu, Z. Lu, Y. Ma, Y. H. Hongfei Zhu, C. Xiao, X. Yi, G. Zhu, H. Lv, L. Ma, T. Chen, Z. Tie, Z. Jin and J. Liu, "All-Inorganic Perovskite Solar Cells," *J. Am. Chem. Soc.,* vol. 49, no. 138, pp. 15829-15832, 2016.

[45] D. B. Mitzi, "Templating and structural engineering in organic–inorganic perovskites," *Royal Soc. Chem. ,* pp. 1-12, 2001.

CHAPTER 4: OLIVINE $Mn_2S_iS_{4-X}Se_x$

4.1 INTRODUCTION

Divalent transition metal cations such as Mn^{2+}, Ni^{2+}, Co^{2+} are the principal constituents in the olivine family. An olivine is generally a group of minerals commonly found in the earth mantle. The rising attention for new materials in the market with unique physical, chemical, and magnetic properties that meet the demands for modern technology could apply to the olivine family. A variety of olivine have has been a center of attention for most crystallographers, mineralogists [1, 2, 3], and other researchers. For over three decades, many researchers have made considerable effort investigating the magnetic properties of low dimensional transitional cations mostly the chalcogenides [4, 5]. While investigating the chalcogenides, these researchers extended their search towards the right side of the periodic table. One of the most interesting findings includes the ferromagnetic ordering [6, 7], observed below 33 K and 66 K in Chromium ternary tellurides [6, 7]. The scientific study for magnetic properties proceeded until Gopalakrishnan et. al. investigated silicon selenides, a member of A_2BX_4 olivine family in 1980s [8]. From around this time, many researchers started shifting their efforts to the olivine members with well-ordered magnetic phases at low narrow temperature regions [9, 10, 11, 12]. They used several methods that include such magnetic measurements at low temperatures [12], high high-resolution specific heat measurements [13], Rietveld refinement study of the low-temperature magnetic structure [11], and neutron diffraction measurements [14] among. This led to the realization of unique structural, magnetic, and electrical behavior in the olivine that predominantly posed important applications.

In this work we investigate the spin ordering in Mn_2SiS_4 system. Lamarche et. al. performed neutron diffraction experiments at 83-86 K and established that the manganese ions in Mn_2SiS_4 have an easy magnetic spin axis along the a-direction [9]. The manganese ions were also found to be antiferromagnetic with some spins alignment along the a-axis while others (opposite spins) along the c-axis. The two sites have inequivalent symmetries - inversion and mirror. These

metallic ions tend to depart from the antiferromagnetic phase at temperatures below 83K and become collinear at 4.2K on their b-axis. This narrow gap of 83-86K is the onset of the unique behavior for Mn_2SiS_4 that initiates the spontaneous magnetization that makes Mn_2SiS_4 a potential candidate to be used in the design of particle detectors [10]. A particle detector is an apparatus used to detect, track, and identify ionizing particles, such as those produced by radioactivity, cosmic radiation, or reactions in a particle accelerator. Since particle physics is one of the active fields in physics, there is a huge demand in particle detectors that allow precise and accurate signal processing.

The trio magnetic phases [13] of Mn_2SiS_4 (antiferromagnetic below temperature 83K, weak ferromagnetic between 83–86K, and paramagnetic above 86K) make this material very unique, and this property has attracted the attention from the research community. Neutron diffraction analysis [9, 10] and study of magnetization as a function of temperature from 4.2K to 250K uncovered the functionality of Mn_2SiS_4 based on the position of Mn^{2+} ions. There are 8 Mn^{2+} ions in a unit cell. These ions are divided into two groups of 4: one group on the 4a sites of inversion symmetry and the other on the 4c sites of mirror symmetry. While these experiments showed antiferromagnetic ordering up to 83K, they also revealed the alignment of the 4a and 4c spins along the b-axis at liquid helium temperatures and re-orientation of the 4a spins to the ab-plane reaching an angle of 32° as the temperature approaches near 83 K. At 83K, the system undergoes the phase transition to the weak ferromagnetic phrase, and magnetization strength increments sharply as the temperature increases initially but then falls slowly until the temperature reaches 86K. Within this 3K interval, the magnetic group is transformed from Pnma to Pn'm'a. This renders canting in the ac plane giving rise to non-zero moments along the c-direction for both groups of Mn^{2+} but of unequal magnitude and of opposite spins. The difference in the magnetic moments at this region is responsible for spontaneous magnetization, which makes Mn_2SiS_4 feasible for applications in high energy particle detectors.

On the same case, the first olivine selenide Mn_2SiSe_4 was discovered and established to be antiferromagnetic at T < 65 K [12]. This changed the previous misperception that oxides and sulfides as the only known olivines. The magnetic measurements analyzed from helium temperature to room temperature suggested antiferromagnetic spin interactions in this selenide. To determine its structure, Fuhrmann and Pickardt compared the similarity of the cell parameters with Mn_2SiS_4 [15] and the space groups taken from Weissenberg photographs that revealed isotypic structures. This information was enough to confirm that Mn_2SiSe_4 crystallizes in the olivine structure. For the magnetic measurements at higher temperatures (above 150 K), Mn^{2+} in Mn_2SiSe_4 was $\mu_{eff} = 5.92\mu_B$ thus permitting paramagnetic phase in antiferromagnetic predominance. At temperatures around 65K, a sharp peak in magnetization is observed which could be analogous to the Mn_2SiO_4 and Mn_2SiS_4 [9, 1].

The Mn_2SiSe_4 in 90s was the latest olivine that had new different ways the Mn (II) moments can be ordered. As established by Ref [11] in their Rietveld study at the low-temperature magnetic structure, Mn_2SiSe_4 has its easy spin axis parallel to the c-axis. The c-axis had been known to be a hard axis for all olivine sulfides and oxides [1, 2]. Neither had they shown spin canting disorder nor short-range order.

It's therefore very important to point at the temperatures around 66K and 83K as critical for Mn_2SiSe_4 and Mn_2SiS_4. These compounds have spontaneous magnetization, and their magnetic phases are well ordered at the said temperature regions. Since the two temperatures (66 K and 83 K) are very close, it would be very interesting to study the structure transformations between Mn_2SiS_4 and Mn_2SiSe_4. This will be done by replacing S with Se sequentially until all the S are substituted. The details are discussed in Section 4.3.

4.2 MOTIVATION

The olivine family is also well known to be magnetically semiconducting material. The nature of their magnetic semiconducting components is favorable in magnetic and optoelectronic applications [16]. Extensive investigations done performed by Yu et. al. and Fredrick et. al. [17, 18] show that these materials can be used as photovoltaic absorbers. In their work, they show the octahedron, FeS_6 distortion just as the distortions observed in other systems such as MnS_6 and $MnSe_6$ in Mn_2SiS_4 and Mn_2SiSe_4 respectively. The metal ions Fe^{2+} in the olivine structure just like Mn^{2+} also occupy the unique locations of 4a and 4c Wyckoff positions. Since they do have the same structure, we believe the Mn^{2+} based olivine with S and Se chalcogens will have similar applications.

The magnetic properties of Mn_2SiS_4 have attracted attention over the past four decades due to the location of Mn^{2+} ions in the 4a and 4c symmetry sites [11] that led to the unusual ordering of the spins. Neutron diffractions and magnetic measurements by Bodénan in Ref [11] further revealed collinear, canted antiferromagnetic, and ferromagnetic ordering at low temperatures [2, 19]. Most particularly, spontaneous magnetization in Mn_2SiS_4 at the small temperature window of 3K between 83 K and 86 K allows this olivine to be applied to high energy particle detectors [10]. Similarly, the antiferromagnetic phase also exists in Mn_2SiSe_4 at temperatures below 65 K as it is revealed in magnetic susceptibility data [12].

It is, therefore, worth mentioning that Mn_2SiS_4 and Mn_2SiSe_4 olivine structures have not been explored to the much-needed attention as seen in oxides and other non-Mn-based sulfides. The well-ordered magnetic phase at low temperatures and the spontaneous magnetism within a narrow temperature window remains a driving factor to study the very important applications such as the ones attributed to magnetism, photovoltaics, and magneto-electronics. With the motivations mentioned above, we intend to study the structural, magnetic, and electronic properties of $Mn_2SiS_{4-x}Se_x$ where the value of x is varied from x = 0 to x = 4 through first principle study calculations.

4.3 CRYSTAL STRUCTURE

The olivine structure of Mn_2SiS_4 and Mn_2SiSe_4 crystallizes in orthorhombic structure with a space group of pnma [9, 10, 13]. The Mn^{2+} uniquely occupies two distinct sites: site of inversion symmetry and that of mirror symmetry. One-half of the Mn atoms lay on the inversion symmetry and the remaining half on the mirror symmetry. Thus, one site of Mn atoms distinctly occupies one-half of the octahedral sites in the b-direction that increments as $x + 0.25$ and $x + 0.75$. The other distinct site is the mirror symmetry where the Mn atoms lay at the center of the symmetry and all the octahedral sites occupied along the b-direction at either 0 or 0.5 depending on the nature of the selenide. The silicon occupies one-eighth of tetrahedral sites in the (a, b) plane that renders it zig-zag [12] in b-direction.

The primitive cell contains 28 atoms, i.e. 8 Mn atoms, 4 Si atoms, and 16 S atoms. Similar to the $MnSe_6$ in Mn_2SiSe_4, the Mn cation and S anion in Mn_2SiS_4 form a distorted MnS_6 octahedron at 4a and 4c independent Wyckoff positions [20]. This cell is consistent with other olivines that have metal ions which lays at the vertices of corner-sharing triangles. This explains the reason for a repeated saw-like tooth shape [21] in such structures. This phenomenon was confirmed in Mn^{2+}, Ni^{2+}, and Co^{2+} olivine by Hagemann et. al. while investigating in geometrically frustrated magnetic materials.

The inequivalent positions of the sulfur atoms, a silicon atom, and the Wyckoff positions of Mn_2SiS_4 are represented in Table 1. These positions are extracted from Mn_2SiS_4 crystallographic information file (cif) using VESTA. The plot for these positions is shown in Fig. 4.1

Table 4.1: Inequivalent atomic positions for Mn_2SiS_4

Atom no.	Atom	X	Y	z
1	S (1)	0.337300	0.033200	0.222200
2	S (2)	0.053100	0.250000	0.278900
3	Mn (1)	0.222700	0.250000	0.508500
4	Si	0.406000	0.250000	0.073600
5	S (3)	0.408400	0.250000	0.734700
6	Mn (2)	0.000000	0.000000	0.000000

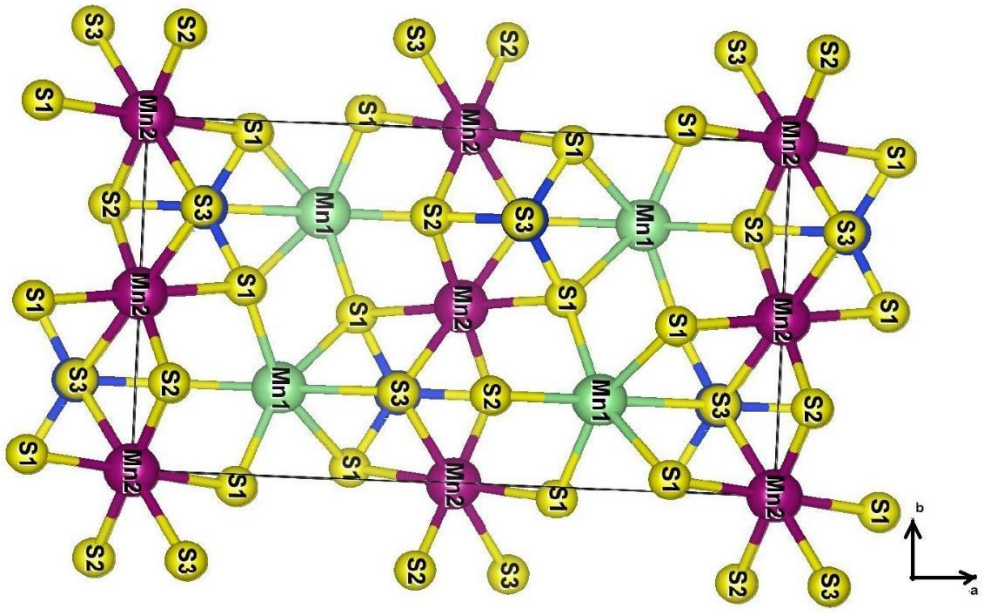

Figure 4.1: The Olivine structure of Mn_2SiS_4 on the a-b plane from cif as shown in Table 4.1

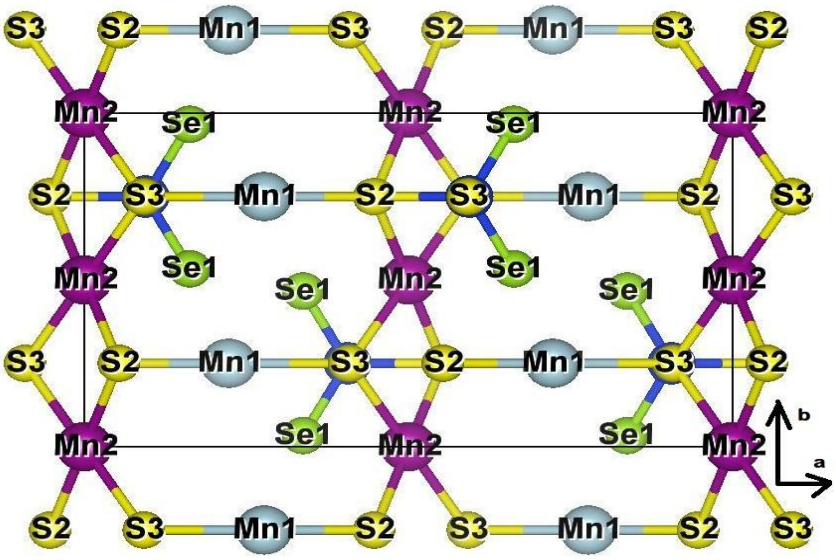

Figure 4.2: The Mn2SiS2Se2 structure a-b plane formed when S (1) position in Table 4.1 is substituted with a selenium atom.

The MnS_6 distortion observed in Mn_2SiS_4 on both Mn (1) and Mn (2) atoms disappears when the sulfur atom at S (1) position is substituted with a selenium atom. The newly formed structure of a chemical formula $Mn_2SiS_2Se_2$ has the MnS_2 and MnS_4 at Mn (1) and Mn (2) positions respectively.

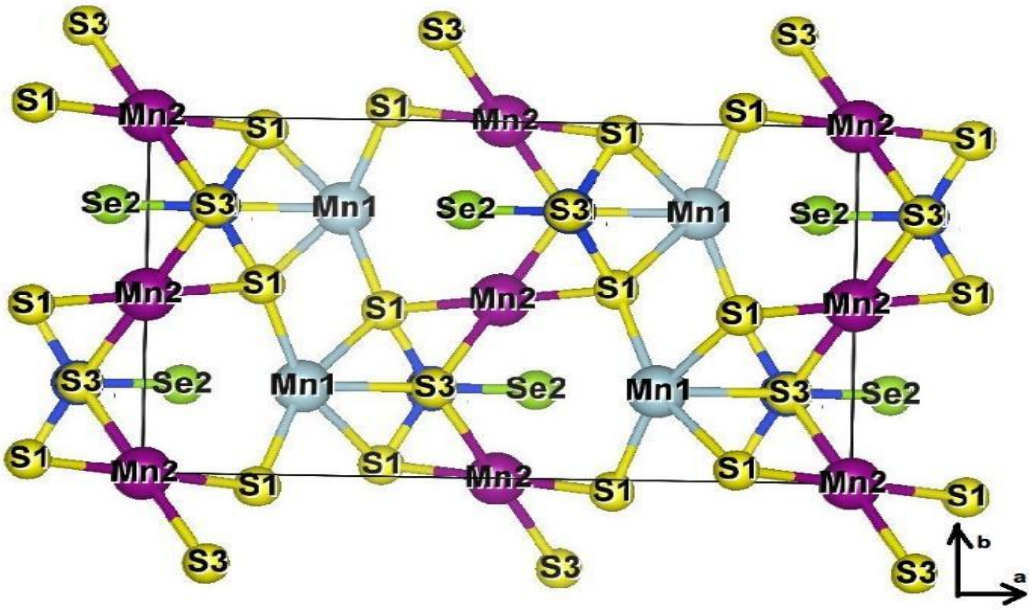

Figure 4.3: The Mn_2SiS_3Se structure in the a-b plane formed when S (2) position in Table 4.1 is replaced with a selenium atom.

Two structures with a chemical name Mn_2SiS_3Se is formed when the sulfur atom at either S (2) or S (3) is replaced by a selenium atom separately as shown in Fig. 4.3 and Fig. 4.4 respectively. This leads to a different phenomenon if compared to the MnS_6 in the parental structure of Mn_2SiS_4. Unlike MnS_2 and MnS_4 in Mn (1) and Mn (2) positions of $Mn_2SiS_2Se_2$, Mn_2SiS_3Se forms a distorted MnS_4 at both Mn (1) and Mn (2) positions. The Mn_2SiSSe_3 structures shown in Fig.4.5 and Fig. 4.6 are formed because of two inequivalent positions of sulfur atoms in Mn_2SiS_4 substituted by selenium atoms. For instance, the S (1) and S (2) sulfur positions when replaced with selenium atoms leads to Mn_2SiSSe_3 structure as shown in Fig. 4.5. Similarly, the structure shown in Fig. 4.6 is formed because of S (1) and S (3) sulfur atoms replaced by selenium atoms. Both Figs. 4.5 and 4.6 show the olivine structure of a chemical name Mn_2SiSe_3.

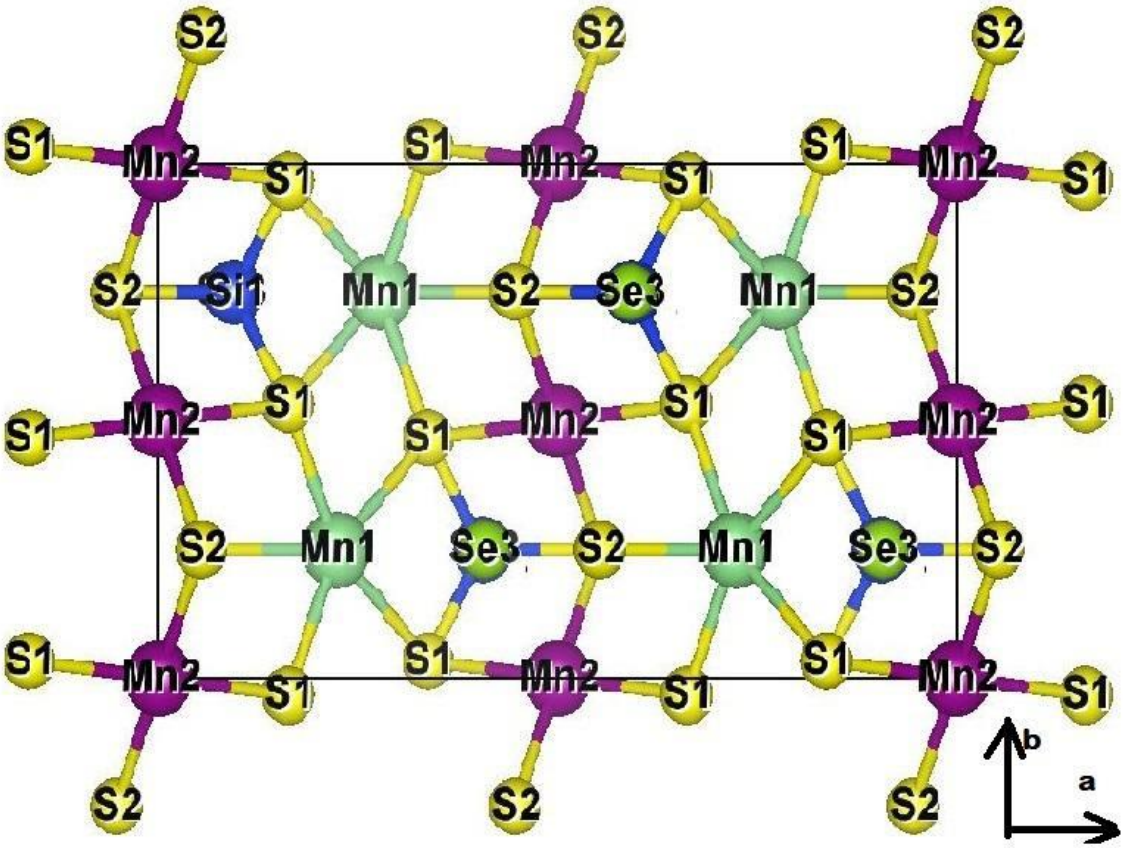

Figure 4.4: Another Mn_2SiS_3Se structure in the a-b plane formed when S (3) in Table 4.1 is replaced with a selenium atom.

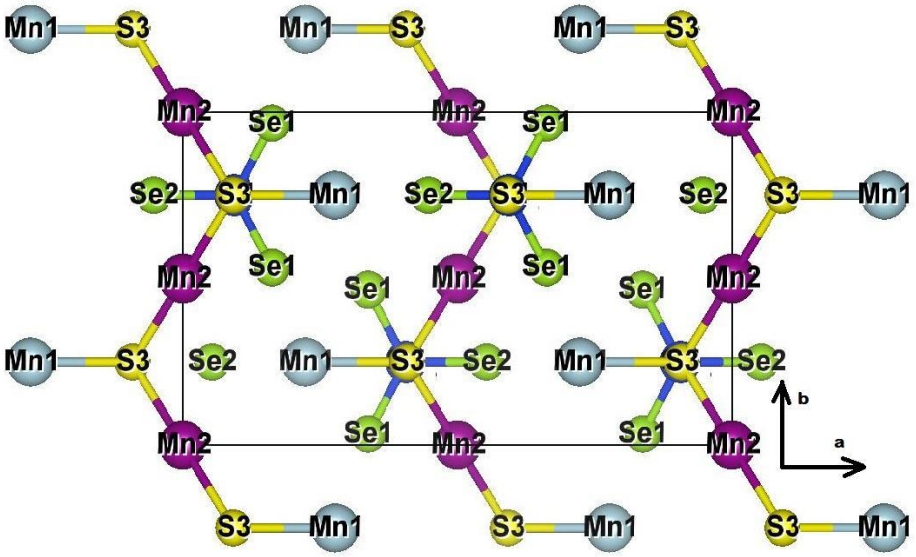

Figure 4.5: Mn_2SiSSe_3 structure on the a-b plane formed when S (1) and S (2) Sulphur positions in Table 4.1 are replaced with the selenium atoms.

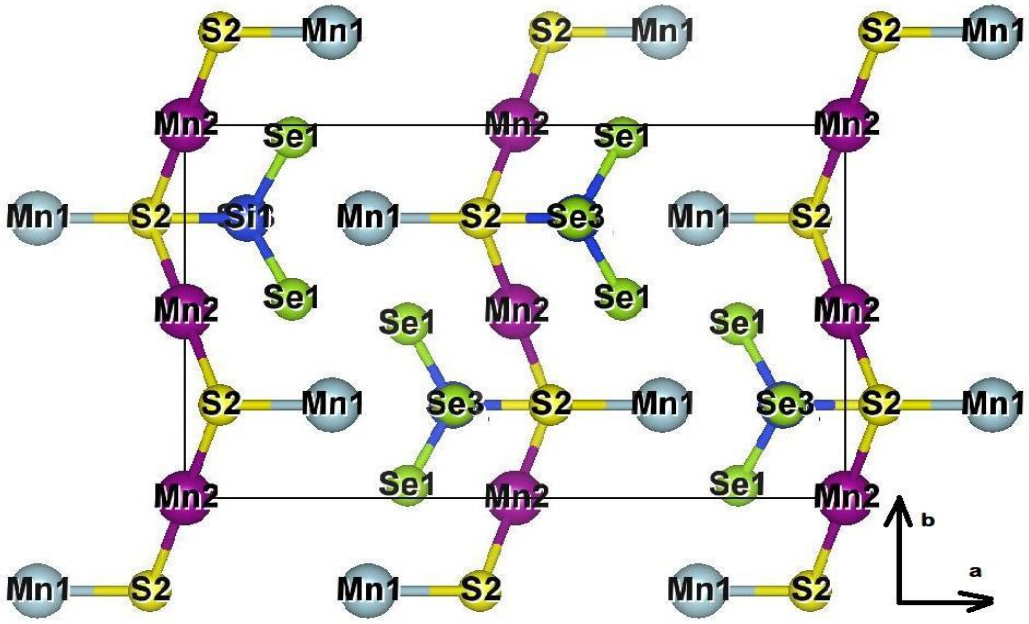

Figure 4.6: Another $Mn_2SiSSe3$ structure on the a-b plane formed when S (1) and S (3) Sulphur positions in Table 4.1 are replaced with the selenium atoms.

The Mn_2SiSe_3 structure also distinguishes itself structurally from the structures in Figs 4.1–4.4 with reference to the Mn atoms at Mn (1) and Mn (2). The Wyckoff positions in this structure could form a distorted MnS for Mn (1) and MnS_2 for Mn (2) positions respectively. The structures represented above (Fig. 4.1–4.6) are the initial structures formed in $Mn_2SiS_{4-x}Se_x$ at x=0 to x=4.

4.4 COMPUTATIONAL METHOD

The density functional theory (DFT) calculations are carried out using the Vienna ab initio simulation package (VASP) [22, 23, 24]. The projector augmented wave (PAW) method is utilized for the electron-ion interaction [25, 26, 27] with an energy cutoff of 470 eV for the plane-wave basis functions. The generalized gradient approximation to exchange-correlation functional by Perdew, Burke, and Ernzhofer is used. A Γ−centered (4×4×4) k-point grid based on the Monkhorst-Pack scheme [28] is employed for initial structure optimization and later a finer grid of 6×11×13 is used for further refinement. We have relaxed the structures until the Hellmann-Feynman forces on the ions become below 0.04 eV/A. Our energy convergence criterion for electronic self-consistent loop is 10^{-8} eV. An initial spin moment of 5 μ_B is assigned to Mn ions and the spin moment is then allowed to relax. We also used VESTA [29] software package for generating the crystal structures.

Table 4.2. The ground state energies for antiferromagnetic (AFM) and ferromagnetic (FM) ordering in eV, magnetic dipole moment (μB), and the bandgap in eV of various systems of the DFT calculations.

System	E(AFM) (eV)	Lattice constants (Å)	Expt. Lattice constants (Å)	E(FM) (eV)	Avg. spin moment/ Mn (μ_B) (AFM)	Expt. spin moment/Mn(μ_B) (AFM)	Avg. spin moment/ Mn (μ_B) (FM)	Band gap (eV)
Mn_2SiS_4	-189.91	a=12.46 b=7.27, c= 5.88	a=12.69 b=7.44, c= 5.94	-188.27	4.04, -4.04	4.0	4.15	0.47
Mn_2SiS_4	-189.51	a=12.69 b=7.44, c= 5.94		-188.59	4.12, -4.12	4.0	4.21	0.64
Mn_2SiS_3Se (a)	-185.33	a=12.726, b=7.320, c=5.892	a=12.860, b=7.527, c=6.009		4.03, -4.03	4.07		
Mn_2SiS_3Se (b)	-185.32	a=12.53, b=7.32, c= 6.01			4.04, -4.04	4.07		0.40
Mn_2SiS_3Se (1)	-185.67	a=12.59 b=7.35, c= 5.91	a=12.86, b=7.53, c=6.01	-184.43	4.02, -4.02	4.07	4.1	0.32
Mn_2SiS_3Se (2)	-185.65	a=12.583, b=7.335, c=5.942			4.02, -4.03			
Mn_2SiS_3Se (3)	-185.55	a=12.590, b=7.34, c= 5.96			4.04, -4.02			
Mn_2SiS_3Se (4)	-185.57	a=12.603, b=7.338			4.02, -4.03			

		, c= 5.915						
$Mn_2SiSe_2S_2$	-181.32	a=12.58 b=7.34, c= 5.96	13.000, 7.605, 6.076	-179.96	3.97, -3.97	3.95	4.0	0.33
$Mn_2SiSe_2S_2$ (b)	-181.39	a=12.538 b=7.432, c= 5.893	13.000, 7.605, 6.076	-179.96	3.97, -3.97	3.95	4.0	0.34
Mn_2SiSe_3S (1)	-176.79	a=12.61, 7.34, 6.00			3.91	3.8	3.9	
Mn_2SiSe_3S (2)	-176.97	a=12.58 b=7.33, c=5.99			3.897	3.8		
Mn_2SiSe_3S (a)	-177.67	a=12.75 b=7.45, c= 5.92	13.150, 7.690, 6.156	-175.64	3.92, -3.92	3.8	3.9	0.1
Mn_2SiSe_4	-174.07		a=13.30 b=7.78, c=6.24	-173.54	4.12	5.9	4.2	0.45

4.5 RESULTS

4.5.1 Structural and magnetic properties

We started with the experimental crystal structure of the Mn_2SiS_4, which is the structure at the room temperature. This structure is used as the initial structure for all the intermediate compounds $Mn_2SiS_{4-x}Se_x$ where the value of x is varied from 0 to 4. The crystal symmetry for all the structures is orthorhombic with six inequivalent positions. The substitution of one S by Se (x=1) leads to three structures; two with the same formula unit of Mn_2SiS_3Se and one with $Mn_2SiS_2Se_2$. Similar substitution by two Se atoms (x=2) also leads to three structures: two with the same formula unit of Mn_2SiSSe_3 and one with $Mn_2SiS_2Se_2$. Other two structures using the same set of inequivalent atom positions are Mn_2SiS_4 and Mn_2SiSe_4 for x=0 and x=4 respectively, which are the terminal structures in this case.

Apart from these structures mentioned above, we also tested mixed structures with random substitutional positions which led to Mn_2SiS_3Se and $Mn_2SiS_2Se_2$ based on atom count but different symmetry or chemical formula. These structures are generated using random substitution in alloys. However, we find that some of these structures have lower energy than the structures that conform to form the orthorhombic symmetry and therefore we include them in the results.

The Mn_2SiS_3Se symmetry structures are identified as Mn_2SiS_3Se (a) and Mn_2SiS_3Se (b) in Table 2.2 and shown in Fig. 4.3 and Fig. 4.4 respectively. The minimum energies of these two structures differ by 0.01 eV and by 0.34 eV and 0.35 eV respectively from the most stable mixed structure of Mn_2SiS_3Se. For Mn_2SiSSe_3, the orthorhombic structure has the lowest energy; lower by 0.7 eV and 0.88 eV from the available mixed structures. The last intermediate structure, $Mn_2SiS_2Se_2$ has its orthorhombic lower by 0.07 eV from its corresponding mixed structure.

The calculations are carried out for the antiferromagnetic spin ordering of the four different single crystals. Both the lattice parameters and the ionic positions are optimized for the antiferromagnetic state. The optimized lattice constants spin magnetic moments, and the band gaps of these systems are summarized in Table 4.I. The optimized lattice constants for all the four systems are found to be smaller than the experimental lattice constants with the PBE functional.

For each of the mixed $Mn_2SiS_xSe_{4-x}$ systems, all different configurations are investigated. For example, mixed Mn_2SiS_3Se has four different configurations. The lattice constants for the lowest energy configuration are presented in Table 4.I. The average spin moments on the Mn ions for the compounds in the antiferromagnetic state vary from 4.04 to 4.12 μ_B. The average spin moment decreases as the content of the Se is increased. The calculated spin magnetic moments of the Mn ions follow the trend seen in the experiment for the mixed compounds [30]. We note that the lattice size plays an important role in the determination of the spin moment. The PBE optimized lattice constants are smaller compared to the experimentally measured ones. Using the experimental lattice parameters leads to decreased interaction between the atoms, and as a result, the Mn ions have a higher magnetic moment for the experimental lattice. However, the total energies for the experimental lattice are found to be higher than the optimized lattice except for the $MnSiSe_4$. The potential energy surface of Mn_2SiSe_4 presents several local minima. The total energy with the experimental lattice is the lowest for this system. The spin magnetic moment for the local minima varies between 3.64–3.9 μ_B whereas the minimum energy configuration gives a moment of 4.12 μ_B. This value is much lower than the experimentally determined value of 5.9 μ_B per Mn atom. The experimental moment for this system is determined from data collected at a high temperature where lattice expansion can play a role in decreasing the interaction between the atoms. The DFT calculations are carried out at T=0K and lattice expansions are not considered.

4.5.2 Electronic properties

The band structures of the two terminal compounds, Mn_2SiS_4 and Mn_2SiSe_4, are shown in Figs. 4.7 and 4.8. The bandgaps of Mn_2SiS_4 and Mn_2SiSe_4 are found to be 0.47 eV and 0.45 eV respectively. Both structures have a direct bandgap as indicated by the valence band maximum (VBM) and conduction band maximum (CBM) at gamma point (G). The band structures have flat bands from G-X crystallographic direction and these features are similar to the Fe_2GeS_4 and Fe_2GeS_4 band structure plots obtained by Gudelli and Kanchana [31].

The corresponding total and projected density of states (DOS) for Mn_2SiS_4 and Mn_2SiSe_4 are represented in Figs. 4.9 and 4.10 respectively, and their PDOS are shown in Figs. 4.11 and 4.12. The DOS shows that the states near the Fermi level arise mainly from the Mn *d*-states and S/Se *p* states. In both systems, the Si states lie deeper in energy. The conduction band has contribution mainly from the Mn *d*-states. Both VBM and CBM for Se *p*-bands are flat compared to the sharp peaks for sulfur VBM, and sulfur CBM is a relatively smaller flat band that is roughly 1.4 eV thicker compared to 1.7 eV of selenium CBM.

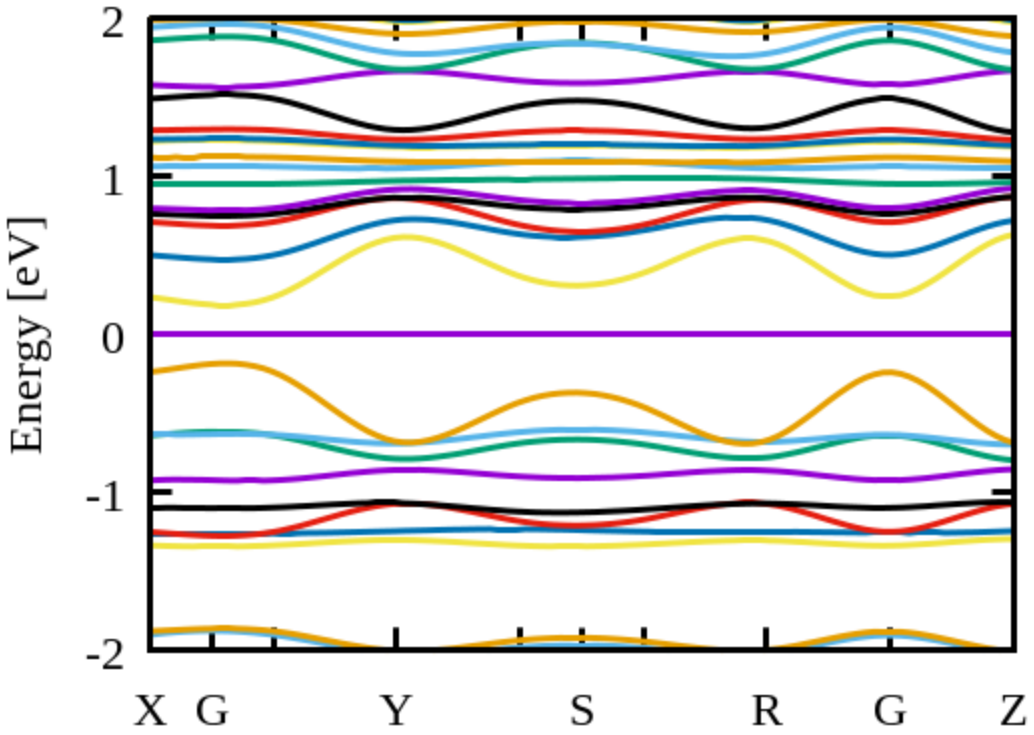

Figure 4.7: The electronic band structure of Mn_2SiS_4 obtained by DFT-PBE calculation.

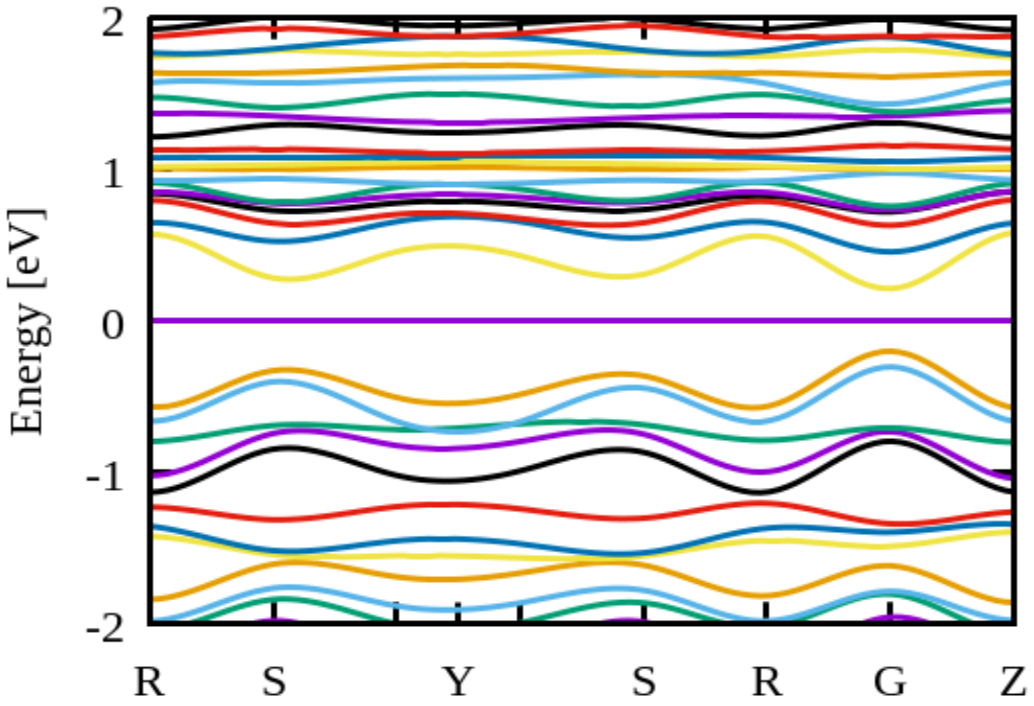

Figure 4.8: The electronic band structure of Mn_2SiSe_4 obtained by DFT-PBE calculation

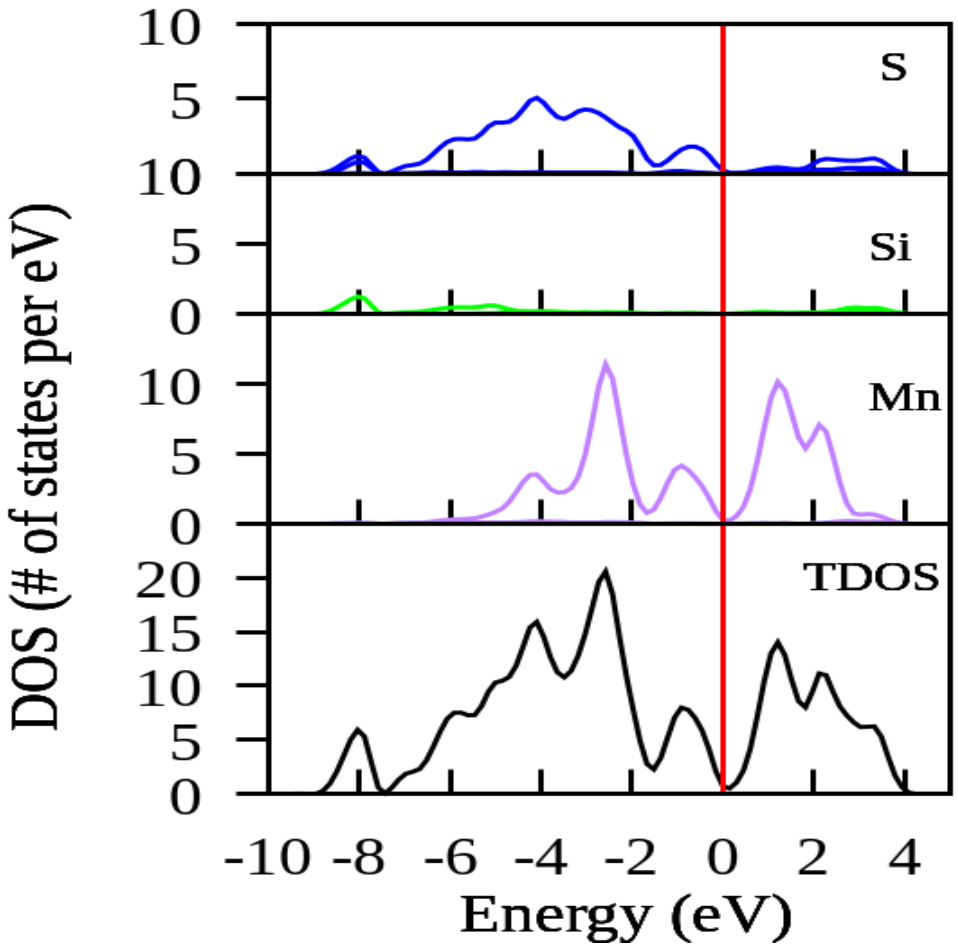

Figure 4.9: The electronic projected density of states (PDOS) of Mn_2SiS_4

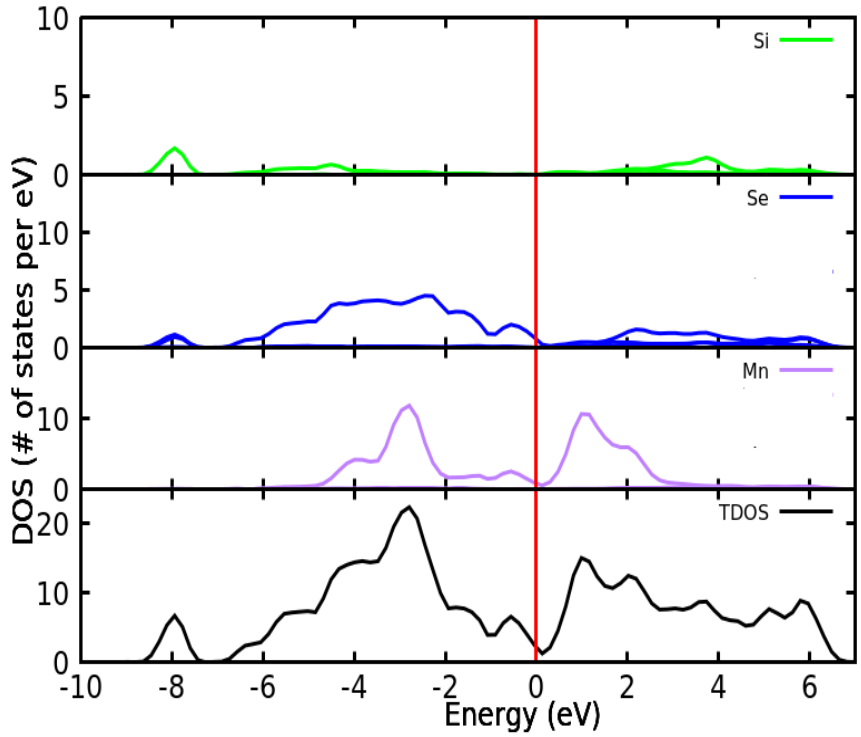

Figure 4.10: The electronic PDOS for Mn_2SiSe_4

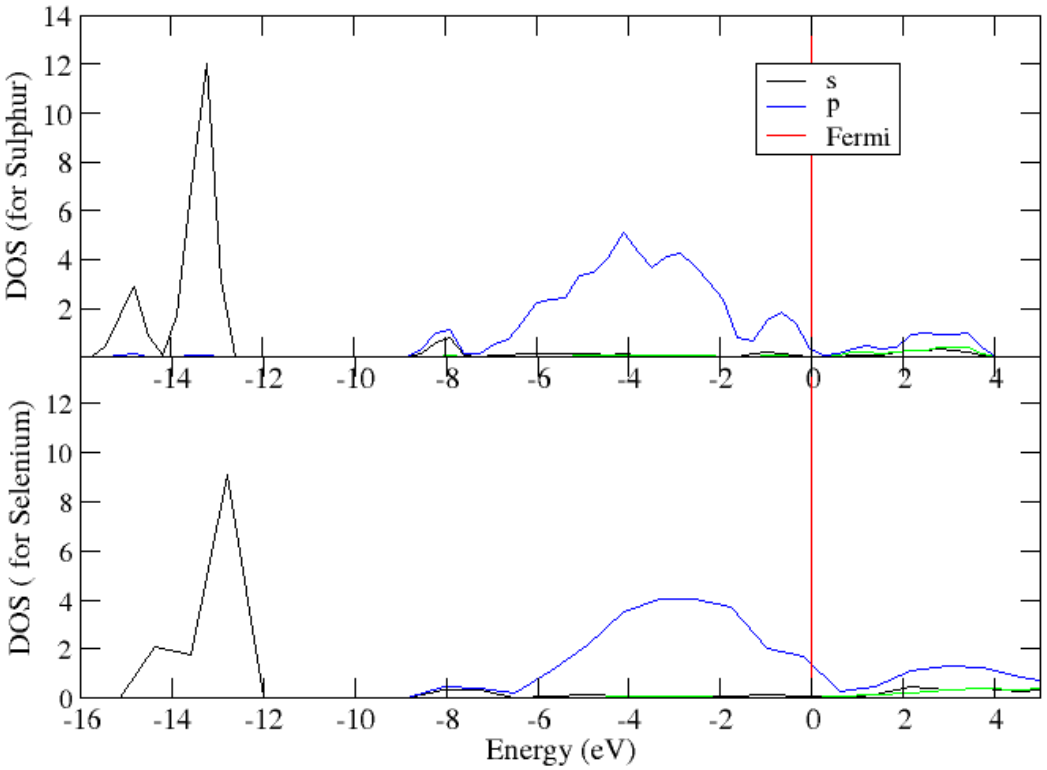

Figure 4:11. The s and p states for Sulphur and selenium as represented in Fig. 4.9 and Fig. 4.10. The respective orbital contribution is also represented

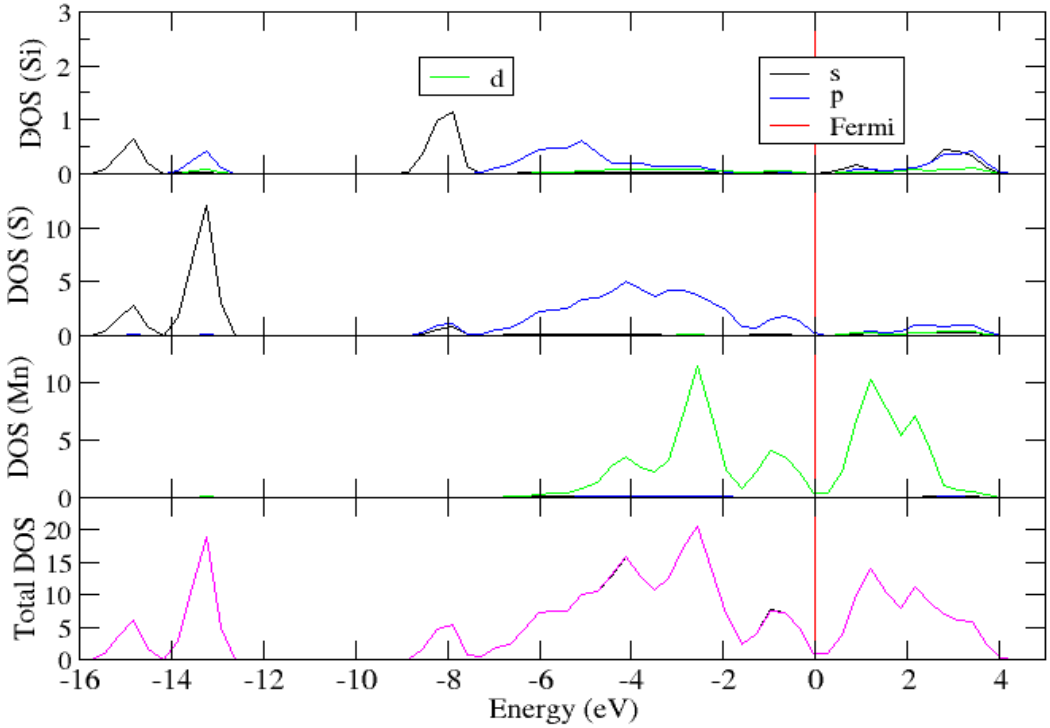

Figure 4.12: The PDOS for Mn_2SiS_4

4.6 CONCLUSIONS

We have performed the DFT calculations for the antiferromagnetic spin arrangement of the four different compositions in $Mn_2SiS_{4-x}Se_x$ from x=0 to 4. Our computations confirm the shift in transition temperature from 86 K to 66K as the value of x is incremented uniformly. The calculated magnetic moments on the Mn atoms agree with the experimental values reported in the literature and we find them to be antiferromagnetic spin ordering. The band structure features from Mn_2SiS_4 and Mn_2SiSe_4 are probable for thermoelectric applications.

REFERENCES

[1] R. Santoro, R. Newnham and S. Nomura., "Magnetic properties of Mn2SiO4 and Fe2SiO4," *J. Phys. Chem. Solids,* vol. 27, no. 4, pp. 655-666, 1966.

[2] S. Nomura, R. Santoro, J. Fang and R. N. , *J. Phys. Chem. Solids,* vol. 25, p. 901, 1964.

[3] J. Creer and G.J.F. Troup, "The crystal and magnetic structures of Mn2GeO4," *Solid State Commun. ,* vol. 8, no. 15 , pp. 1183-1188, 1970.

[4] P. Monceau, Electronic Properties of Inorganic Quasione-dimensional Compounds; Physics and Chemistry of Materials with Low-dimensional Structures, Series B, D. Reidel, Dordrecht, Holland, 1985.

[5] J. Rouxel, Crystal Chemistry and Properties of Materials with Quasi-one-dimensional Structures; Physics and Chemistry of Materials with Low-dimensional Structures, Series B, D. Reidel, Dordrecht, Holland, 1986.

[6] V. Carteaux, D. Brunet, G. Ouvrard and G. Andre, *J. Phys. Condens. Mattter,* vol. 7, p. 68, 1995.

[7] V. Carteaux, G. Ouvrard, J. Grenier and Y. Laligant, *J. Magn. Magn. Mater.,* vol. 5, p. 237, 1991.

[8] J. Gopalakrishnan and K. Nanjundaswamy, *Mater. Res. Bull.,* vol. 23, p. 107, 1988.

[9] A.-M. Lamarche, G. Lamarche, C. Church, J. Woolley, I. Swainson and T. Holden, "Neutron diffraction study of magnetic phases in polycrystalline Mn2SiS4," *Journal of Magnetism and Magnetic Materials,* vol. 137, no. 3, pp. 305-312, 1994.

[10] G. Lamarche, F. Lamarche and A.-M. Lamarche, "A possible 83K magnetic detector for high energy particles," *Physica B: Condensed Matter,* Vols. 194–196, Part 1, no. 0921-4526, pp. 219-220, 1994.

[11] F. Bodénan, V. Cajipe, G. Ouvrard and G. André, "Low-temperature magnetic structure of the olivine Mn2SiSe4," *Journal of Magnetism and Magnetic Materials,* vol. 164, no. 1-2, pp. 233-240, 1996.

[12] S. Jobic, F. Bodtnan, P. L. Boterf and G. Ouvrard., "Structure refinement and magnetic behaviour of the only selenide in the olivine group family: Mn,SiSe4," *J. Alloy Camp.,* vol. 230, pp. 16-22, 1995.

[13] A. Junod, K.-Q. Wang, G. Triscone and G. Lamarche, "Specific heat, magnetic properties and critical behaviour of Mn2SiS4 and Fe2GeS4," *Journal of Magnetism and Magnetic Materials,* vol. 146, no. 1-2, pp. 21-29, 1995.

[14] K. Ohgushi and Y. Ueda, "Anomalous Magnetic Properties near the Spin-Flop Bicrtical point in Mn2AS4 (A=Si, Ge)," *Phys. Rev. Lett.,* vol. 95, p. 217202, 2005.

[15] J. Fuhrmann and J. Pickardt, *Acta Crystallogr,* vol. C45, p. 1808, 1989.

[16] R. Williardson and A.C Beer, "1988 Diluted magnetic semiconductors, Semiconductors and Semimetals ed J K Fundyna and J-Kossut vol 25," New York:Academic chapter, 1988.

[17] L. Yu, S. Lany, R. Kykyneshi, V. Jieratum, R. Ravichandran, B. Pelatt, E. Altschul, H. A. S. Platt, J. F. Wager, D. A. Keszler and A. Zunger, "Iron Chalcogenide Photovoltaic Absorbers," *J. Adv. Energy Mater,* vol. 1, no. 5, pp. 748-753, 2011.

[18] S. J. Fredrick and A. L. Prieto, "Solution Synthesis and Reactivity of Colloidal Fe2GeS4: A Potential Candidate for Earth Abundant, Nanostructured Photovoltaics," *J. Am. Chem. Soc. ,* vol. 135, no. 49, p. 18256–18259, 2013.

[19] H. Vincent and E.F. Bertaut, *J. Phys. Chem. Solids ,* vol. 34, p. 15, 1973.

[20] G. V. Kumar, V. Kanchana and G. Vaitheeswaran, "Predicted thermoelectric properties of olivine-type Fe 2 GeCh 4 (Ch = S, Se and Te)," *J. of Phys. Cond. Matter,* vol. 28, p. 025502, 2016.

[21] I. S. Hagemann, P. G. Khalifah, A. P. Ramirez and R. J. Cava, "Geometric magnetic frustration in olivines," *Phys. Rev. B,* vol. 62, p. 771, 2000.

[22] J. Furthmüller, J. Hafner and G. Kresse, "Ab initio calculation of the structural and electronic properties of carbon and boron nitride using ultrasoft pseudopotentials," *Phys. Rev. B,* vol. 50, no. 21, pp. 15606-15622, 1994.

[23] G. Kresse and J. Furthmueller, " Efficiency of ab-initio total energy calculations for metals and semiconductors using plane-wave basis set," *Comp. Mat. Sci.,* vol. 6, pp. 15-50, 1996.

[24] G. Kresse and J. Furthmüller, "Efficient iterative schemes for ab initio total-energy calculations using a plane-wave basis set," *Phys. Rev. B,* vol. 54, no. 16, pp. 11169-11186, 1996.

[25] P. E. Bloechl, " Projector augmented-wave method," *Phys. Rev. B,* vol. 50, p. 17953, 1994.

[26] G. Kresse and D. Joubert, "From ultrasoft pseudopotentials to the projector augmented-wave method," *Phys. Rev. B,* vol. 59, p. 1758, 1999.

[27] PETER E BLÖCHL, CLEMENS J FÖRST and J. SCHIMPL, "Projector augmented wave method: ab initio molecular dynamics with full wave functions," *Bull. Mater. Sci.,* vol. 26, no. 1, pp. 33-41, 2003.

[28] H. J. Monkhorst and J. D. Pack, "Special points for Brillouin-zone integrations," *Phys. Rev. B,* vol. 13, no. 12, pp. 5188-5192, 1976.

[29] K. Momma and F. Izumi, "VESTA for three-dimensional visualization of crystal, volumetric and morphology data," *J. Appl. Cryst.,* vol. 44, pp. 1272-1276, 2011.

[30] H. Nhalil, R. Baral, A. Cosio, B. Khamala, S. R. Singamaneni, M. Fitt, R. Z. T. B. D. Antonio, K. Gofryk, B. Saparov and H. Nair, "Evolution of the spin-flop antiferromagnetic transition and the emergence of frustration in saw-tooth lattice Mn2SiS4-xSex (x = 0 - 4) chalcogenides," in *American Physical Society*, Boston, 2019.

[31] V. K. Gudelli and V. Kanchana, "Predicted thermoelectric properties of olivine-type Fe2GeCh4 (Ch = S, Se and Te)," *J. Phys. Condens. matt.,* vol. 28, no. 025502, 2016.

[32] G. Kreese and J. Hafner, "AB initio molecular dynamics for liquid metals," *Phys. Rev. B,* pp. 47, 558-561, 1993.

CHAPTER 5: SUMMARY

We have investigated the interface formation between MAI-terminated 001 surface of the cubic phase of $MAPbI_3$ perovskite layer and endohedral metallofullerene derivatives viz. $Sc_3N@C_{80}$ and $Sc_3N@C_{80}$PCBM using DFT calculations. Methylammonium lead halide perovskite-based solar cells have recently emerged as a promising class of materials for photovoltaic applications with efficiencies reaching over 22%. Fullerene-based materials are widely employed as efficient electron transport layers and interfacial modification layers in perovskite solar cells due to their outstanding electronic and photophysical properties and their well-matched energy levels with perovskites. We have used VASP within DFT as computational techniques to perform the analysis and optimization of perovskite methylammonium lead iodide ($MAPbI_3$)/metallofullerene interfaces such as fullerene ($Sc_3N@C_{80}$) and fullerene derivatives ($Sc_3N@C_{80}$PCBM). We investigated $MAPbI_3$ slab models with methylammonium Iodide (MAI-T) and lead Iodide (PbI_2-T) terminated surfaces in 001 direction with different orientations ($–CH_3$ and $–NH_3$) pointing to the vacuum.

The band gap of the MAI-terminated models (1.85–1.45 eV) has been shown to be in closer agreement to the experimentally measured band gap (1.55–1.7 eV) than the band gap of the PbI models (1.15–1.36 eV). As described earlier in the computational methods chapter, both topC and topN orientations of the MA ions are studied. We found the energetics of the 2×2×5 and 3×3×3 MAIT slab models and their optimized geometries. The topC models are found to be more stable for the 2×2×5 slab models while topN models are slightly more stable for the 3×3×3 slab models.

For studying the perovskite-metallofullerene interfaces, we placed the $Sc_3N@C_{80}$ in contact with the 2×2×5 slab model and $Sc_3N@C_{80}$PCBM in contact with the 3×3×3 slab model. Two different initial positions of the $Sc_3N@C_{80}$ on both topN and topC 2×2×5 $MAPbI_3$ slab model have been probed: one considering the interface of the pentagonal face of C_{80} with the slab ($Sc_3N@C_{80}$ -Pent) and the second with the interface of the hexagonal face of C_{80} with the slab ($Sc_3N@C_{80}$ -Hex). For $Sc_3N@C_{80}$PCBM, the interface with the phenyl-butyric acid methyl ester

side chain facing the slab model is used for the calculations. The interface binding energy can be considered as a criterion to judge the stability of the interfaces. The interface binding energies and shortest interfacial distances for the perovskite/metallofullerene interfaces are obtained.

It is seen that C_{80} orientation in $Sc_3N@C_{80}$ has an important effect on the stability of the adlayers. The adlayer of $Sc_3N@C_{80}$ with its hexagonal face on the 2×2×5 topN perovskite surface displays an interface binding energy of 1.05 eV and hence is more stable compared to the one with the pentagonal face. However, the interface of the 2×2×5 topC slab model with the pentagonal face of $Sc_3N@C_{80}$ has a large negative binding energy which indicates a repulsive interaction. The binding energies for $Sc_3N@C_{80}$-PCBM interface with topN and topC slab models are nearly the same, viz., the weakly repulsive and attraction of -0.04 eV and 0.042 eV respectively. Here, the shortest interfacial interaction distances are 2.99 and 2.41 Å respectively for the topN and topC models. Interestingly, these are H...H interactions between the H atom of the methyl ester side chain of $Sc_3N@C_{80}$-PCBM and the $-NH_3$ of MA ion.

Thus, both the endohedral metallofullerenes investigated form stable interfaces with the MAI- terminated surfaces of $MAPbI_3$ perovskites (except the topC interface with $Sc_3N@C_{80}$) with binding energies in the range of 0.26 to 1.09 eV. The interface binding energies for the formation of a C_{60} adlayer on the perovskite surfaces has been reported to be in the range from 0.3 to 1.0 eV per C_{60} recently by Quartil et al., which are comparable to our results. Our results suggest that endohedral metallofullerene derivatives can form more stable interfaces with perovskite surfaces compared to pristine fullerenes.

Our calculated binding energies have shown the possibility of adsorption at the interface. The density of states and band gaps show that these interfaces may be useful in solar energy converters. Therefore, designing interfaces with strong binding are vital to developing efficient, high-performing solar cells and medical imaging platform.

We have also studied the structural, electronic, and magnetic behavior of olivine A_2BX_4 (A=Mn, B=Si, X=S, Se). The olivine is known to be magnetic semiconducting material which makes it favorable in magnetic and optoelectronic applications. The Mn occupies the mirror and

symmetry locations that uniquely defines its application. The olivine chalcogenides are in the antiferromagnetic phase at the low-temperature limit. Their critical temperature is linearly proportional to its selenium content where 86 K for Mn_2SiS_4 and 66K for Mn_2SiSe_4. We studied $Mn_2SiS_{4-x}Se_x$ for x = 0 to x = 4 through first principle calculations for the structural, electronic, and antiferromagnetic spin arrangements of the four different compositions of $Mn_2SiS_{4-x}Se_x$. Our spin magnetic moments, density of states, and bandgap are comparable to the available experimental data. We also find that several spin structures can exist depending on the doping content.

APPENDIX

Table C1: Total energies (eV), DFT-D3 binding energies, and PBE-binding energies for Sc3N@C80 (A), $Sc_3N@C_{80}$-PCBM, perovskite surfaces, and their respective complexes

DFT-D3					DFT-D3	DFT-PBE
Orientation	Config.	Complex	surface	$Sc3@C_{80}$/PCBM	BE	BE
Ntop(Hex)	225MAIT/A	-1951.46	-1200.18	-750.06	1.2	1.05
Ntop(pent)	225MAIT/A	-1950.62	-1200.18	-750.06	0.38	0.26
Ctop	225MAIT/A	-1950.73	-1198.19	-750.06	2.48	-5.58
Ntop	333MAIT/B	-2704.67	-1782.32	-922.24	0.11	-0.04
Ctop	33MAIT/B	-2703.05	-1780.13	-922.24	0.69	0.04

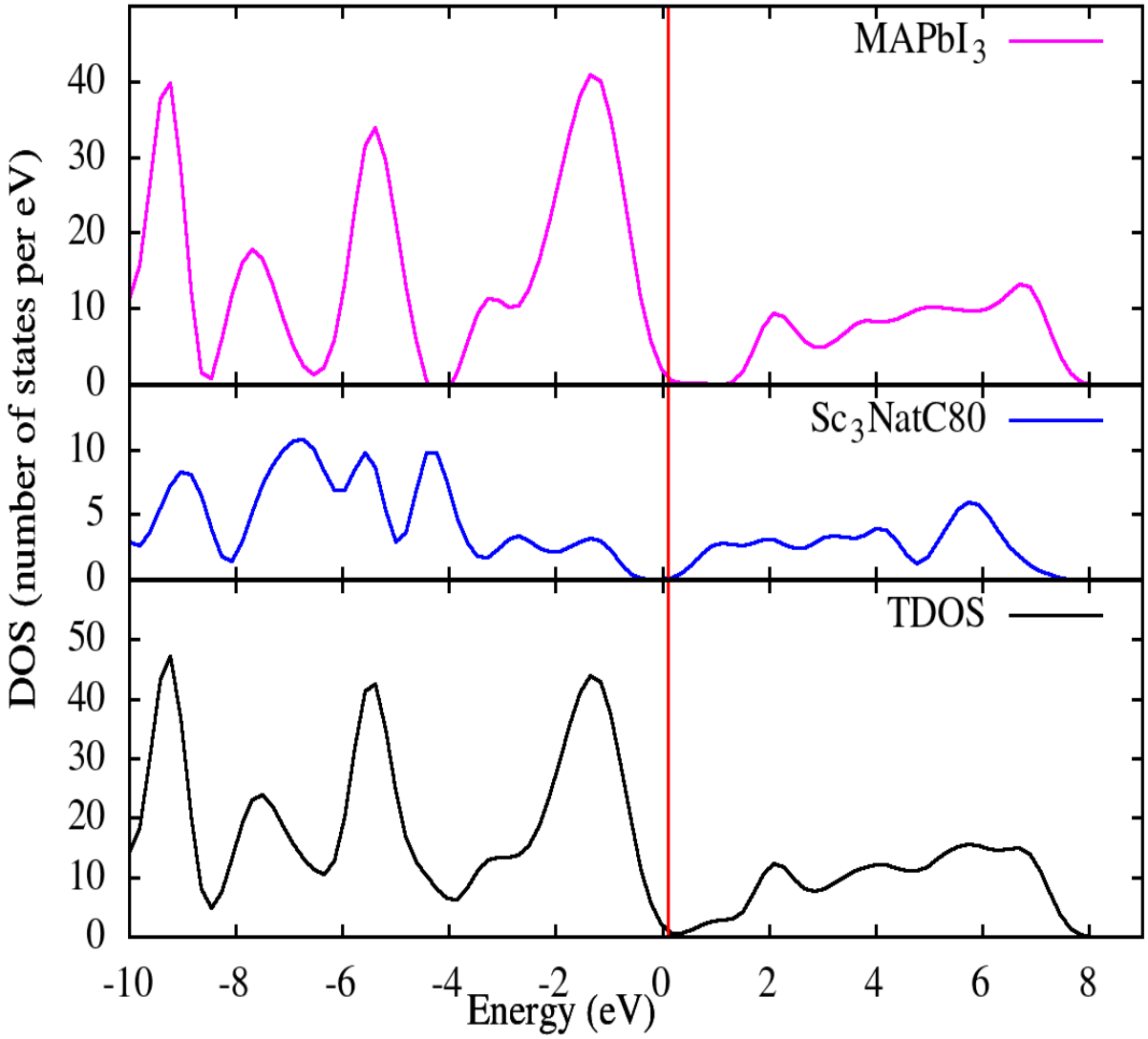

Figure C.1: DOS representation for $Sc_3N@C_{80}$ binding on the $MAPbI_3$ and the complex (TDOS)

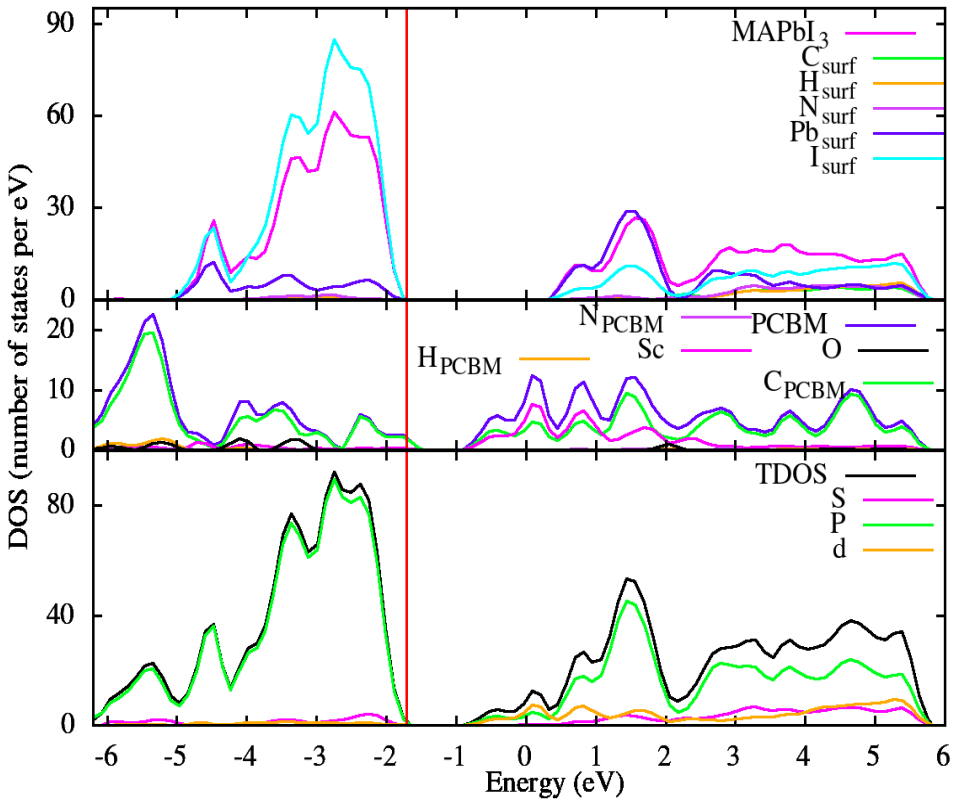

Figure C2: Projected DOS of MAPbI3/PCBM analogue interface. From top: MAPbI3 surface, Sc3N@C80PCBM, and pDOS for their complex. The Fermi level of -1.74 eV is shown by a vertical line in red

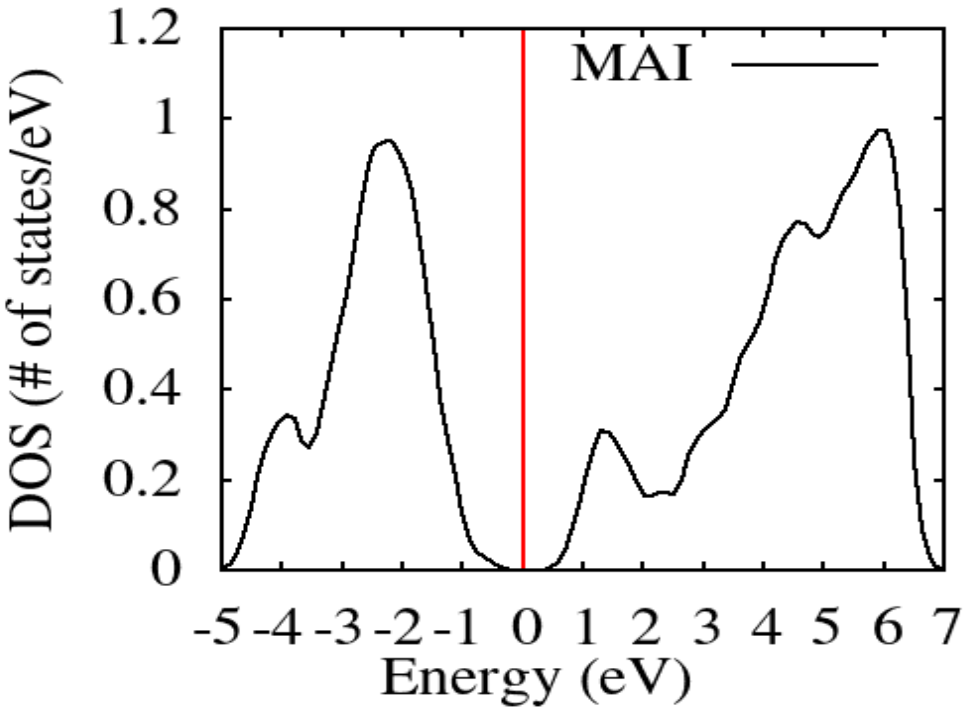

Figure C3: DOS for 2.2.5 MAIT surface

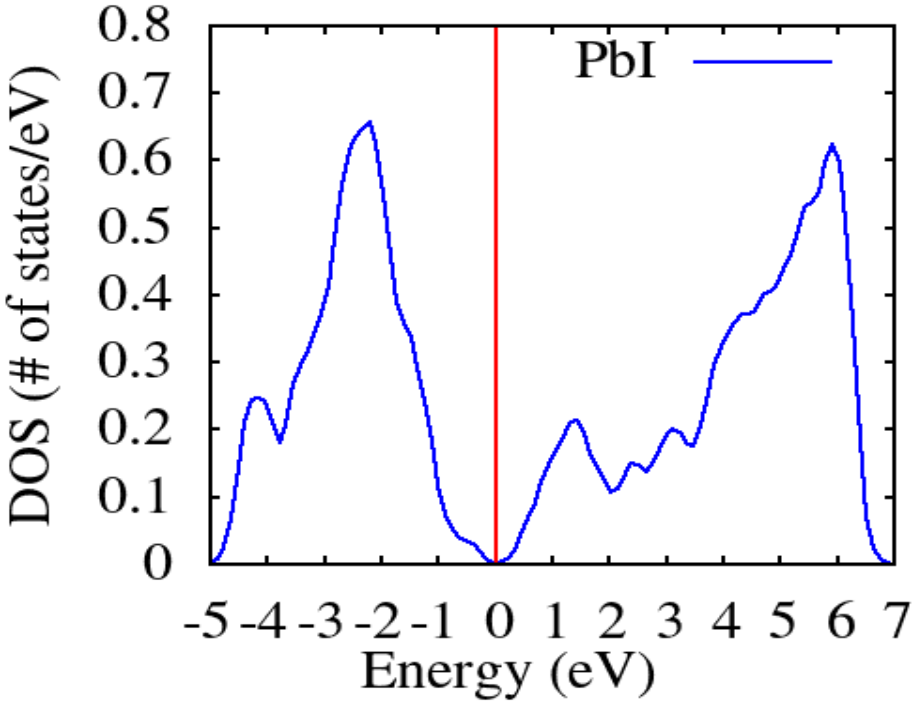

Figure C4: DOS for 2.2.5 PbIT surface

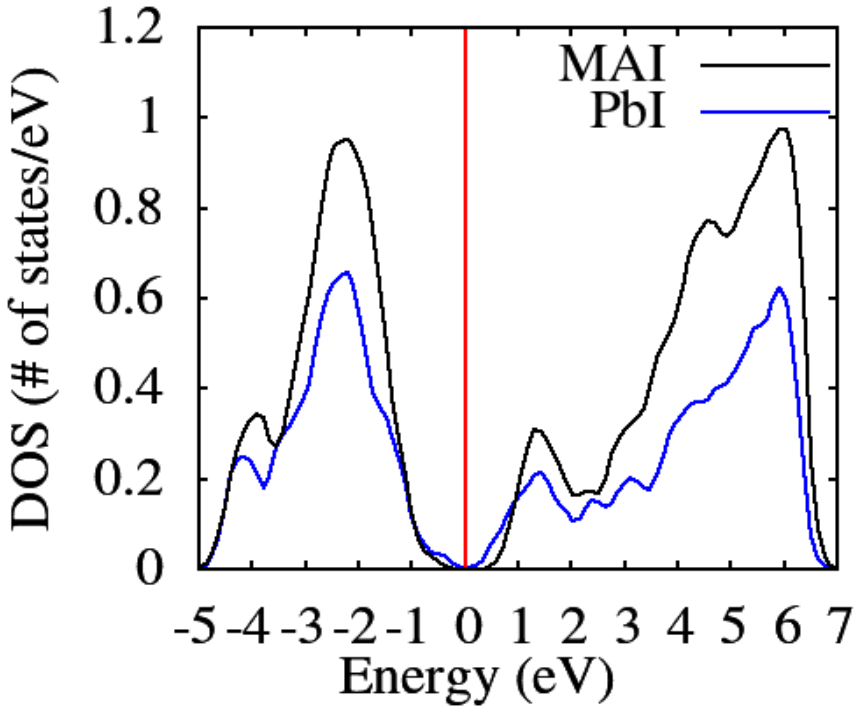

Figure C5: DOS of 2.2.5 MAIT and 2.2.5 PbIT surface

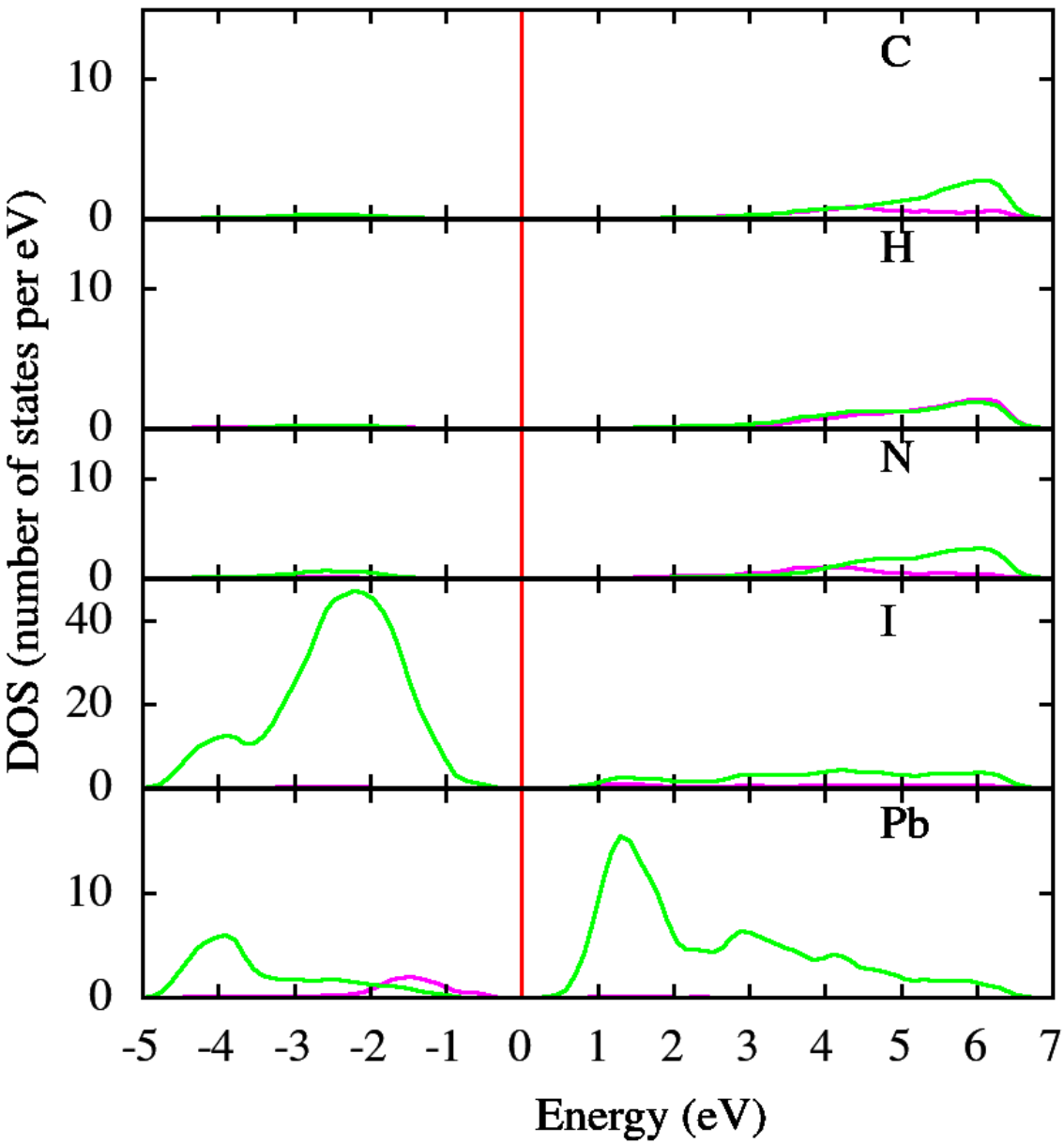

Figure C.6: PDOS representation for 2.2.5-MAI-T surface. S-orbitals are represented by magenta graphs while p-orbitals are represented by green color graphs.

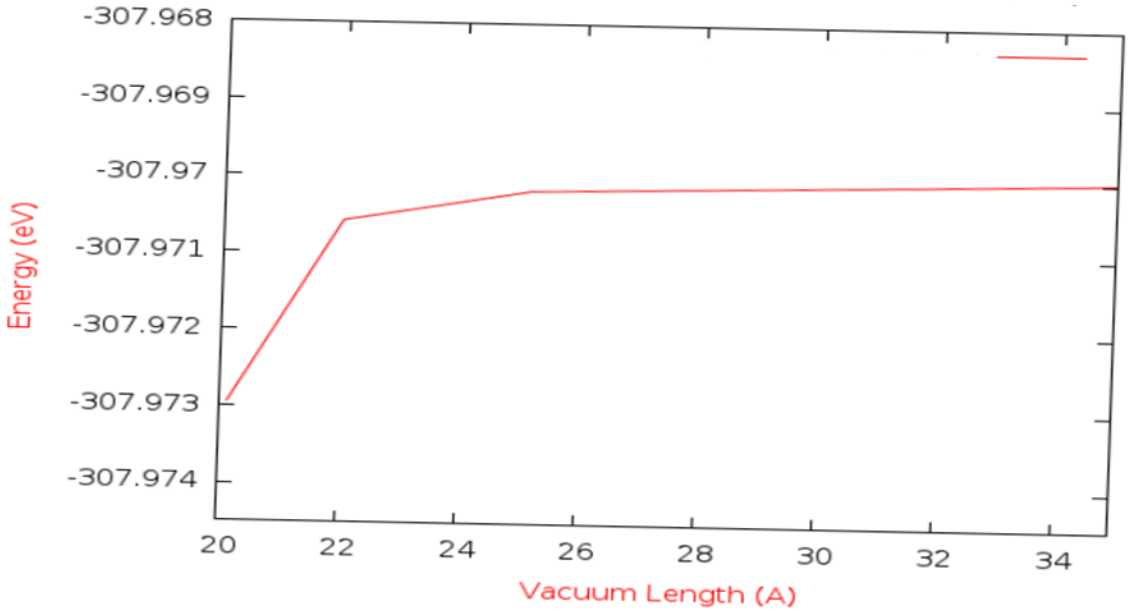

Figure C.7: A Plot of minimum energy in eV as a function of Vacuum length in Å.

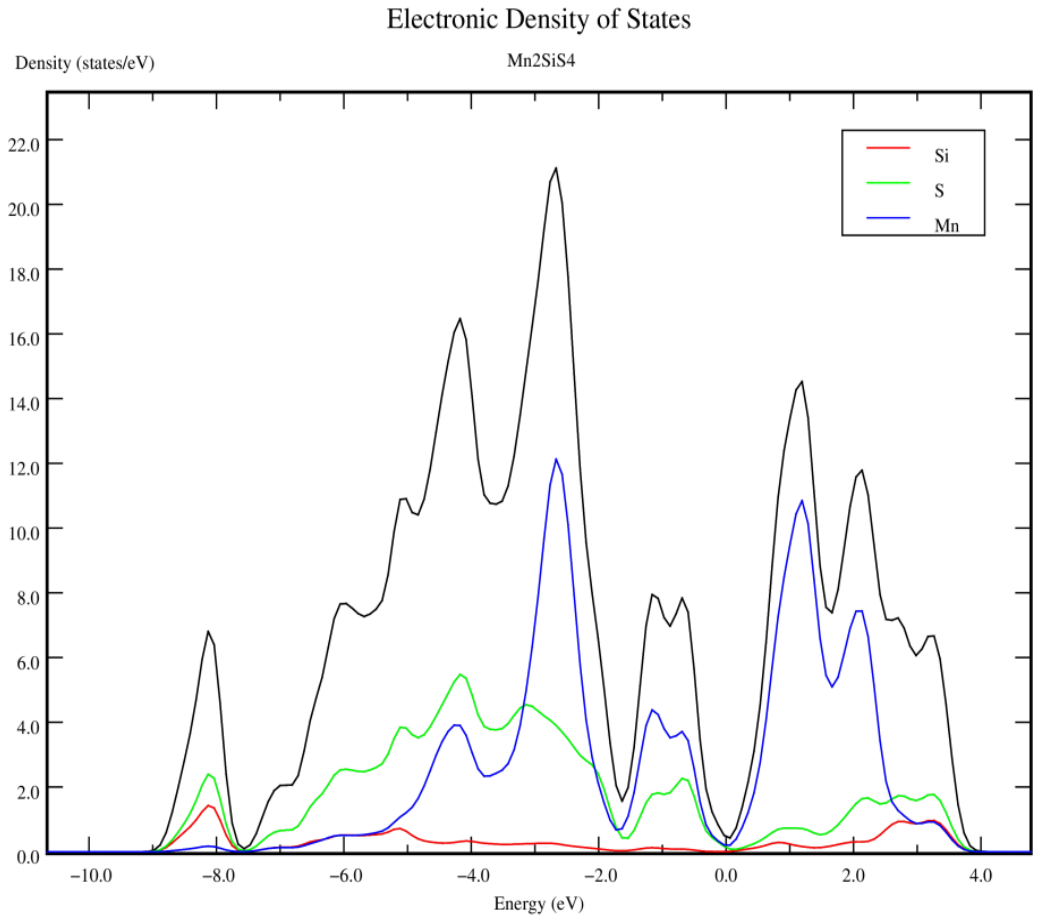

Figure D.1: The electronic projected density of states (PDOS) of Mn2SiS4 plotted on the same axes.

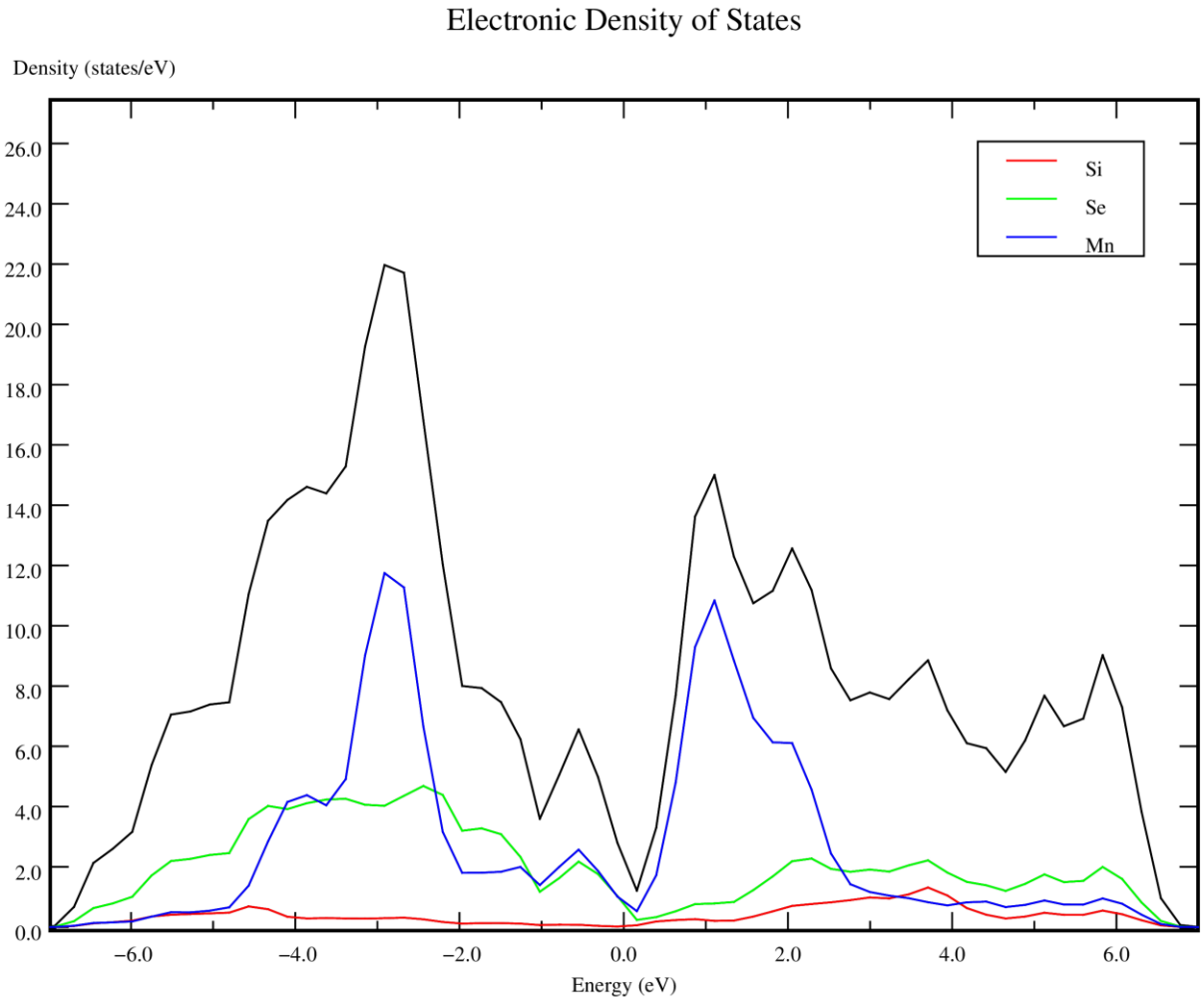

Figure D.2: The electronic PDOS for Mn_2SiSe_4 plotted on the same axis

Table C.2: A single-point calculation performed on 3.3.3MAIT/Sc3N@C80 (517 atoms) to determine the best Parallelization of VASP in this system using stampede with 64 processors per node. NCORE determines the number of cores work per orbital. NPAR should be taken to be the number of cores per compute node.

# nodes	# cores	#NCORES	# NPAR	Wall time (sec)	Total Energy (eV)
1	64	32	2		-2670.2402
2	128	32	4		-2670.2233
3	192	32	6		-2670.2235
3	204	17	12		-2670.2285
4	256	32	8		-2670.2256
4	272	17	16		-2670.2410
5	320	32	10		-2670.2276
5	340	20	17		-2670.2402
6	384	32	12		-2670.2236
6	408	17	24	5542	-2670.2272
7	448	32	14	5116	-2670.2258
7	476	17	28		-2670.2232
8	512	32	16	4839	-2670.2233
8	544	32	17	4993	-2670.2233

Table C.3: A single-point calculation performed on $Sc_3N@C_{80}$ (84 atoms) to determine the best Parallelization of VASP in this system using stampede with 68 processors per node.

# nodes	# cores	#NCORES	# NPAR	Wall time (sec)	Total Energy (eV)
1	68	34	2	3835	-746.21777099
2	136	34	4	2922	-746.21777099
3	204	34	6	2079	-746.21777099
4	272	34	8	2041	-746.21777099
5	340	34	10	2039	-746.21777099
6	408	34	12	2034	-746.21777099
7	476	34	14	1924	-746.21777099
8	544	34	16	1759	-746.21777099

VITA

Bethuel Omutiti Khamala was born in Bungoma, Kenya, to Mr. Paul Khamala Mukhongo and Mrs. Jane Nakhumicha Mukhongo. He attended his first school at Kimugui Primary School from 1988-1995. He was then enrolled at chebuyusi High School for his secondary education where he graduated in 1999. He earned his Bachelor of Science degree in Physics from Moi University, Kenya in 2005 and MPhil in 2007. In 2014, he received his Master of Science degree in Physics and Mathematics from Southern University, LA. He joined UTEP's doctoral program in Computational Science in Fall 2014.

Dr. Khamala was the recipient of the Alpha Kappa Alpha Education Advancement Foundation Scholarship in 2014. He was also a recipient of a State of Texas Public Education Grant for International Students and Teaching Assistantship from Computational Science.

Dr. Khamala's research has been presented in part at several meetings including the 2019 American Physical Society. His work has appeared in the proceedings of these conferences. He has the Olivine results published in the Physical Review B and the article on perovskites is being submitted to the journal of physics.

While pursuing his degree, Dr. Khamala worked as a research associate for the Department of Mathematics, Teaching Assistant in Computational Science, and Adjunct Professor in Physics department at EPCC. In Co-curricular, he served as the President for SIAM-UTEP chapter, and Secretary for Computational Science Students Association.

Dr. Khamala's dissertation, "Computational Studies on Perovskite-Metallofullerene Interface and Magnetic Properties of Mn-based Mixed Olivines," was supervised by Dr. Rajendra Zope and Dr. Tunna Baruah. Dr. Khamala has accepted a Postdoc position at UTEP.

Address: khamalabethuel59@gmail.com